DOI:10.14753/SE.2019.2319

Investigation of Glutamatergic Synaptic Transmission in Hippocampal Pyramidal Cells

Ph.D. thesis

Éltes Tímea M.D.

János Szentágothai Doctoral School of Neurosciences
Semmelweis University

Supervisor: Zoltán Nusser, DVM, D.Sc.

Official reviewers: Zelles Tibor, Ph.D.
Mátyás Ferenc, Ph.D.

Head of the Final Examination Committee: Ligeti Erzsébet, D.Sc.
Members of the Final Examination Committee:
Wittner Lucia, Ph.D.
Köles László, Ph.D.

Budapest
2019

DOI:10.14753/SE.2019.2319

TABLE OF CONTENTS

DOI:10.14753/SE.2019.2319

DOI:10.14753/SE.2019.2319

DOI:10.14753/SE.2019.2319

1. ABBREVIATIONS

+	positive
*	p < 0. 05
2P	two-photon
3D	3-dimensional
AP	action potential
AU	arbitrary unit
AZ	active zone
Bkgrd	background
CA	Cornu Ammonis
CV	coefficient of variation
DG	dentate gyrus
duA	'*detected unitary*' amplitude
EC	Entorhinal Cortex
Elfn1	extracellular leucine-rich repeat fibronectin-containing protein 1
EM	electron microscopic
EPSC	excitatory postsynaptic current
EPSP	excitatory postsynaptic potential
ER	error rates
Fv	felszabadulási valószínűség
FOV	field of view
FS	fast-spiking
FWHM	full width at half-maximal amplitude
GABA	gamma aminobutyric acid
GEVI	genetically encoded voltage indicators
IN	interneuron
IQR	interquartile ranges
ISI	inter spike interval
mGluR1α	metabotropic glutamate receptor 1α
MW U	Mann-Whitney U test

DOI:10.14753/SE.2019.2319

NA	numerical aperture
NGS	normal goat serum
O-Bi	oriens-bistratified
O-LM	oriens-lacunosum moleculare
PB	phosphate buffer
PC	pyramidal cell
PFA	paraformaldehyde
p_{nonlin}	nonlinearity parameter
P_r	release probability
PS	piramissejt
PSD	postsynaptic density
PSP	postsynaptic potential
puA	'*presumed unitary*' amplitude
PV	parvalbumin
ROI	region of interest
SDS-FRL	sodium dodecylsulphate- digested freeze-fracture replica labeling
SNR	signal to noise ratio
SOM	somatostatin
str. l-m	stratum lacunosum-moleculare
str. luc.	stratum lucidum
str.ori.	stratum oriens
str. rad.	stratum radiatum
SV	synaptic vesicle
TBS	Tris-buffered saline
VGCC	voltage-gated Ca^{2+} channels

DOI:10.14753/SE.2019.2319

2. INTRODUCTION

2.1. Glutamatergic synaptic transmission in the central nervous system

Regulated control of synaptic transmission is essential for gating the information flow through neuronal circuits. Functional parameters such as neurotransmitter release probability (P_r), size of postsynaptic response, short- and long-term plasticity and efficacy are different depending on the identity of the pre- and postsynaptic neurons. Moreover, different axon terminals of a cell can have different release probabilities resulting in a context-dependent activation of the postsynaptic cells by the same presynaptic cell (reviewed in Nusser, 2018). A depressing synapse with high initial transmitter release probability is more efficacious at low frequencies, whereas a facilitating synapse with low initial release probability will be more efficacious at high frequencies, and can serve as presynaptic burst detector (Blackman et al., 2013). The fact that such a mechanism is present in spite of the necessity of a signaling mechanism between the pre-and postsynaptic cells, suggests that this form of diversity is potentially crucial for the information processing in the mammalian brain (Blackman et al., 2013).

Understanding the rules of formation of synapses with diverse properties is crucial for elucidating how neuronal circuits are built up from individual neurons, which are then responsible for the emergence of complex behaviors and memory formation. The mechanism underlying the differential regulation of synaptic properties however, remains elusive. In the next sections, after introducing the studied brain region, I will summarize our current knowledge about the anatomical and molecular features and the functional properties of synapses. Then, in the first part of my results section I will present my experiments, which extended our current knowledge about the mechanisms of target cell-type dependent differences in release probability (Éltes et al., 2017).

Recent results provide evidence that the heterogeneity of principal cells, in concert with the heterogeneity of synaptic properties, can constitute several distinct, nonuniform parallel circuit modules underlying the diverse downstream effects of circuit activity (Soltesz and Losonczy, 2018). In order to observe the extent of the influence of synaptic diversity on information processing, storage and retrieval, it is necessary to simultaneously and chronically record the activity of large ensembles of neurons in behaving animals that are

anatomically and biochemically identifiable. *In vivo* electrophysiological recordings have the required temporal resolution, but they allow the monitoring of the activity of a relatively modest number of cells for short periods and provide limited information about the identity of the recorded cells (Buzsáki, 2004). Investigating neuronal activity using genetically encoded Ca^{2+} indicators in behaving animals has become a widely used technique. However, inferring the spiking activity from fluorescent traces, is still a formidable challenge due to the different expression levels and the highly nonlinear nature of the most widely used genetically encoded Ca^{2+} indicators (Jercog et al., 2016; Lin and Schnitzer, 2016). In the Introduction I will detail the limitations of the current state of the art optical imaging techniques, and in the second part of my results section I will explore how the amount of GCaMP6f in the cells affects the amplitude, kinetics and temporal summation of [Ca^{2+}] transients, and I will also elucidate the effect of indicators expression level and of the variability of the unitary fluorescence signals on the spike inferring performance. Finally I will offer a reliable spike inference strategy with a superior accuracy compared to currently available methods (Éltes et al., 2019).

2.2. The hippocampus

The hippocampal formation, located within the temporal lobe of the brain, forms a computational unit that includes the dentate gyrus, hippocampus proper (*Cornu Ammonis*, CA), subiculum, presubiculum, parasubiculum, and entorhinal cortex (EC) (Andersen et al., 2007). The hippocampus attracted the attention of neuroscientists due to its implications in mnemonic processes and episodic memory; and because of its phylogenetically highly preserved and simplified structure, with cell bodies, inputs and outputs ordered in distinct layers (Andersen et al., 2007). The first evidence pointing towards its role in memory retrieval has emerged in the 1950's when Scoville and Milner reported that patient H.M. suffered anterograde memory impairment due to a bilateral hippocampal removal surgery (Scoville and Milner, 1957). Since then, the hippocampal formation has been associated with several other conditions, such as epilepsy and Alzheimer's disease (Green, 1964). Beside its significance in different pathologies hippocampal neurons can encode spatial locations (O'Keefe and Dostrovsky, 1971) and time (Pastalkova et al., 2008; Kraus et al., 2013;

MacDonald et al., 2013). Hippocampal neurons can also recognize the position of conspecifics (Omer et al., 2018), possibly playing a role in social interactions; they are able to code constant landmarks of changing environments (Geiller et al., 2017), and locomotion or immobile periods of a task (Arriaga and Han, 2017). Some hippocampal neurons increase their activity in reward zones during reverse replays in accordance with the relative amount of the reward (Ambrose et al., 2016). Aronov et al hypothesize and provide evidence that the spatial representations are just examples of a general mechanism for encoding any arbitrary continuous variables that are relevant to an animal (Aronov et al., 2017). Due to these intriguing implications and its simplified structure the hippocampus became a model system for neuroanatomical and electrophysiological studies relating to the synaptic organization of the brain. Therefore, I have chosen to investigate glutamatergic synaptic transmission in this brain region.

2.2.1. The intrinsic organization of the hippocampus

The hippocampus is devided to four main regions: dentate gyrus, area CA3, CA2, and CA1 of the hippocampus proper. The dentate gyrus consists of three layers: 1) the molecular layer where the apical dendrites of the granule cells receive their input; 2) the granule cell layer in which the somata of principal cells, the granule cells are located in a tightly packed manner; 3) a polymorphic layer/ hilus which is comprised of polymorphic cells and the efferent fibers of the dentate gyrus (***Figure 1***) (Andersen et al., 2007).

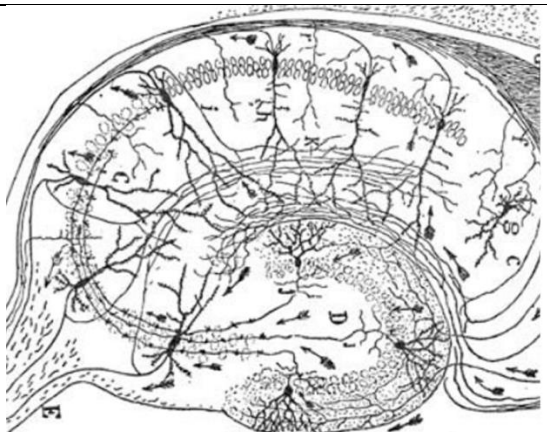

Figure 1. The hippocampus.
Drawing of Santiago Ramon y Cajal of the hippocampus in his 1911 book Histologie de Système Nerveux. The arrows give his interpretation of likely impulse direction. Abbreviations: D, dentate gyrus; C, hippocampus proper. Modified from (Andersen et al., 2007).

The principal cells from the three areas of the hippocampus proper are also organized in a single layer; however, the size of their somata are different along the proximodistal axis

DOI:10.14753/SE.2019.2319

(***Figure 1***) (Andersen et al., 2007). All these principal cells release L-glutamate from their axon terminals.

Additionally to the laminar division of the neuronal elements of the hippocampus, the pyramidal cells (PCs) of the CA1 region are morphologically, molecularly and functionally (physiological properties, connectivity) heterogeneous along a radial axis, that is perpendicular to the PC layer (reviewed in Soltesz and Losonczy, 2018). The superficial CA1 PCs are immunopositive for a Ca^{2+} binding protein calbindin, which may function as an intra-neuronal Ca^{2+} buffering system (Baimbridge et al., 1991). Moreover, another study demonstrated transcriptional gradients along the radial axis (Cembrowski et al., 2016), which could manifest in differences in protein expression and functional properties (reviewed in Soltesz and Losonczy, 2018). The heterogeneity along the radial axis is complemented with spatial gradients in the dorsoventral axis (reviewed in Strange et al., 2014) and proximodistal axis (reviewed in Igarashi et al., 2014). The PCs located in dorsal hippocampus show more precise place fields compared with the more diffuse place fields of ventral hippocampal place cells (Jung et al., 1994; reviewed in Basu and Siegelbaum, 2015). CA1 PCs also differ in their dendritic morphology (Bannister and Larkman, 1995), connectivity with INs (Lee et al., 2014), activity during theta oscillations (Mizuseki et al., 2011) and sharp-wave ripples (Valero et al., 2015) *in vivo*.

The inhibitory neurons of the hippocampus, which release gamma aminobutyric acid (GABA) from their terminals, are even more diverse with respect to their functional, anatomical properties and neurochemical content (Klausberger and Somogyi, 2008; Somogyi, 2010). Distinct types of interneurons (INs) provide subcellular domain-specific GABAergic innervation to PCs, allowing the coordination of multiple glutamatergic inputs through their temporally distinct activity (Somogyi et al., 2014). The two populations of INs that are of interest to my study are the fast-spiking (FS) parvalbumin-positive (PV^+) and the somatostatin (SOM) and metabotropic glutamate receptor 1α (mGluR1α) expressing INs. SOM and mGluR1α-expressing, oriens-lacunosum moleculare (O-LM) and oriens-bistratified (O-Bi) INs of the CA1 area have their soma and dendrites located in stratum oriens and receive facilitating excitatory postsynaptic currents (EPSCs) (Losonczy et al., 2002; Biro, 2005). In contrast, the somata of PV-expressing INs (basket, axo-axonic,

bistratified cells) are located in stratum pyramidale. Due to the expression of Kv3.1b K^+ channel subunit, these cells are able to fire at very high frequencies (Du et al., 1996). Their inputs from PCs display short-term depression (Losonczy et al., 2002). The synaptic outputs of these cells also differ, PV^+ cells innervate the perisomatic region of the PCs, whereas mGluR1α^+ cells innervate the distal dendritic compartments; therefore the two cell classes can exert their inhibitory effects on different afferent pathways.

2.2.2. The hippocampal circuit

The afferents and efferents of the hippocampus are organized in layers in a topographical manner. The main hippocampal input is formed by fibers from the layer II and III of the entorhinal cortex, which form synapses on the dendrites of dentate gyrus granule cells and CA3 PCs; and on the apical dendrites of CA1 PCs respectively (***Figure 2***) (Andersen et al., 2007). These two pathways, the Perforant Path (indirect) and the Temporoammonic Path (direct) transfer different information from the medial and lateral entorhinal cortices: spatial (Zhang et al., 2013) and nonspatial (Hargreaves et al., 2005), or context- and content-related (Knierim et al., 2014) information, respectively (reviewed in Basu and Siegelbaum, 2015). This information is then further processed in the hippocampus (***Figure 2***). The axon terminals of granule cells, the Mossy Fibers, form synapses onto complex spines, the so-called thorny excrescences on the apical dendrites of the CA3 PCs in stratum lucidum. The CA3 PCs form a dense network of reciprocal connections and innervate heavily the dendrites of PCs of the CA2 and CA1 regions in the stratum radiatum and oriens (via the Schaffer Collateral Pathway). They also send axons to the contralateral hippocampus via the anterior commissure (Associational Commisural Pathway) (Andersen et al., 2007; Basu and Siegelbaum, 2015). Recent results provide evidence for additional excitatory inputs of CA1 PCs directly from layer II of medial EC (Kitamura et al., 2014) and also from the CA2 region (Chevaleyre and Siegelbaum, 2010). The CA2 neurons in turn receive similar direct and indirect inputs as CA1 PCs from the EC, a weaker input from dentate gyrus granule cells through the Mossy Fibers (Kohara et al., 2014), and additional inputs from a number of subcortical regions (Cui et al., 2013; Hitti and Siegelbaum, 2014)

DOI:10.14753/SE.2019.2319

Several types of INs of the hippocampus are innervated by the direct pathway from EC layer III which provides strong feedforward inhibition onto CA1 pyramidal neurons. An important GABAergic input to INs arrives from the medial septum, which was proposed to contribute to the coordination of network activity through parallel, target area- and cell type-selective projections (Unal et al., 2018).

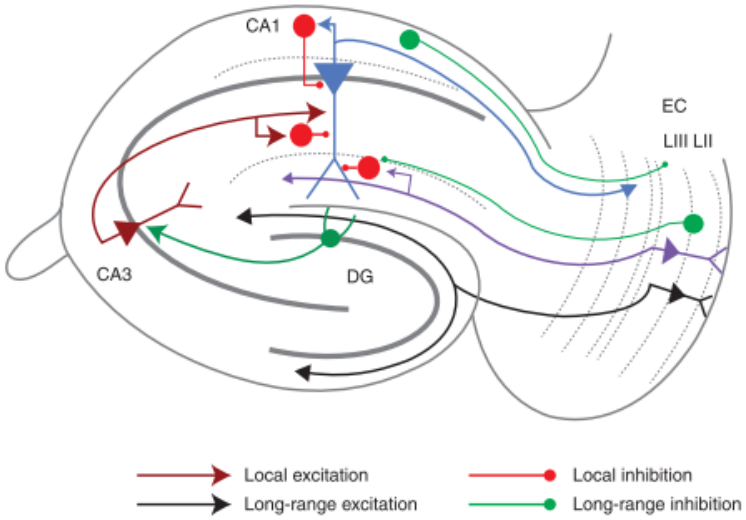

Figure 2. The classical hippocampal circuit.

Perforant path: direct pathway to CA1 PCS: purple; indirect to dentate gyrus (DG) granule cells: black; Mossy fibers: dark green; Schaffer collateral: dark red; CA1 output: blue; long-range inhibitory projections: green; local GABAergic INs and their local projections: red. Arrowheads indicate the direction of information transfer. Modified from Basu and Siegelbaum, 2015.

The major output of the hippocampus is provided by the axons of CA1 PCs (***Figure 2***) which innervate a number of brain regions, including subiculum, medial and lateral EC, perirhinal cortex, prefrontal cortex, restrosplenial cortex, amygdala, nucleus accumbens, the anterior thalamic nuclei, the medial mammillary nucleus, the lateral septum (reviewed in Basu and Siegelbaum, 2015). The GABAergic outputs of some projecting INs innervate the local INs (Melzer et al., 2012) of subiculum and medial EC, medial septum (Jinno et al., 2007; Fuentealba et al., 2008), retrosplenial cortex, indusium gresium (Jinno et al., 2007), striatum (Melzer et al., 2012). In has been suggested that long-range inhibitory projections

may be important for coordinating the timing between the hippocampus and its cortical targets (Buzsáki and Chrobak, 1995; reviewed in Basu and Siegelbaum, 2015).

2.3. Glutamatergic synaptic transmission

Synapses are specialized sites where neurons communicate in a spatially and temporally precise manner. Currently, two major types of synapses are known to exist: electrical and chemical. Electrical synapses provide instantaneous signal transmission via gap junctions; most synapses are however, chemical and are capable of highly complex signaling (Kandel et al., 2013). I will present in more details the chemical synaptic transmission.

2.3.1. Anatomical and molecular structure of the synapse

Chemical synapses (hereafter synapses) are close appositions of specialized regions of the plasma membranes of the pre- and postsynaptic cells (***Figure 3***), containing electron-lucent synaptic vesicles (SV), of a size of ~40 nm (Palay and Palade, 1955) which store the neurotransmitters. The vesicles are intercalated in a hexagonal grid of dense projections anchored to an actin scaffold by synapsin (Akert et al., 1972; Pfenninger et al., 1972; reviewed in Südhof, 2012). Those vesicles that are in contact with the plasma membrane are called docked vesicles (***Figure 3***); they seem to localize randomly over the AZ area (Schneggenburger et al., 2012) and are believed to be set for fusion and release of the neurotransmitter.

The synaptic vesicle exocytosis is spatially restricted to the active zone (AZ), marked by an electrodense material at the precise opposition of the plasma membranes (Gray, 1963; reviewed in Südhof, 2012). This is surrounded by the perisynaptic zone which is the site of synaptic vesicle endocytosis, contains presynaptic receptors (e.g.: $GABA_B$, group III metabotropic glutamate receptors - which can regulate synaptic activity) and proteins involved in membrane trafficking and recycling of synaptic vesicles.

DOI:10.14753/SE.2019.2319

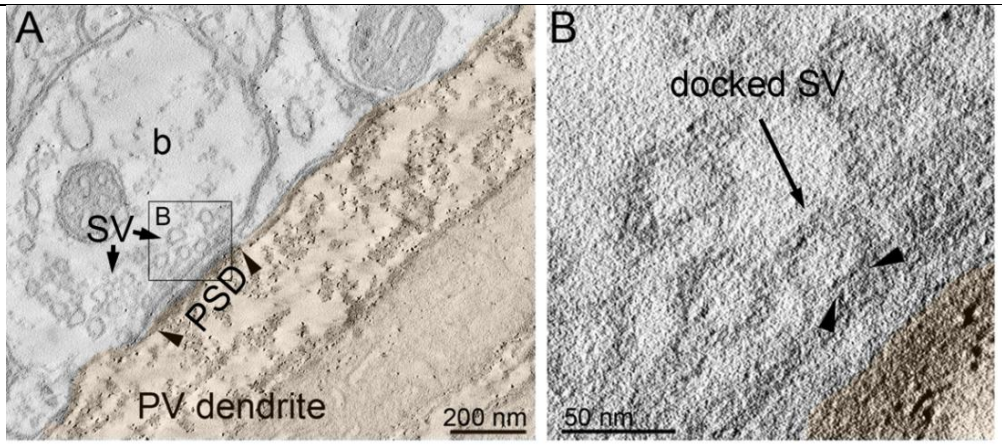

Figure 3. Electron tomograph of an excitatory synapse.

(A) Electron tomographic subvolume of a CA3 PC axon terminal establishing asymmetric synaptic contact (arrowheads demarcate the edges of the synapse) on a PV^+ dendrite (labeled with preembedding peroxidase reaction). (B) Higher-magnification view of the boxed area showing a docked vesicle. Abbreviations: SV, synaptic vesicle; PSD, postsynaptic density. Modified from Éltes et al., 2017, experiment of Noemi Holderith.

The AZs are composed of specialized, evolutionarily conserved proteins: RIM (central organizers of the AZ), Munc13 (mediates vesicle priming), RIM-BP (links Ca^{2+} channels to RIM), α-liprin, ELKS (synapse formation), piccolo and bassoon (provide presynaptic skeleton) which are part of the secretory apparatus, and transsynaptic cell-adhesion molecules (e.g. neurexins). Components of the release machinery (SNARE complex, Munc18) are also present; however, these are not enriched in the AZs but distributed all over the plasma membrane (reviewed in Südhof, 2012; Kandel et al., 2013). The AZs contain P/Q- (Cav2.1) and N-type (Cav2.2) Ca^{2+} channels, which are responsible for the release, and also R-type (Cav2.3) Ca^{2+} channels (Holderith et al., 2012; Parajuli et al., 2012; Schneggenburger et al., 2012; reviewed in Südhof, 2012; Althof et al., 2015; Lenkey et al., 2015; Éltes et al., 2017). The P/Q- and N-type channels are enriched at the AZs of hippocampal glutamatergic and GABAergic, and calyx of Held terminals (Kulik et al., 2004; Holderith et al., 2012; Althof et al., 2015; Lenkey et al., 2015; Nakamura et al., 2015; Éltes et al., 2017). Their density in the CA3 PC terminals correlates linearly with the AZ area

(Holderith et al., 2012; Althof et al., 2015) and they are distributed nonuniformly, arranged in clusters (Südhof, 2012a; Althof et al., 2015; Nakamura et al., 2015).

The presynaptic membrane communicates with the postsynaptic membrane through a 20-40 nm synaptic cleft, where the neurotransmitters are released. The postsynaptic membrane contains postsynaptic receptors (e.g.: AMPA, NMDA in excitatory, $GABA_A$ and $GABA_B$, GlyR in inhibitory synapses) and several regulatory proteins embedded in the postsynaptic density (Kandel et al., 2013).

2.3.2. Synaptic release

Synaptic transmission is initiated by an action potential (AP), that depolarizes the presynaptic membrane, and therefore opens the voltage-gated Ca^{2+} channels (VGCC) (Del Castillo and Katz, 1954; Borst and Sakmann, 1996). Due to the low intracellular concentration of Ca^{2+} at rest and due to effective [Ca^{2+}] buffering capabilities (mobile buffers, intracellular stores), Ca^{2+} ions are very efficient chemical signals (Kandel et al., 2013). The transient increase in its concentration induces exocytosis of the synaptic vesicles (Katz and Miledi, 1967; reviewed in Sudhof, 2004) in a highly cooperative manner (Dodge and Rahamimoff, 1967). The ultrafast speed of neurotransmitter release, not much slower then the actual opening of the VGCC (~ 100 μs), indicates that a release machinery must exist in a primed and ready state (Sabatini and Regehr, 1999; reviewed in Südhof, 2012b, 2013a, 2013b).

Synaptic vesicle proteins, such as synapsins target the vesicles to release sites; whereas the Ca^{2+} channels are recruited to the release sites by the collaboration of two families of evolutionary conserved active-zone proteins, RIMs and RIM-BPs (binds Ca^{2+} channels). The interaction of RIM with Munc13 and vesicular Rab3/ Rab27 GTPases results in the docking of synaptic vesicles (***Figure 4***). Additionally, Munc13 serves as a catalyzer of priming of vesicles for fusion (Wang et al., 1997; Kaeser et al., 2011; reviewed in Südhof, 2013a, 2013b). Recent results demonstrated a role of Munc13-3 in the regulation of developmental localization of Cav2.1 (P/Q-type) and Cav2.2 (N-type) Ca^{2+} channels and of the coupling distance between release sensors and Ca^{2+} channels at parallel fiber-to-Purkinje neuron synapses (Kusch et al., 2018).

DOI:10.14753/SE.2019.2319

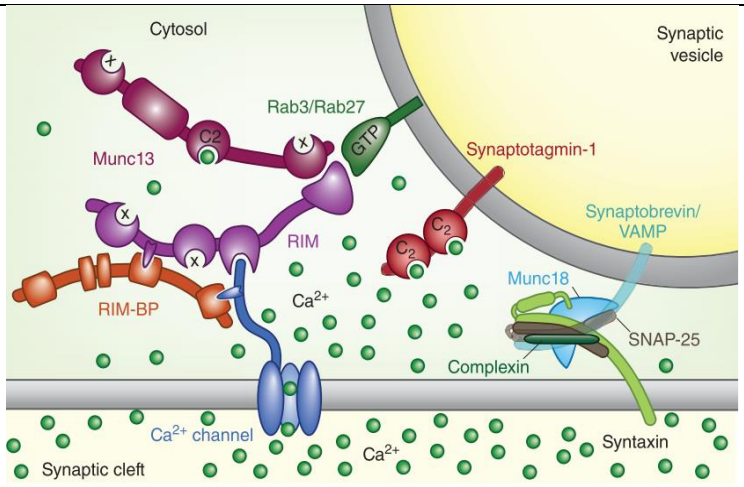

Figure 4. Recruitment of Ca^{2+} channels and the docking of vesicles at release sites.
Figure from (Südhof, 2013b).

In the first step of the priming, two proteins located on the plasma membrane (syntaxin and SNAP-25) form a complex (the SNARE complex) with the synaptic vesicle protein synaptobrevin (Söllner et al., 1993a). The zippering of the SNARE complexes forces the two membranes into close proximity, destabilizes their hydrophilic surfaces and initiates fusion (Priming I on ***Figure 5***). The sensors of the Ca^{2+} ions, the synaptotagmins also bind to syntaxin-1 of the SNARE complexes (Bennett et al., 1992; Söllner et al., 1993b; Li et al., 1995; reviewed in Südhof, 2013b, 2013a). Then, the calcium-activated synaptotagmin displaces complexin (a co-factor for synaptotagmin which functions both as a clamp and as an activator of calcium- triggered fusion (McMahon et al., 1995; Maximov et al., 2009)), and tiggers fusion-pore opening (Priming II on ***Figure 5***). Binding of Munc18-1 protein to syntaxin (full trans-SNARE complex) opens the fusion pore (Hata et al., 1993; Dulubova et al., 1999; reviewed in Südhof, 2013b, 2013a).

Fusion-pore expansion transforms the initial trans-SNARE complexes into cis-SNARE complexes (Fusion completion on ***Figure 5***) that are disassembled by the specialized ATPase NSF. During the multiple cycles of association and dissociation, the function of the SNARE complex is maintained by chaperones: cysteine string proteins and synucleins. The continued association of Munc18-1 to SNARE complexes throughout their assembly/ disassembly cycle is essential for fusion (Khvotchev et al., 2007; reviewed in Südhof, 2013b, 2013a; Zhou et al., 2013)

DOI:10.14753/SE.2019.2319

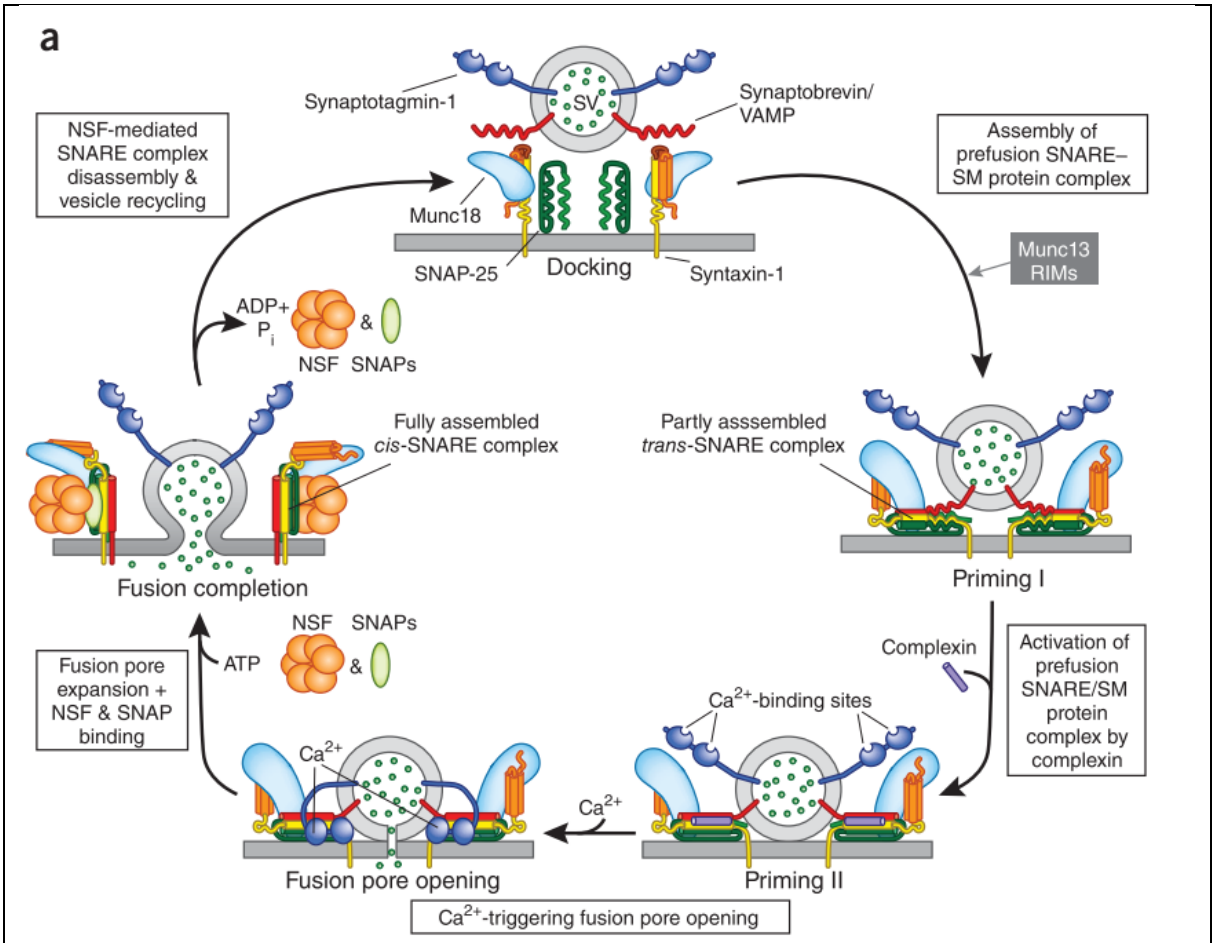

Figure 5. Key proteins regulating priming of synaptic vesicles, fusion of the membranes, pore opening and neurotransmitter release. (a) Overview of the protein complex assembly for synaptic release. (b) Expanded view of the primed vesicle fusion complex. Figure from (Südhof, 2013b).

The pioneering work of Katz revealed that neurotransmitter release (at the end-plate of frog muscle) results in a postsynaptic response that is composed of several postsynaptic potentials (PSPs) of a fixed size which are released in an all-or-none manner (Del Castillo and Katz, 1954). In most neurons however not all APs, but only 10 - 20% of them, are able

to trigger the neurotransmitter release (Goda and Südhof, 1997; reviewed in Sudhof, 2004). The P_r depends on the number of release ready vesicles, the Ca^{2+} concentration in the terminal, and the coupling of Ca^{2+} and vesicle fusion. Because these factors can be modulated by several mechanisms (e.g.: regulation of Ca^{2+} channel function, modulation of release machinery proteins, regulation of Ca^{2+} entry by the AP waveform or by different Ca^{2+} buffering capabilities, different composition of Ca^{2+} channels), the P_r can differ widely between different connections and even from bouton to bouton of the same axon (Atwood and Karunanithi, 2002; Nusser, 2018). The variability in the number of successfully released quanta in concert with the variability in the number of synaptic contacts and the quantal size (size of the postsynaptic depolarization caused by the release of a single quanta) results in the varying amplitude of the PSP (Katz and Miledi, 1967; reviewed in: Sudhof, 2004; Branco and Staras, 2009; Kandel et al., 2013). Moreover, the P_r defines the way a synapse adapts to dynamic inputs by being able to change with short-term activity. The PSP at a synapse with high initial P_r will decrease upon short-term repetitive activation (short-term depression), whereas at low initial P_r synapses the amplitude will increase (short-term facilitation) (reviewed in Branco and Staras, 2009).

The hypothesis that these differences in synaptic properties are underlied by distinct molecular mechanisms is currently generally accepted. The multiple isoforms of Ca^{2+} sensors (synaptotagmins), the four presynaptic VGCC subtypes, additionally the several isoforms of other synaptic proteins can potentially form thousands of combinations of presynaptic functional properties (Nusser, 2018).

2.4. Diversity of synaptic properties

Assessing the efficacy and reliability of synaptic transmission in a dynamic system, in which a plethora of connection types respond differently to diverse patterns of presynaptic firing activity, are crucial to understand the ongoing information transfer. Synapses formed by heterogeneous, or even apparently homogeneous pre- and postsynaptic cells demonstrate remarkable diversity regarding their synaptic properties (Nusser, 2018). A special form of this diversity is the so-called target cell type-dependent form, which results in the transmission of different aspects of information coded in a complex spike train to distinct

postsynaptic cell types by the same PC axon (Markram et al., 1998b, 1998a; Reyes et al., 1998; Pouille and Scanziani, 2004; Koester and Johnston, 2005).

2.4.1. Postsynaptic target cell type-dependent differences in synaptic properties

Release probability and the paired-pulse ratio have been demonstrated to show inverse correlation. Therefore, performing short-term plasticity experiments and calculating the paired pulse ratio between the postsynaptic responses evoked by the first and last APs in a train will allow the estimation of the release probability of those synapses. The first evidence for target cell-type dependent diversity of synaptic properties was revealed in the early 1970s in case of motoneuron synapses, which innervated multiple muscles with differing release probabilities and short-term plasticity (Parnas, 1972; Robitaille and Tremblay, 1987; Katz et al., 1993). Two decades later, Thomson reported a similar observation in the neocortex, where PC-to-PC connections showed paired-pulse depression, whereas PC-to certain IN synapses displayed robust short-term facilitation (Thomson, 1997). Later, a similar phenomenon was found in the hippocampus (Ali and Thomson, 1998; Ali et al., 1998; Scanziani et al., 1998; Losonczy et al., 2002), where combined functional and molecular neuroanatomical approaches led to the identification of the postsynaptic IN types. SOM and mGluR1α-expressing, O-LM and O-Bi INs of the CA1 area receive facilitating EPSCs with low initial P_r, whereas synaptic inputs onto FS PV-expressing INs (e.g., basket, axo-axonic, bistratified cells) display short-term depression and have high initial P_r (Atwood and Karunanithi, 2002; Losonczy et al., 2002; Biró et al., 2005; Koester and Johnston, 2005; Mercer et al., 2012).

A candidate protein bestowing different P_r and short-term plasticity to axon terminals was mGluR7, a metabotropic glutamate receptor that shows postsynaptic target cell type-dependent differences in its presynaptic density (Shigemoto et al., 1996). However, a group III mGluR-specific antagonist failed to abolish the differences in short-term plasticity of synapses expressing or lacking mGluR7 (Losonczy et al., 2003). More recently, Sylwestrak and Ghosh (Sylwestrak and Ghosh, 2012) identified the extracellular leucine-rich repeat fibronectin-containing protein 1 (Elfn1) as a key molecule in regulation of short-term facilitation. This protein is selectively expressed postsynaptically in O-LM cell somata and

dendrites. When Sylwestrak et al. overexpressed it in PV^+ INs, the short-term properties of PC-to-PV IN synapses was converted from short-term depression to short-term facilitation (***Figure 6***). Their results provide evidence that Elfn1 imposes facilitating neurotransmitter release to the presynaptic axon terminals (Sylwestrak and Ghosh, 2012).

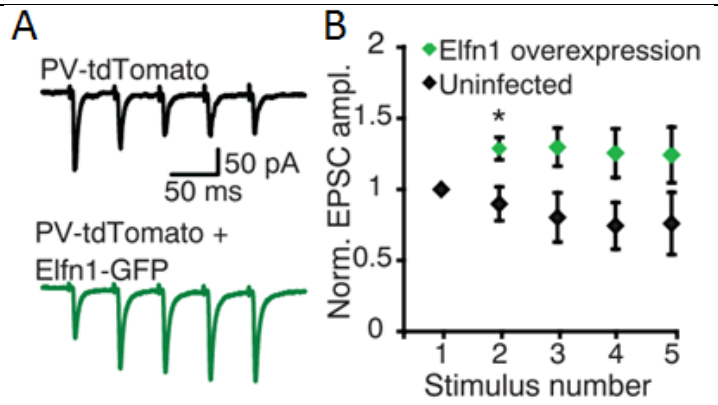

Figure 6. Overexpression of Elfn1 in PV^+ INs converts the short-term synaptic properties of PC-to-PV IN synapses.

(A) Response of control and Elfn1-expressing PV^+ neurons to five stimuli delivered to the alveus at 20 Hz. (B) Quantification of short-term plasticity in Elfn1 overexpressing PV^+ cells. Modified from Sylwestrak and Ghosh, 2012.

There is little data available regarding the mechanisms through which such proteins as Elfn1 can regulate the low initial P_r of PC-to-O-LM cell facilitating synapses, and high initial P_r of PC-to-PV IN depressing synapses. In 2001 Rozov et al. put forward an elegant hypothesis based on their experiments involving fast and slow Ca^{2+} buffers (Rozov et al., 2001). Intracellular loading of pyramidal neurons with the fast and slowly acting Ca^{2+} buffers, BAPTA and EGTA respectively, differentially reduced transmitter release in these two types of terminals. Unitary excitatory postsynaptic potentials (EPSPs) evoked by PC stimulation were reduced by presynaptic EGTA to 50% by much lower concentrations of buffers in case of bitufted neurons compared to multipolar neurons. The lower effectiveness of the buffers suggest a longer diffusional distance between release sites and Ca^{2+} channels at PC-to multipolar IN synapses. Therefore, they postulated that the low initial P_r of facilitating cortical PC synapses can be explained by a larger coupling distance between VGCC and Ca^{2+} sensors on the docked vesicles compared with the high P_r PC synapses on

FS INs (***Figure 7***). Assuming similar Ca^{2+} sensors and docked vesicle distributions, this would suggest a lower average Ca^{2+} channel density within the AZs of low P_r synapses (Rozov et al., 2001).

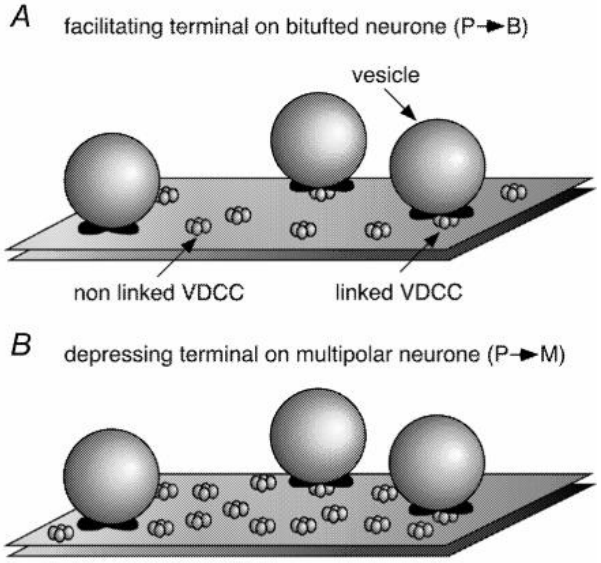

Figure 7. Possible distribution of Ca^{2+} channels and vesicle release sites.
(A) bouton of a pyramidal cell axon contacting a bitufted cell, (B) bouton of a pyramidal cell axon contacting a multipolar cell. Voltage-dependent Ca^{2+} channels (VDCC) can be linked to a vesicle release site or non-linked. Figure from (Rozov et al., 2001).

2.5. Diverse synaptic properties shaping network activity and behavior

Target cell-type dependent activation of INs results in differences in information processing, due to the different recruitment at low and high frequencies of short-term depressing and facilitating synapses, respectively (Blackman et al., 2013). The INs, due to their diverse morphological, functional, molecular, properties have been proposed to play a key role in shaping network activity (Isaacson and Scanziani, 2011; Kepecs and Fishell, 2014) and neuronal assembly formation (reviewed in Holtmaat and Caroni, 2016). Recent results provide evidence that distinct cognitive functions can be based on heterogeneous parallel circuit modules, and not random synaptic connections between homogeneous populations of neurons (Soltesz and Losonczy, 2018). One such example is that of deep CA1 PCs, which receive stronger excitatory input from MEC and from hippocampal area CA2, weaker excitatory input from CA3 PCs, and larger inhibitory currents from PV^+ basket cells, compared to the superficially located CA1 PCs (***Figure 8***) (Lee et al., 2014; reviewed in Soltesz and Losonczy, 2018). These deep CA1 PCs are more active and more likely to form place fields than superficial neurons (Mizuseki et al., 2011) and their place cell representation

of the goal, during a goal-oriented learning task, was found to be more predictive of performance compared to the superficial neurons (Danielson et al., 2016; reviewed in Soltesz and Losonczy, 2018). This different relationship of CA1 PC subpopulations to behavior is hypothesized to be due to the distinct perisomatic inhibitory interactions between separate output channels (***Figure 8***) (Soltesz and Losonczy, 2018).

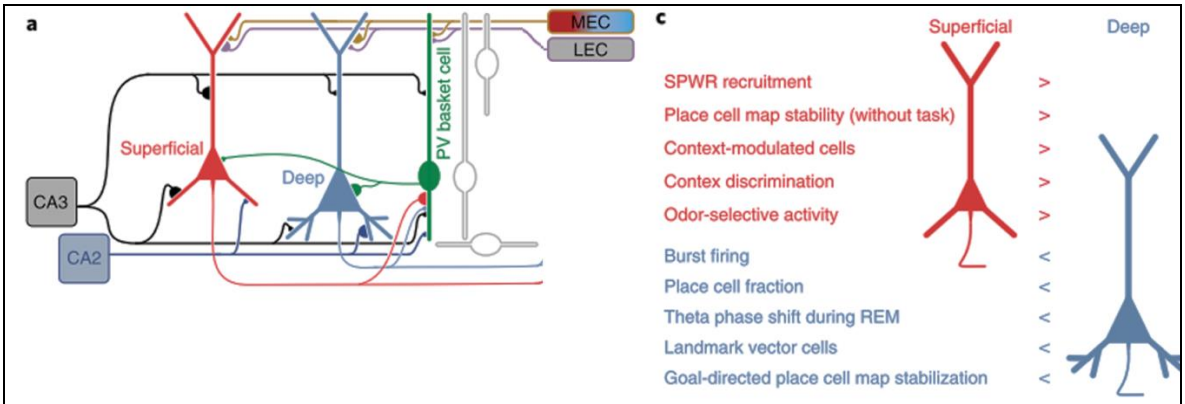

Figure 8. Different connectivity and synaptic properties of radially defined CA1 PC subpopulations can potentially result in their different recruitment during behavior. (A) Biased microcircuits and afferent-efferent connectivity of superficial and deep CA1PCs. (C) Differential behavioral functions of radially defined CA1PCs subpopulations. Abbreviations: MEC, Medial Entorhinal Cortex Modified; LEC, Lateral Entorhinal Cortex. Modified from (Soltesz and Losonczy, 2018).

Understanding the extent to which diverse synaptic properties shape neuronal circuits, is critical to elucidate how neuronal activity is transformed into mnemonic processes and complex behaviors. For this neuroscientists must track the dynamics of large ensembles of morphologically and neurochemically identifiable cells in behaving animals, over timescales equivalent with long-term memory formation (Jercog et al., 2016). However, the methods currently available for exploring synaptic transmission *in vivo* are limited.

2.6. Limitations of methods exploring synaptic transmission *in vivo*

The ideal *in vivo* recording method is expected to monitor simultaneously the activity of large populations of neurons and to capture the temporal dynamics of their spiking activity during complex behaviors. In order to understand the function of neuronal networks the

recording method should also grant the morphological and molecular identification of neurons.

2.6.1 *In vivo* electrophysiological recordings

In vivo single cell electrophysiological recordings (i.e.: intracellular, cell attached, juxtacellular) have the required temporal resolution, and permit the *post hoc* identification and molecular analysis of the cells, but they allow the monitoring of the activity of only a relatively modest number of cells and only for short periods. Moreover, single cell recordings do not provide the opportunity to investigate the simultaneous activity of neuronal populations, which is necessary in order to decipher how the combination of their activity is coding an environment or a certain behavior. Electrical recordings of large numbers of neurons – populations that are statistically representative - is currently feasible by using tetrodes, silicon probes or multi-shank probes (Buzsáki, 2004). These techniques are invasive and cause local tissue damage. These large-scale electrophysiological recordings provide limited information about the identity of the recorded cells and face further limitations, such as difficulties in spike sorting (Buzsáki, 2004).

2.6.2. *In vivo* optical recordings

The introduction of two-photon (2P) microscopy (Denk et al., 1990) in concert with improvement of the signal to noise ratio (SNR) of the fluorescent probes revolutionized the field of optical imaging promoting the real-time investigation of biological processes (Helmchen and Denk, 2005; Svoboda and Yasuda, 2006). Optical imaging techniques have the advantage of monitoring AP-evoked fluorescent changes simultaneously in a large number of individual neurons and in a chronic manner, allowing the examination of activity changes during the course of learning, life experience, brain development, or disease progression. Moreover, the genetically encoded activity indicators enable selective interrogation of genetically defined neuronal subtypes, or of cells with specific patterns of anatomical connectivity permitting the sophisticated analyses of ensemble neural activity (reviewed in Broussard et al., 2014; Jercog et al., 2016; Lin and Schnitzer, 2016). The neuronal damage can also be minimized in case of superficially located areas, such as the

neocortex, because most optical preparations are minimally invasive and offer the possibility of placing the probe millimeters away from the area of interest.

The most ideal optical method would be the direct imaging of voltage changes, the primary signal of interest, using genetically encoded voltage indicators (GEVI). However, the fast nature of the voltage signal requires an indicator with very fast kinetics and high sensitivity to secure an acceptable signal to noise ratio. The necessary membrane targeting of the voltage sensitive molecules causes additional difficulties in the implementation of this imaging method (Broussard et al., 2014). Sensors with response dynamics that are compatible with recording of millisecond timescale computations are available in cultured cells; however, their use for *in vivo* imaging at single cell resolution is still sporadic, due to critical shortcomings such as low brightness, imperfect membrane localization, or low signal to noise ratio (Broussard et al., 2014; Knöpfel et al., 2015).

Neuronal spiking activity can also be indirectly monitored by recording AP-evoked [Ca^{2+}] changes with Ca^{2+} indicators. The intracellular [Ca^{2+}] is determined by the balance between calcium influx and efflux as well as by the exchange of calcium with internal stores and buffers, and in most neurons is ~50 - 100 nM. During electrical activity, the influx of Ca^{2+} through VGCC results in a transient increase of [Ca^{2+}] to levels that are ten to hundred times higher (Berridge et al., 2000; Schwaller, 2010; reviewed in Grienberger and Konnerth, 2012). The large concentration difference makes monitoring [Ca^{2+}] a potent measure of neuronal activity. The first high affinity, high signal to noise ratio genetically encoded Ca^{2+} indicator was developed by Nakai et al. in 2000 (Nakai et al., 2001) and was named G-CaMP. This probe contains a circularly permutated GFP (cpGFP) that is connected to the M13 fragment of the myosin light chain kinase (a target sequence of calmodulin), and to calmodulin. Upon Ca^{2+} binding to calmodulin, a chain of conformational changes leads to an increase of cpEGFP fluorescence intensity (Nakai et al., 2001). The palette of genetically encoded Ca^{2+} indicators was expanded in the following years with indicators demonstrating improved affinity, kinetics; and with the addition of blue and red hues (Tian et al., 2009; Zhao et al., 2011; Akerboom et al., 2012; Ohkura et al., 2012; Chen et al., 2013; Badura et al., 2014; Podor et al., 2015; Lin and Schnitzer, 2016) . The use of red indicators was expected to improve the maximal imaging depth and allow parallel optical manipulation of neuronal

activity, however they show photoswitching behavior or partial saturation at high number of APs, and accumulation in lysosomes which reduces the signal to noise ratio for *in vivo* imaging (Dana et al., 2016; Lin and Schnitzer, 2016). Other promising genetically encoded Ca^{2+} indicator candidates are the ratiometric indicators. Ratiometric imaging with Förster resonance energy transfer-based indicators have the advantage to enable the reduction of motion related artefacts during *in vivo* measurements. Their sensitivity only recently became comparable to that of synthetic dyes (Twitch family), however still show slower decay kinetics (Thestrup et al., 2014; Lin and Schnitzer, 2016).

The GCaMP family of genetically encoded Ca^{2+} indicators underwent successive structure-guided mutagenesis over the past decade to improve sensitivity, dynamic range, SNR and brightness, resulting in the GCaMP6 family with sensitivities comparable to those of synthetic Ca^{2+} indicators (Nakai et al., 2001; Tian et al., 2009; Akerboom et al., 2012; Chen et al., 2013). Even though more recent developments yielded more sensitive (GCaMP7) or faster (GCaMP6fRS09, GCaMP6f91) indicators, these show more pronounced nonlinearity and saturate at lower Ca^{2+} levels; or have lower sensitivity, respectively (Ohkura et al., 2012; Badura et al., 2014; Podor et al., 2015). Thus, GCaMP6f became the most widely used genetically encoded Ca^{2+} indicator in behaving animals because it combines high sensitivity and large dynamic range with fast kinetics (Jercog et al., 2016).

2.6.3. Inference of spiking activity from fluorescence transients

Despite the improved properties of indicators, APs cannot be directly inferred from the fluorescent transients with millisecond temporal resolution (Jercog et al., 2016; Lin and Schnitzer, 2016). To overcome this limitation, several approaches have been developed to determine the AP firing underlying the fluorescent traces: template-matching (Greenberg et al., 2008; Grewe et al., 2010; Oñativia et al., 2013), deconvolution (Yaksi and Friedrich, 2006; Park et al., 2013), approximate Bayesian inference (Vogelstein et al., 2009; Pnevmatikakis et al., 2016) and supervised learning techniques (Sasaki et al., 2008; Theis et al., 2016), but the accuracy of estimation for high frequency events is still < 40-60% (Lin and Schnitzer, 2016; Theis et al., 2016). Deneux et al. improved spike estimation performance by introducing a baseline drift and nonlinearity of the indicator (Deneux et al.,

2016). They define baseline drifts as low frequency, large amplitude baseline fluctuations, which probably reflect slow changes in [Ca^{2+}] which are unrelated to the cell's firing activity. The nonlinearity parameters are: saturation γ, Hill exponent n or polynomial coefficient. MLspike software uses a maximum-likelihood approach to find the most likely underlying spike train (***Figure 9.***).

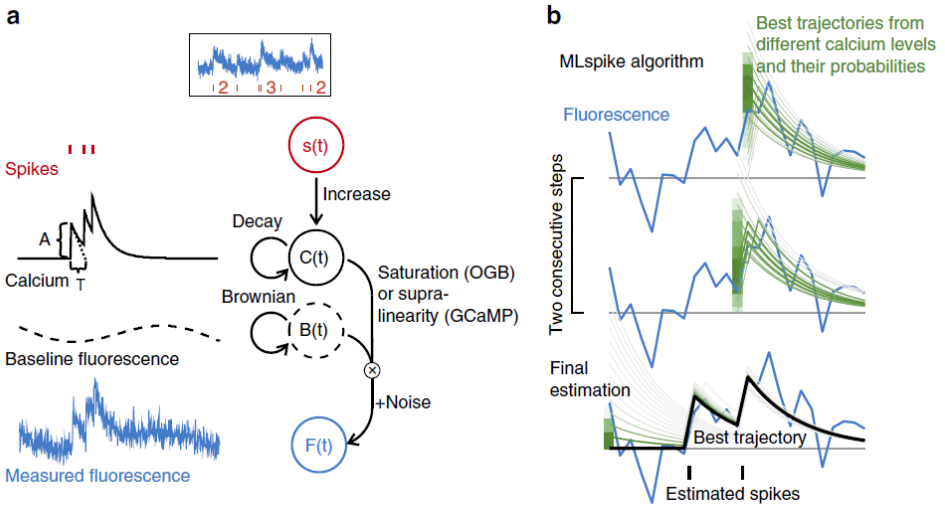

Figure 9. ML spike physiological model and algorithm: Upon emission of s(t) spikes, intracellular [Ca^{2+}] C(t) is driven by an increase A (the unitary calcium response) X s(t), then decays to the resting value with time constant τ. The measured fluorescence F(t) is the product of a drifting baseline fluorescence B(t) with a nonlinear function of C(t) accounting for dye saturation and GCaMP nonlinearities; a noise term is added.
(b) 'MLspike' algorithm illustrated on a schematic example without baseline drift. (top and middle) The probabilities (white-green colour code) of 'best trajectories' originating from all possible calcium values (y axis, for display purposes same scale as fluorescence) at time t (x axis) are calculated, iteratively for decreasing time. Figure and explanation from (Deneux et al., 2016)

Most of these algorithms are based on the estimation of the model parameters from a limited number of available simultaneous optical and electrical recordings, which might not capture the full range of the key parameters (Deneux et al., 2016; Theis et al., 2016).

The spike inferring accuracy is known to depend on peak amplitude and decay kinetics of single AP-evoked (unitary) [Ca^{2+}] transients, SNR, baseline fluctuations and the

nonlinear nature of genetically encoded Ca^{2+} indicators (Wallace et al., 2008; Lütcke et al., 2013; Wilt et al., 2013; Rose et al., 2014; Deneux et al., 2016). These parameters not only vary among different cell types, preparations and optical recording conditions, but also among individual cells of the same type (Mao et al., 2008; Tian et al., 2009; Akerboom et al., 2012; Ohkura et al., 2012; Zheng et al., 2015). A key factor that determines many of these parameters is the concentration of the Ca^{2+} indicator: low concentrations of indicators provide signals with higher peak amplitudes, lower SNR and faster kinetics (Hires et al., 2008; Broussard et al., 2014; Dana et al., 2014; Rose et al., 2014). Unfortunately, the concentration/expression of the genetically encoded Ca^{2+} indicators cannot be controlled and made uniform among the transfected cells when they are expressed with viral vectors, leaving an inherent source of error for transforming the fluorescent traces to spike trains. Understanding the exact relationship of indicator expression level and variability of unitary $[Ca^{2+}]$ transients, their SNR and nonlinearity, and how these parameters influence the performance of spike inferring algorithms is crucial to achieve higher accuracy.

DOI:10.14753/SE.2019.2319

3. OBJECTIVES

The general aim of my PhD work is to investigate glutamatergic synaptic transmission.

In the first part of my PhD thesis I pursue to answer the question of what mechanism underlies the target cell type-dependent differences in release probability (Éltes et al., 2017). For this I specifically addressed the following questions:

1. What is the short-term plasticity of CA3 PC-to-PV^+ or -$mGluR1\alpha^+$ IN synapses?
2. Does the postsynaptic presence of Elfn1/2 determine the short-term plasticity at PC-to-$mGluR1\alpha^+$ INs?
3. Are there target cell type-dependent differences in the $[Ca^{2+}]$ transients in axon terminals synapsing onto these two populations of INs?
4. Do presynaptic kainite receptors contribute to the $[Ca^{2+}]$ transients in the $mGluR1\alpha^+$ dendrite-targeting boutons?
5. Is the contribution of P/Q and N type VGCCs to the Ca^{2+} influx different in these two populations of axon terminals?
6. Is the degree of $[Ca^{2+}]$ buffering similar in the PV^+- or $mGluR1\alpha^+$-dendrite targeting boutons?

Investigation of these properties and their functional consequences on network activity and during behavior is hampered by the inaccurate spike inference from the optically recorded fluorescent transients. Therefore, in the second part of my PhD work I aimed to understand the relationship between the expression level of the most widely used genetically encoded Ca^{2+} indicator, GCaMP6f and the variability in $[Ca^{2+}]$ transients, their signal to noise ratio and nonlinearity. I also aimed to elucidate which of these parameters is a key source of error in spike inference and to develop a procedure that improves the spike estimation (Éltes et al., 2019). For this, I asked the following specific questions:

1. How large is the variability in the unitary $[Ca^{2+}]$ transients and in the GCaMP6f expression level in CA1 hippocampal PCs?
2. What is the relationship of the GCaMP6f expression level and the peak amplitude of unitary $[Ca^{2+}]$ transients?

3. Is there a cell-to-cell variability in the temporal summation of GCaMP6f [Ca^{2+}] transient? What is the relationship of the supralinearity and of the expression level, or the size of unitary responses?

4. How does variability in the amplitude, kinetics and supralinearity affect the precision of spike estimation?

5. Can we estimate the peak amplitude of the unitary [Ca^{2+}] signals? Can spike inference performance be improved by using the peak amplitude of an estimated unitary [Ca^{2+}] transient in the spike inferring algorithm?

Contributions:

In the first part of my thesis, the short-term plasticity measurements of CA3 PC and PV^{+}/mGluR1α^{+} INs, and the [Ca^{2+}] imaging from boutons of CA3 PCs are pooled from my recordings and that of my collaborator, Noémi Holderith's (for exact contribution see ***Table 1***; Figures 1 and 2 from Éltes et al., 2017). The Neurolucida reconstructions were performed by Borbála Bolonyai.

In the second part of my thesis the simulations were conducted together with my collaborator, Miklós Szoboszlay. He implemented the MLspike algorithm (Deneux et al., 2016) and performed initial simulations and analysis. My collaborator, Szigeti Katalin performed anti-GFP immunoreactions and quantified native GCaMP6f and anti-GFP intensities. She also performed 3-dimensional (3D) reconstructions of the somata of a subselected population of the recorded cells, measured their surface-to-volume ratios and helped with the *post hoc* identification of some recorded cells (Éltes et al., 2019).

DOI:10.14753/SE.2019.2319

Table 1. Details of my contribution in the pooled data in the Part I of the thesis.

Experiment name	Figure number	own contribution	contribution of colleagues	own contribution (%)
Short-term plasticity of CA3 pyramidal cell synapses contacting PV+ INs.	**Figures 12, 14**	I recorded 10 cells	Noémi Holderith recorded 6 cells	**62.5%**
Short-term plasticity of CA3 pyramidal cell synapses contacting mGluR1α+ INs.	**Figures 13, 14**	I recorded 4 cells	Noémi Holderith recorded 27 cells	**12.9%**
Short-term plasticity of CA3 pyramidal cell synapses contacting mGluR1α+ and Elfn1/2+ or Elfn1/2- INs.	**Figure 15**	I recorded all the15 cells	-	**100.0%**
[Ca2+] transients in PV+ and mGluR1α+ dendrite-contacting boutons.	**Figure 16**	I imaged 13 PV dendrite-targeting boutons	Noémi Holderith imaged 13 PV dendrite-targeting boutons	**50.0%**
		I imaged 32 mGluR1α dendrite-targeting boutons	Noémi Holderith imaged 29 mGluR1α dendrite-targeting boutons	**52.5%**
Contribution of N/P/Q type [Ca2+] channels to the [Ca2+] transients	**Figure 17**	I recorded all the cells, n = 12 PV targeting boutons , n = 19 mGluR1α targeting botuons	-	**100.0%**
Measurment of decay time constant of [Ca2+] transients in innervating PV+ or mGluR1α+ dendrites with lower dye concentration	**Figure 18**	I recorded all the cells, n = 18 PV targeting boutons , n =35 mGluR1α targeting botuons, n = 439 boutons on unidentified targets	-	**100.0%**

DOI:10.14753/SE.2019.2319

4. MATERIALS AND METHODS

4.1. Animal Care

All experiments were conducted in accordance with the Hungarian Act of Animal Care and Experimentation (1998, XXVIII, section 243/1998) and with the ethical guidelines of the Institute of Experimental Medicine Protection of Research Subjects Committee. All experimental protocols were approved by the Protection of Research Subjects Committee of the Institute of Experimental Medicine. Animals were housed within the vivarium of the Institute in a normal 12 h/ 12h light/dark cycle with food and water available ad libitum. Young experimental rats were kept in a cage with their mothers and were used before weaning; whereas, adult mice from the same litter were kept together in the same cage. The environment of mice was enriched with Sizzle-Pet and cardboard tubes as play tunnels (Akronom).

4.2. PART I: Investigation of the mechanism of target cell-type dependent differences in neurotransmitter release probability

4.2.1. Slice preparation and electrophysiological recordings of CA3 PCs and INs

Male Wistar rats (n = 97, 14 - 17 days old) were killed by decapitation and acute hippocampal slices were prepared as described previously (Holderith et al., 2012; Éltes et al., 2017). Briefly, after decapitation, the brain was quickly removed and placed into an ice-cold cutting solution containing the following (in mM): sucrose, 205.2; KCl, 2.5; NaHCO3, 26; CaCl2, 0.5; MgCl2, 5; NaH2PO4, 1.25; and glucose, 10, saturated with 95% O2 and 5% CO2. Then, 300 μm-thick horizontal slices were cut from the ventral part of the hippocampus using a Leica Vibratome (VT1200S). Slices were incubated in an interface-type holding chamber in ACSF containing the following (in mM): NaCl, 126; KCl, 2.5; $NaHCO_3$, 26; $CaCl_2$, 2; $MgCl_2$, 2; NaH_2PO_4, 1.25; and glucose, 10; saturated with 95% O_2 and 5% CO_2, pH 7.2 - 7.4, at 36°C that was gradually (~1 hour) cooled down to room temperature (22 - 24°C). Experiments were performed at 22 - 24°C up to 6 h after slicing.

Cells were visualized using a Femto2D microscope equipped with oblique illumination and a water-immersion lens (25X, numerical aperture (NA) = 1.05, Olympus,

or 25X, NA = 1.1, Nikon). Whole-cell voltage- or current-clamp recordings were performed from CA3 PCs or INs located in the strata oriens and pyramidale using MultiClamp 700A and B amplifiers (Molecular Devices). Recorded traces were filtered at 3 - 4 kHz and digitized online at 20 kHz. Patch pipettes (resistance 3 - 6 MΩ) were pulled from thick-walled borosilicate glass capillaries with an inner filament. Intracellular solution contained the following (in mM): K-gluconate, 110; KCl, 5; creatine phosphate, 10; HEPES, 10; ATP, 2; GTP, 0.4; and biocytin, 5, pH 7.3; 290 - 300 mOsm. For voltage-clamp recordings of evoked EPSCs in INs, the intracellular solution contained picrotoxin (0.6 - 0.8 mM). For current-clamp recordings and Ca^{2+} imaging in PC axons, 100 or 300 μM Fluo5F (Invitrogen) and 20 μM Alexa Fluor 594 (Invitrogen) were added to the intracellular solution. The firing pattern of the INs was determined with a series of 500 ms long hyperpolarizing and depolarizing current pulses with amplitudes of 125 - 500 pA. A cell was considered fast spiking if the average firing frequency exceeded 70 Hz. For extracellular stimulation, a unipolar stimulating electrode was placed in the stratum oriens at least 100 μm away from the soma.

INs were held at -70 mV and 5 stimuli (0.2 - 0.3 ms duration, 20 - 200 pA) at 40 or 50 Hz with 30 s interstimulus interval (15 - 70 repetitions) were applied. Data from 40 and 50 Hz stimulations were pooled (see ***Figure 14***). Series resistance was monitored and was < 20 MΩ. Pyramidal cells were held at -70 mV (with a maximum of -100 pA DC current) and single APs at 0.05 - 0.016 Hz were evoked with 2- to 4-ms-long depolarizing current pulses (1 - 1.2 nA). Peak amplitude and full width at half-maximal amplitude (FWHM) of the APs were monitored and cells were rejected if any of these parameters changed > 10%.

4.2.2. *In vitro* two-photon [Ca^{2+}] imaging of CA3 PC axon terminals

Experiments were performed with a Femto2D (Femtonics) laser scanning microscope equipped with a MaiTai femtosecond pulsing laser tuned to 810 nm (described in (Holderith et al., 2012). Electrophysiological data and image acquisition were controlled with software written in MATLAB (The MathWorks). Cells were filled for 2 h with a Ca^{2+}-insensitive (20 μM Alexa Fluor 594) and a Ca^{2+}-sensitive fluorophore (100 or 300 μM Fluo5F). Boutons were selected at 150 - 300 μm distances from the soma on the second- and third order collaterals of the main axon in the stratum oriens at 35 - 80 μm slice depth. They were imaged

in line scan mode (scan duration 500 or 1200 ms at 1 kHz, 1 - 3 per minute repetition, 2 - 3 scans averaged for each bouton) with a laser intensity of 2 - 6 mW at the back aperture of the objective lens. Single AP-evoked changes in fluorescence were quantified during the recording as delta$G/R(t)$ = ($F_{green(t)}$ - $F_{rest, green}$)/(F_{red} - $I_{dark, red}$) where $F_{green(t)}$ represents the green fluorescence signal as a function of time, $F_{rest, green}$ is the green fluorescence before stimulation, and $I_{dark, red}$ is the dark current in the red channel (***Figure 10***).

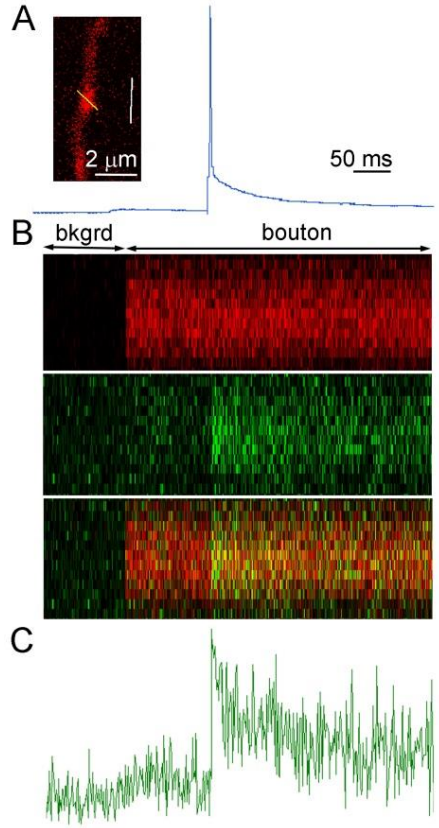

Figure 10. ***In vitro*** **two-photon [Ca^{2+}] imaging of CA3 PC axon terminals.**
(A) A single AP was evoked by a 2 - to 4 ms long depolarizing current pulse. Inset shows the scanned bouton (white line, scanline for background; yellow line, scanline on bouton). (B) Fluorescence intensities in the red (Alexa Fluor 594), green (Fluo-5F) channels, and overlay respectively. Note the abrupt fluorescence change in the green channel upon the AP, and the lack of fluorescence change in the red channel. (C) Raw [Ca^{2+}] trace (from the green channel). All panels are on the same timescale as A and are aligned accordingly. Abbreviations: Bkgrd, background.

To normalize data across batches of dyes, G_{max}/R values were measured by imaging a sealed (tip melted and closed by heating) pipette filled with intracellular solution containing 10 mM $CaCl_2$ for each cell at the same position where the boutons were imaged. DeltaG/R measurements from boutons were divided by G_{max}/R, yielding the reported values of G/G_{max}. The effects of 1 µM ω-CTX MVIIC (diluted in 1 mg/ml BSA; Tocris Bioscience and Alomone Laboratories) were tested by comparing the peak amplitudes of presynaptic [Ca^{2+}]

transients in individual boutons, averaged from two to three consecutive scans, in control conditions, and after 30 min (for ω -CTX MVIIC) of wash-in of the drug.

4.2.3. Identification of the postsynaptic target of the imaged boutons

At the end of the recordings a high resolution image stack of the measured boutons was acquired; after which the slices were fixed in a solution containing 4% paraformaldehyde (PFA), 0.2% picric acid in 0.1 M phosphate buffer (PB), pH 7.4, at 4°C for either 12- 36 h (PV or mGluR1α immunolabeling) or 1 - 3 h (for Elfn1/2 labeling). Slices containing filled PCs were incubated in 10% and 20% sucrose as a cryoprotectant, repeatedly freeze-thawed above liquid nitrogen, embedded in agarose (2%), and resectioned at 70 – 90 μm thickness. Slices containing filled INs were immunolabeled without resectioning.

Sections/slices were washed in 0.1 M PB and blocked in normal goat serum (NGS, 10%) for 1 h made in Tris-buffered saline (TBS; pH 7.4), incubated in the following primary antibodies: mouse anti-PV (1:1000, RRID:AB_10000343; Swant); rabbit anti-PV (1:1000, RRID:AB_1210396; Synaptic Systems), guinea pig anti-mGluR1α (1:1000, RRID:AB_2531897; Frontier Institute; Mansouri et al., 2015), or rabbit anti-Elfn1/2 (1:500, RRID:AB_1079280; Sigma-Aldrich) diluted in TBS containing 2% NGS. After several washes, the following secondary antibodies were applied: Alexa Fluor 488- or Cy5-conjugated goat antimouse or goat anti-rabbit and Cy3-conjugated donkey anti-guinea pig IgGs. Biocytin was visualized with Alexa Fluor 488-conjugated (Invitrogen) or Cy5-conjugated (Jackson Laboratories) streptavidin (1:500). Sections were mounted in Vectashield (Vector Laboratories). Image stacks including the measured axon segment were acquired with an Olympus FV1000 confocal microscope with 20X and 60X (oil-immersion) objectives. The measured boutons were then identified based on superposition of the 2P and *post hoc* acquired confocal image stacks. Contacts between PC boutons and IN dendrites were considered as putative synapses if they had no apparent gap between them in the focal plane.

4.3. PART II. Investigation of variability in GCaMP6f Ca^{2+} transients, its relationship with GCaMP6f expression level and their impact on spike inference accuracy

4.3.1. Stereotaxic viral delivery of GCaMP6f to the CA1 region of the hippocampus

Male FVB/Ant mice (n = 57, 30 - 52 days old) were anesthetized with 100 µl / 10 g body weight of the mixture of Ketamine (625 µl in 10 ml), Xylazin (625 µl in 10 ml) and Pypolphen (250 µl in 10 ml). The head was fixed in a Kopf stereotaxic apparatus (David Kopf Instruments) and a small craniotomy (0.5 - 1 mm) was made bilaterally, above the CA1 region of dorsal hippocampus, at the following coordinates: anterior - posterior: 2.46 - 2.0 mm, medial - lateral: -1.5 mm, dorsal - ventral 1.3 - 1.5 mm. To obtain a sparse expression of the genetically encoded Ca^{2+} indicator GCaMP6f, I used a mixture of AAV9.Syn.Flex.GCaMP6f.WPRE.SV40 (qTiter 7.744e13 GC/ ml, Penn Vector Core) and AAV9.CMV.PI.CRE.rBG (qTiter 5.86e13 GC/ ml, Penn Vector Core) in 1:100 dilution. A volume of 100 nl was injected (2.3 nl steps at a speed of 11 bpm) bilaterally using thin glass pipettes (World Precision Instruments) and a Nanoject II Injector (Drummond Scientific Company). Mice were returned to their cage for at least two weeks before performing *in vivo* imaging or the preparation of acute slices.

4.3.2. Imaging window implant for *in vivo* [Ca^{2+}] imaging

The surgery was performed according to the method of Dombeck et al. (Dombeck et al., 2010) 21 days after virus injection. Briefly, a 73 days old mouse was anesthetized with isoflurane and a craniotomy (~3 mm) was made centered above the left dorsal hippocampus. After removing the dura, the cortex was slowly removed by aspiration. A cannula (3 mm diameter, 1.5 mm long, filled with optical adhesive (Norland Products)) with glass coverslips on both ends was introduced and sealed to the skull with a mix of RelyX Luting cement (3M) and superglue. Once the cement has set, a custom-made head plate (Supertech Instruments) was also cemented to the skull and all exposed skull surface was covered. The animal recovered 5 -15 minutes after surgery.

4.3.3. *In vivo* two-photon [Ca^{2+}] imaging and data analysis

Imaging was performed 9 days after window implant surgery with a Femto2D (Femtonics Ltd., Budapest, Hungary) resonant scanning microscope equipped with a Chameleon Vision (Coherent) femtosecond pulsing laser tuned to 925 nm and a water-immersion lens (16X, NA = 0.8, Nikon). The animal was anaesthetized with isoflurane (4 – 5% for induction, 1 – 1.5% during imaging). A field of view (FOV) of 300 µm x 300 µm was imaged at a frame rate of 32 Hz and a resolution of 0.65 µm / pixel for 10 minutes. After performing rigid motion correction (NonRigid4Reso Toolbox, Femtonics Ltd.) I drew regions of interest (ROIs) by hand around somata and exported the fluorescent traces. The ΔF/F value was calculated as follows: ΔF/F = (Fpeak – Fbaseline) / Fbaseline. A uniform Gaussian filtering was applied to all fluorescent traces and the peak fluorescence was measured as the maximum value of the fluorescence. To correct for drifts in baseline I subtracted the mean baseline measured before each [Ca^{2+}] transient individually. Changes in fluorescence with a SNR >2 (2*SD of the baseline) were considered [Ca^{2+}] transients. To estimate the variability in the ΔF/F caused by variations of the background fluorescence (F_{bk}), I measured F_{bk} in ROIs of similar areas (n = 9) in the vicinity of each GCaMP6f expressing cell. Then, I subtracted its values from each cell's baseline fluorescence. I recalculated the ΔF/F as $\Delta F/F = (F_{peak} - F_{baseline}) / (F_{baseline} - F_{bk})$ with the 9 different F_{bk} values and their mean, and found a mean coefficient of variation (CV) of 0.29 (n = 14 cells, 1 transient for each cell with 10 F_{bk} values). This variance accounts for only 7.3% of the total variability observed in our *in vivo* recordings (CV = 1.07).

4.3.4. Slice preparation for electrophysiological recordings in CA1 hippocampal region from adult mice

Adult male mice (n = 53, 43 - 81 days old for GCaMP6f cell-attached recordings; n = 7, 42 - 59 days old control mice for Flou5F whole-cell recordings) were anaesthetized with 100 µl / 10 g body weight of the mixture of Ketamine (625 µl in 10 ml), Xylazin (625 µl in 10 ml) and Pypolphen (250 µl in 10 ml). Mice were transcardially perfused with an ice-cold cutting solution containing the following (in mM): sucrose, 205.2; KCl, 2.5; $NaHCO_3$, 26; $CaCl_2$, 0.5; $MgCl_2$, 5; NaH_2PO_4, 1.25; and glucose, 10; saturated with 95% O_2 and 5% CO_2.

After decapitation, the brain was quickly removed and placed into the ice-cold cutting solution. 300 μm thick coronal slices were cut from the dorsal part of the hippocampus with a Vibratome (Leica VT1200S). Slices were incubated in an interface-type holding chamber in ACSF containing the following (in mM): NaCl, 126; KCl, 2.5; $NaHCO_3$, 26; $CaCl_2$, 2; $MgCl_2$, 2; NaH_2PO_4, 1.25; and glucose, 10; saturated with 95% O_2 and 5% CO_2, pH 7.2 - 7.4, at 36°C that was gradually (~1 hour) cooled down to room temperature. Experiments were performed at 22 - 24°C up to 6 h after slicing. Cells were visualized using a Femto2D microscope equipped with oblique illumination and a water-immersion lens (25X, NA = 1.1, Nikon). A MultiClamp 700A amplifier (Molecular Devices) was used to obtain cell-attached recordings from CA1 PCs expressing GCaMP6f, and whole-cell voltage-clamp recordings in experiments using the synthetic Ca^{2+} indicator Fluo5F (300 μM). Recorded traces were filtered at 3 - 4 kHz and digitized online at 20 kHz. Patch pipettes (resistance 4 - 7 MΩ) were pulled from thick-walled borosilicate glass capillaries with an inner filament. Recording pipettes for cell-attached recordings were filled with ACSF. For whole-cell experiments the intracellular solution contained the following (in mM): Fluo5F (Invitrogen), 0.3; Alexa Fluor 594 (Invitrogen), 0.02; K-gluconate, 110; KCl, 5; creatine phosphate, 10; HEPES, 10; ATP, 2; GTP, 0.4; and biocytin, 5, pH = 7.3; 290 - 300 mOsm. APs were evoked antidromically by extracellular stimulation (0.2 - 0.3 ms duration, ~500 μA) using a monopolar stimulating electrode, placed at least 100 μm away from the soma, in the stratum oriens/alveus. Several stimulating protocols were used: single stimulus, 5 stimuli at 10 Hz or 50 Hz, 3 stimuli at 100 Hz, 12 stimuli at 0.25 Hz, place cell firing pattern stimuli (timing of spikes from Losonczy et al., 2002 and a burst recovery protocol. For whole-cell recordings, PC were held at -70mV. APs were evoked with 2- to 4 ms-long depolarizing current pulses (1 - 1.2 nA).

4.3.5. *In vitro* two-photon [Ca^{2+}] imaging of somatic GCaMP6f signals and data analysis

Experiments were performed using a Femto2D (Femtonics) laser scanning microscope equipped with a Chameleon femtosecond pulsing laser (Coherent) tuned to 925 nm (as described in Holderith et al., 2012). Somata of CA1 PCs expressing GCaMP6f were imaged in line scan mode (0.5-1 kHz sampling rate) with 10 - 15 mW laser intensity at the back aperture of the objective lens. To measure background fluorescence (F_{bk}), each linescan

protocol included a short (~10 μm) background line over the neuropil in the vicinity of the cell (~10 μm; F_{bk}), which was scanned for 45 ms. After that, the cell was scanned for 400 ms before delivering the stimulus ($F_{baseline}$). The resting fluorescence of the cell was calculated as $F_{rest} = F_{baseline} - F_{bk}$ and the peak fluorescence was measured as the maximum value of the fluorescence within a 300 ms window following the stimulus. The ΔF/F value was calculated as: $\Delta F/F = (F_{peak} - F_{baseline}) / F_{rest}$. Raw fluorescence values (F_{rest} and ΔF) and SNR (peak amplitude divided by standard deviation of $F_{baseline}$) are reported only for cells imaged with the same laser intensity (10 mW, ~90% of data). We acquired images of the cells at the start of the recordings (either before or immediately after the cell was patched) and after the withdrawal of the recording pipette. We excluded cells from our analysis if the mean intensity of fluorescence changed >25% from the beginning to the end of the cell-attached recordings. The remaining cells had a mean intensity at the start of the recording of 364 ± 367 AU and 377 ± 355 AU (n = 55) at the end of the recordings. Image z-stacks (2 μm step size) were also taken to allow *post hoc* identification of the recorded cells. ROIs around the somata were drawn in Icy BioImage Analysis software (http://icy.bioimageanalysis.org/, De Chaumont et al., 2012) and mean GCaMP6f intensities were measured in the optimal focus plane. The laser intensity (10 mW) and PMT setting were the same for all images used for quantification. My collaborator, Katalin Szigeti reconstructed the soma of a subset of cells in 3D and calculated their surface and volume as follows: (1) volume: she multiplied the ROI areas measured from each frame with the z-step size; (2) surface: she multiplied the ROI circumference measured from each frame with the z-step size, and added the areas of top and bottom ROIs.

In another set of experiments, cells were filled with a Ca^{2+}-insensitive (20 μM Alexa Fluor 594) and a Ca^{2+}-sensitive fluorophore (300 μM Fluo5F). After 7 to 10 minutes in whole-cell configuration the stabilization of peak amplitude and decay time constant indicated the dye reached an equilibrium. For the measurement of variability of unitary peak amplitudes only data from this time period was used. For determining the linearity I used data from similar time intervals after establishing the whole-cell configuration. Fluorescence changes were quantified as reported previously (Holderith et al., 2012; Éltes et al., 2017). A uniform Gaussian filtering was applied to all fluorescent traces.

4.3.6. Tissue processing for *post hoc* identification of the imaged GCaMP6f expressing cells

After recordings, the slices were fixed in a solution containing 4% PFA, 0.2% picric acid in 0.1 M PB, pH = 7.4, at 4°C overnight.

Image stacks were acquired with an Olympus FV1000 confocal microscope with 20X and 60X (oil-immersion) objectives. The recorded cells were identified based on two-photon image stacks. For quantification of *post hoc* native GCaMP6f intensities I used the same laser and PMT settings. Mean native GCaMP6f intensities were quantified as described above. The background was measured in each slice over five ROIs placed close to each cell, and their mean value was subtracted from the fluorescence values measured over the cells. I also measured the GCaMP6f intensity for 15 cells from ROIs including or excluding the nuclei and found almost perfect correlation between these values ($\rho = 0.96$; Spearman correlation), indicating that both measurements reflect equally well the intensity of GCaMP6f fluorescence.

4.3.7. Immunohistochemistry and quantification of nativeGCaMP6f and anti-GFP intensities

One month after virus injection, together with my collaborator, we deeply anesthetized male mice (n = 3, 55 - 76 days old) with isoflurane and i.p. injection of Ketamine (0.2 ml / 20 g body weight). The mice were transcardially perfused with 0.9% saline (for 1 min) followed by 2% PFA and 0.2% picric acid in 0.1M PB for 16 min. The brain was quickly removed from the skull and postfixed for another hour after which it was placed in PB. Blocks were cut out from the forebrain and 50 μm coronal sections were cut with a vibratome. Then, Katalin Szigeti performed immunoreactions as follows: Sections from one mouse were washed in 0.1M PB and TBS (pH 7.4) containing 0.1% TritonX-100 and blocked in NGS (10%) for 1 h made up in TBS. Sections were then incubated in mouse anti-GFP (1:5000, catalog number 75-132, NeuroMab) IgG diluted in TBS containing 0.3% TritonX-100 and 2% NGS overnight. Sections were then washed and Cy3 conjugated goat anti-mouse IgG2a (1:500, Jackson Laboratories) secondary antibody was applied for 2.5 h at room temperature. Sections were mounted in Vectashield (Vector Laboratories).

Image stacks were acquired with an Olympus FV1000 confocal microscope with 20X (NA = 0.75, Olympus) and 60X (NA = 1.35, oil-immersion, Olympus) objectives. Laser intensity and PMT settings were the same for all cells. Cells located within the top 6 µm of the sections were selected for quantification. The recorded cells were identified based on two-photon image stacks. For quantification of *post hoc* native GCaMP6f intensities we used the same laser and PMT settings as above. Mean native GCaMP6f and anti-GFP intensities were quantified as described above. The background fluorescence was determined over 78 ROIs and its mean value was subtracted from each cell.

4.3.8. Simulations

The simulations were conducted together with my collaborator, Miklós Szoboszlay. To infer actions potentials from Ca^{2+} traces, we used the MLspike software (Deneux et al., 2016), which detects the most likely underlying spike train. The spike matching tolerance window, i.e. the maximal time difference between an inferred and the original AP, within which the AP is registered as 'correctly detected', was set to 60 ms, almost an order of magnitude shorter than that used by Deneux et al. (0.5s) for all simulations. My colleague, Miklós Szoboszlay implemented MLspike and wrote additional code that permitted an easy execution of complex simulations and analysis. First, he fitted *in vitro* recorded fluorescent [Ca^{2+}] transients evoked by either a single AP or bursts consisting of 5 APs at 50 Hz with MLspike. From the burst protocol (n = 37 cells), he first estimated the p_{nonlin} (and '*baseline drift*' parameters (low frequency fluctuations of the baseline fluorescence). The accuracy of the fitting is quantified in error rates (ERs) as the harmonic mean of sensitivity (% of missed spikes, i.e.: that were not detected within the 60 ms time window from the real spike) and precision (% of false detections). The ERs were calculated for p_{nonlin} values ranging from 0 to 2.1 with an increment of 0.1 and *baseline drift* values from 0.001 to 0.101 with an increment of 0.005 for determining those parameters that produce the smallest ERs (see ***Figure 28***). If there were multiple parameter combinations resulting in minimal ER values, the smallest *baseline drift* value was selected with its corresponding maximal p_{nonlin} value.

Miklós Szoboszlay then generated synthetic fluorescent transients with MLspike at three different frequencies (0.1 Hz, 1 Hz, 10 Hz) of Poisson spike trains (n = 10 repetitions

for each cell). The fluorescent transients were generated with 37 cells' experimentally determined amplitude and decay of single AP-evoked unitary fluorescent [Ca^{2+}] transients, their measured noise and the abovementioned p_{nonlin} and *baseline drift* values. For spike inference, we implemented the following four scenarios: 1) all of the parameters were the cells' own (i.e. with which the synthetic fluorescent data were generated); 2) own amplitude, p_{nonlin} and *baseline drift* parameters, average of n = 37 cells' decay; 3) own decay, p_{nonlin} and *baseline drift* parameters and average of n = 37 cells' amplitude; and 4) all four parameters were the averages of the 37 cells.

To test the efficacy of our approach under more realistic conditions, we generated fluorescent Ca^{2+} traces using *in vivo* recorded spike times of hippocampal CA1 PCs (Grosmark, Long and Buzsaki; CRCNS.org, http://dx.doi.org/10.6080/K0862DC5; Grosmark and Buzsáki, 2016). I estimated the peak amplitude of putative unitary [Ca^{2+}] transients with two methods. (1) First, I approximated the percentage of temporally isolated (no spike > 4s before and >1s after a given AP), single AP-evoked [Ca^{2+}] transients. From the spike train of the *in vivo* recorded data, I calculated that two third of the temporally isolated events are single APs, the rests are burst with inter-spike intervals <20 ms. I detected well temporally isolated fluorescent [Ca^{2+}] transients and calculated the '*presumed unitary*' peak amplitudes as the mean of the smallest 66.6 % of the events. (2) In a second procedure, I inferred spiking activity with MLspike using the mean amplitude, decay time constant, p_{nonlin} and *baseline drift* parameters of weakly GCaMP6f expressing cells (n = 20). Then, I selected the temporally isolated (no spike > 4s before and >1s after), potentially single AP-evoked [Ca^{2+}] transients and measured the peak amplitudes of these so called *'detected unitary'* [Ca^{2+}] transients. In few cases, the detected isolated AP followed a missed AP, and a preceding [Ca^{2+}] transient was clearly distinguishable. These transients were omitted when more than 10 isolated [Ca^{2+}] transients were already detected in the cell (n = 4 cells).

Finally, I performed spike inference using the '*putative unitary'* or *'detected unitary'* [Ca^{2+}] transient amplitude of each cell (n = 20) with the mean of the decay, p_{nonlin} and *baseline drift* parameters. All simulations were performed on a desktop computer, running Matlab (version: 2017b) under Windows 10.

4.4. Statistical analysis

All statistical tests and plotting of data were performed using OriginPro. Normality of data was tested using Shapiro - Wilk test. Statistical significance was assessed with: Two-way repeated-measures ANOVA and Bonferroni *post hoc* test (***Figure 14, Figure 15C, D***); Kruskal-Wallis ANOVA test (multiple independent samples; ***Figure 16I***, ***Figure 26B***); Mann-Whitney U test (MW U) (two unpaired groups***; Figure 16I, Figure 17B, Figure 18C***); Spearman correlation for non-normally distributed data (***Figure 19D inset; Figure 21D;*** *Error! Reference source not found.****A,B***; ***Figure 23 F,G,H; Figure 25A, B; Figure 26A,C, D; Figure 27B,C,E,F; Figure 28J; Figure 30B,C;***); Pearson correlation for normally distributed data ***Figure 27H***); Two-Sample Kolmogorov-Smirnov Test (***Figure 21B; Figure 26D; Figure 30A***); Three-Way ANOVA and Bonferroni post hoc test (***Figure 28 E,G,I,K***); Friedman ANOVA, with Paired Sample Wilcoxon Signed Rank *post hoc* test and Bonferroni correction (***Figure 30G***). Data are presented as mean ± SD or median and interquartile range 1 - 3 (IQR). Results were considered significant when $p < 0.05$.

DOI:10.14753/SE.2019.2319

5. RESULTS

5.1. PART I. Target cell type-dependent differences in Ca^{2+} channel function underlie distinct release probabilities at hippocampal glutamatergic terminals

5.1.1. Distinct short-term plasticity of EPSCs in different IN types of the hippocampal CA3 region

I chose CA3 PC local axon collaterals as the subject of my study because they are amenable to presynaptic [Ca^{2+}] measurements (Holderith et al., 2012) and establish synaptic contacts onto both FS/PV^+ INs and mGluR1α^+ INs. First, I characterized the short-term plasticity of EPSCs recorded from PV^+, and mGluR1α^+ INs in the CA3 region of young Wistar rats. For this, I performed whole-cell voltage-clamp recordings from the somata of GABAergic INs located in the stratum oriens or stratum pyramidale with biocytin-containing intracellular solutions and I evoked five EPSCs by extracellular stimulation of PC axons (as illustrated in ***Figure 11***). The intracellular solution also contained picrotoxin (0.6 - 0.8 mM) to block GABAergic responses. These recordings were performed together with my colleague Noémi Holderith.

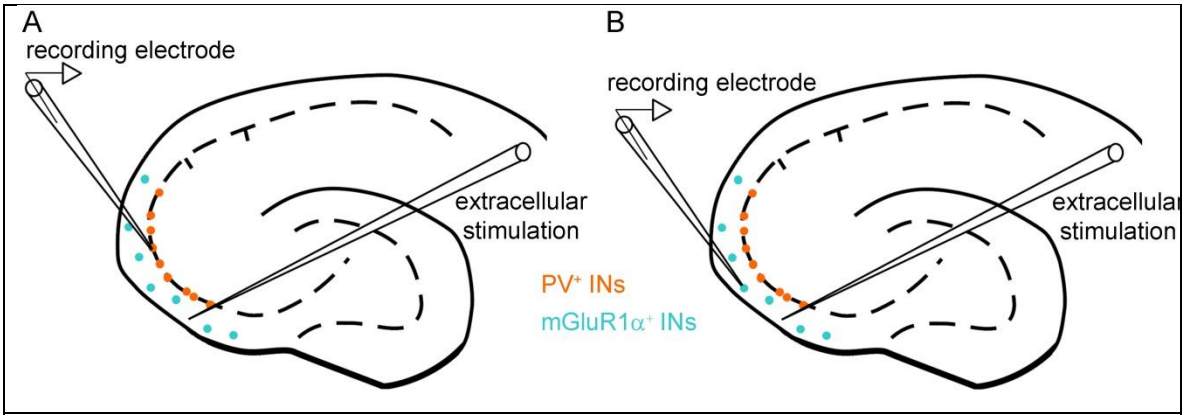

Figure 11. Illustration: Recording synaptic activity of CA3 PC to PV^+ or mGluR1α^+ IN synapses.

(A, B) Recording of EPSCs in PV^+ (A) or mGluR1α^+ (B) INs evoked by extracellular stimulation of local CA3 PC axon collaterals. The stimulating electrode is placed in stratum oriens at least 200 μm away from the recorded cell.

The cells were characterized based on their firing patterns (***Figure 12C, Figure 13C***), *post hoc* determined dendritic and axonal arbors (***Figure 12A, Figure 13A***), and their PV or mGluR1α immunoreactivity (***Figure 12B, Figure 13B***). Even though the FS firing pattern is characteristic to PV^+ cells, I detected PV in only 63% of cells. It is known that during intracellular recordings PV often dilutes to undetectable levels. Because I found no difference in the short-term synaptic properties of FS and PV^+ cells and of FS cells with undetectable levels of PV/ PV^- ($p > 0.05$, MW U test), I pooled these data together.

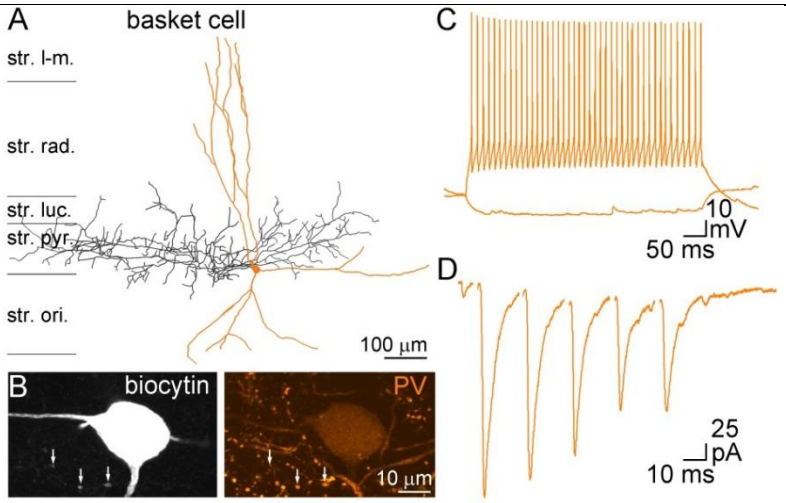

Figure 12. Short-term plasticity of CA3 pyramidal cell synapses contacting PV^+ INs. (A) Neurolucida reconstruction of an *in vitro* recorded basket cell in stratum pyramidale (str. pyr.) of the CA3 region of the hippocampus (soma and dendrites orange, axon black). (B) Confocal image of the biocytin-filled IN (left) showing immunoreactivity for PV (right). Arrows indicate PV immunoreactivity of the biocytin-filled boutons. (C) Membrane potential responses upon depolarizing and hyperpolarizing current injections. The depolarizing suprathreshold response shows FS characteristics. (D) EPSCs (average of 20 traces) evoked by extracellular stimulation in the stratum oriens (str. ori.) display short-term depression. str. luc., stratum lucidum; str. rad., stratum radiatum; str. l-m, stratum lacunosum-moleculare.

EPSCs evoked by a train of stimuli at 40 or 50 Hz in PV^+ INs showed short-term depression ($EPSC^{fifth}/EPSC^{first}$: 0.52 ± 0.19, n=16; ***Figure 12 D, Figure 14***), the extent of which was similar upon stimulation at 20 Hz ($EPSC^{fifth}/EPSC^{first}$: 0.67 ± 0.28, n = 6). In

DOI:10.14753/SE.2019.2319

contrast, EPSCs in mGluR1α$^+$ INs elicited by five stimuli at 50 Hz (EPSC^{fifth}/ EPSC^{first} = 3.02 ± 1.9, n = 31; ***Figure 13D, Figure 14***) or at 20Hz (EPSC^{fifth}/EPSC^{first} : 3.02 ± 2.42, n = 12) showed short-term facilitation.

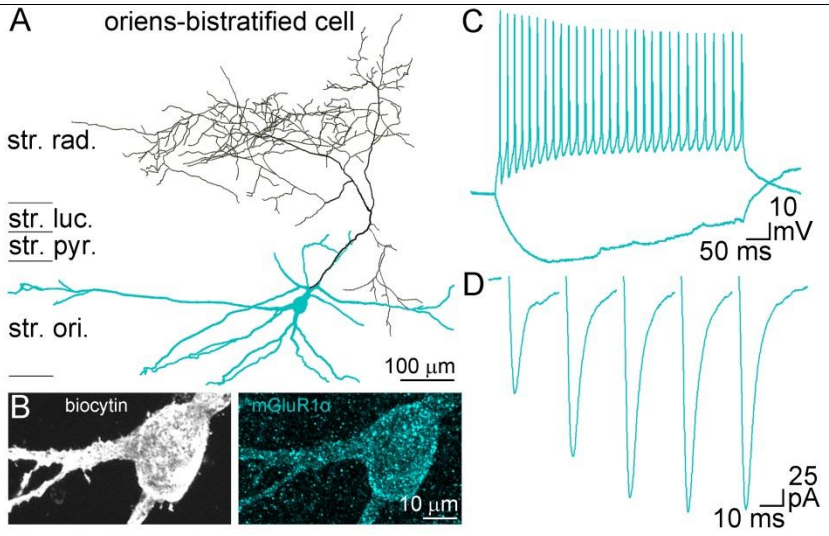

Figure 13. Short-term plasticity of CA3 pyramidal cell synapses contacting mGluR1α$^+$ INs.

(A) Neurolucida reconstruction of an *in vitro* recorded and biocytin-filled oriens-bistratified IN (soma and dendrites blue, axon black) in the str. ori. (B) The biocytin-filled cell (left) is intensely labeled for mGluR1α$^+$ (right). (C) Membrane potential responses to hyperpolarizing and depolarizing current pulses. Firing pattern shows moderate spike frequency adaptation and amplitude accommodation. Note the prominent sag and the slow membrane time constant in response to the hyperpolarizing current step. (D) Extracellular stimulation-evoked EPSCs display short-term facilitation (average of 20 traces). str. luc., stratum lucidum; str. rad., stratum radiatum; str. l-m, stratum lacunosum-moleculare.

The group of cells positive to mGluR1α included several cell-types, such as: oriens-lacunosum moleculare, oriens-oriens, radiatum associated, and basket cells. These cells showed marked heterogeneity based on their dendritic and axonal arbors, firing patterns, and short-term plasticity; with some cells receiving initially facilitating, then depressing, or depressing EPSCs. On average the excitatory inputs to mGluR1α$^+$ cells showed a different short-term plasticity pattern compared with those recorded from PV$^+$ cells (***Figure 14***).

DOI:10.14753/SE.2019.2319

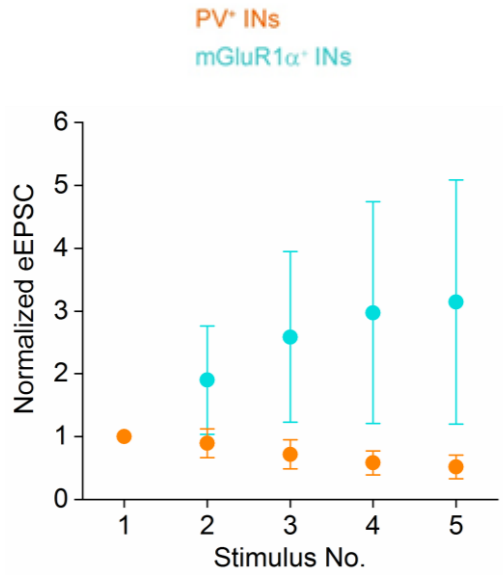

Figure 14. Short-term plasticity of CA3 pyramidal cell synapses contacting PV$^+$ or mGluR1α$^+$ INs.

The short-term plasticity of evoked EPSCs onto PV$^+$ and mGluR1α$^+$ INs differs significantly ($p < 0.01$ for cell type, $p = 0.2$ for stimulus number and $p = 0.01$ for cell type and stimulus number interaction, two-way repeated-measures ANOVA, Bonferroni post hoc test). Data are presented as mean ± SD.

The colocalization experiments of my colleague, Noémi Holderith demonstrated that unlike the CA1 and CA3 regions of dorsal hippocampus (Ferraguti et al., 2004), less than 4% of the mGluR1α$^+$ cells are immunopositive for PV in the ventral CA3 area. She also demonstrated an almost complete colocalization in these cells of mGluR1α with Elfn1/2 (Éltes et al., 2017); a protein of interest because of its critical role in the short-term facilitation of EPSCs onto mGluR1α$^+$ O-LM cells of the CA1 region (Sylwestrak and Ghosh, 2012). Therefore, I next tested the potential role of Elfn1/2 in the diverse short-term plasticity of EPSCs onto mGluR1α$^+$ cells. Elfn1/2 and mGluR1α double-labeled INs showed a robust short-term facilitation, the degree of which was significantly larger than that detected in mGluR1α$^+$, but Elfn1/2$^-$ cells (***Figure 15 C,D***). I did not find any Elfn1/2$^+$ IN that received short-term depressing excitatory input, whereas most of Elfn1/2$^-$ cells received short-term depressing EPSCs (depressing, n = 3; initial slight facilitation followed by depression, n = 1; facilitation, n = 1, ***Figure 15D***). These results reveal a previously unseen diversity in the short-term plasticity of PC-to-mGluR1α$^+$ IN synapses and indicate a potential role of Elfn1/2 in its regulation.

DOI:10.14753/SE.2019.2319

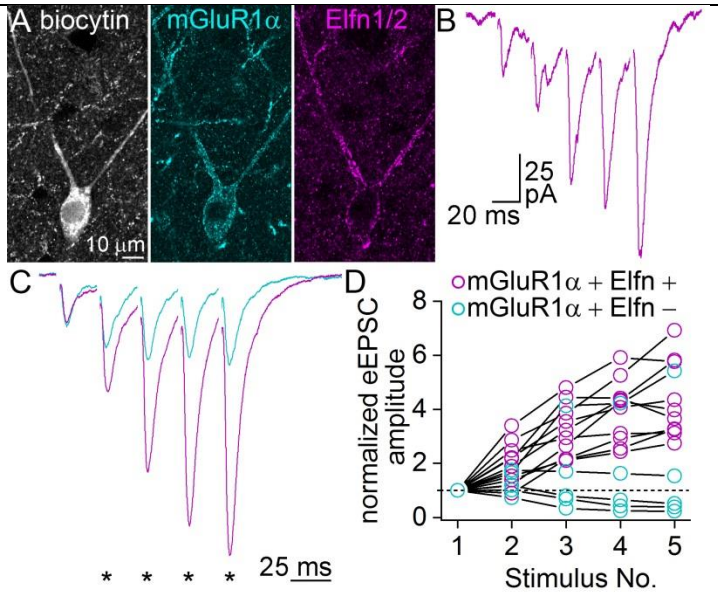

Figure 15. Different short-term plasticity of CA3 pyramidal cell synapses contacting mGluR1α$^+$ and Elfn1/2$^+$ or Elfn1/2$^-$ INs.

(A) A biocytin-filled IN is intensely labeled for mGluR1α and Elfn1/2. (B) Peak amplitude of evoked EPSCs onto the same representative cell. (C -D) Peak amplitudes of evoked EPSCs onto Elfn1/2 double-positive INs are significantly larger ($p < 0.05$ for cell type, $p = 0.31$ for stimulus number and $p = 0.17$ for cell type and stimulus number inter- action, two-way repeated-measures ANOVA, Bonferroni post hoc test) than those recorded from mGluR1α$^+$, but Elfn1/2$^-$ cells. (C, traces are mean of 10 cells for double-positive and mean of 5 cells for Elfn1/2$^-$.)

The demonstrated robust differences in the short-term plasticity of evoked EPSCs in PV$^+$ and mGluR1α$^+$ INs in the CA3 area, are similar to those observed in the CA1 area and the neocortex, offering the use of these molecules in this brain region as markers to label the postsynaptic compartments of functionally distinct presynaptic axon terminals. Elfn1/2 seems to be an ideal molecular marker for postsynaptic INs that receive strongly facilitating inputs, but its *post hoc* visualization requires very mild fixation (see Materials and Methods) that is incompatible with *post hoc* recovery of axonal arbor and electron microscopic (EM) analysis. However, because 90% of mGluR1α$^+$ IN dendrites are also Elfn1/2$^+$ I decided to use mGluR1α as my molecular marker for facilitating synapses.

DOI:10.14753/SE.2019.2319

5.1.2. Target cell type-dependent differences in Ca^{2+} inflow in axon terminals

To provide data that is necessary for estimating the functional Ca^{2+} channel density in the presynaptic AZs of CA3 PCs (Holderith et al., 2012), I measured the Ca^{2+} influx in the PV^{+}- and $mGluR1\alpha^{+}$-dendrite targeting boutons. This approach requires the measurements of $[Ca^{2+}]$ transients in local axon terminals of PCs using two-photon microscopy with an intracellularly applied Ca^{2+}-sensitive dye (300 μM Fluo5F). These recordings were performed together with my colleague Noémi Holderith.

I performed whole-cell voltage-clamp recordings of CA3 PCs and evoked single APs by a depolarizing current pulse. Single AP-evoked $[Ca^{2+}]$ transients showed sizeable variability in their peak amplitudes (coefficient of variation (CV) = 0.37, n = 692 boutons in 30 cells). To examine $[Ca^{2+}]$ specifically in axon terminals with identified postsynaptic target cell types, I fixed the slices after the *in vitro* imaging experiments and then, I visualized the intracellular biocytin and immunolabeled the tissue for mGluR1α and PV for confocal microscopic analysis (***Figure 16***).

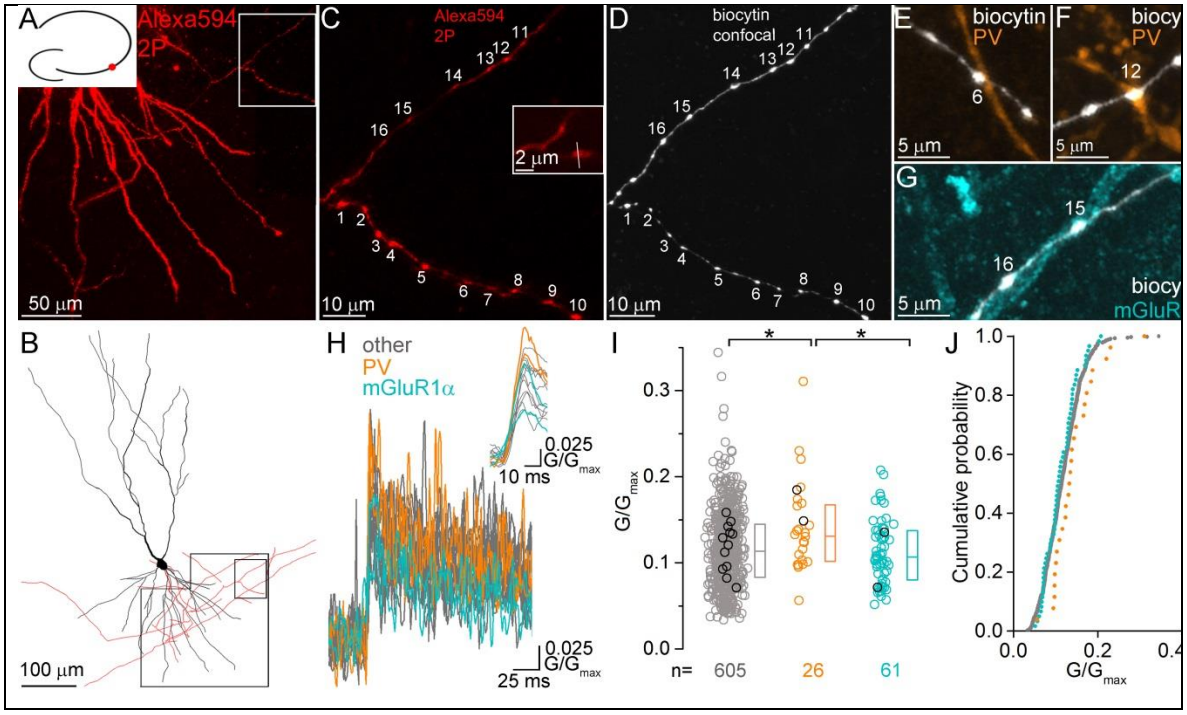

Figure 16. Larger [Ca^{2+}] transients in PV^+ than in mGluR1α$^+$ dendrite-contacting boutons.

(A) Two-photon (2P) image stack of a CA3 PC basal dendritic tree and axonal arbor filled with 20 μM Alexa Fluor 594 (Alexa594, red), 300 μM Fluo5F, and biocytin. Boxed area is shown at higher magnification in C. Diagram at the upper left corner illustrates the position of the cell in the CA3 area. (B) Neurolucida reconstruction of the cell shown in A. Boxed areas correspond to A and C. (C-D) High-magnification two-photon (C) and confocal (D) images of the scanned axon collaterals after fixation and visualization of the biocytin. Numbers indicate the boutons that have been line scanned. Inset in C shows bouton #1 at a higher magnification. The line indicates the position of the line scan. (E-G) Some of the imaged boutons are in contact with PV (E,F, boutons #6 and #12) or mGluR1α (G, boutons #15 and #16) immunolabeled dendrites (white, biocytin; orange, PV; cyan, mGluR1α). (H) Single AP-evoked [Ca^{2+}] transients (n = 16 transients from 16 boutons, each trace is the average of two scans) recorded in the axon terminals shown in C. Orange and cyan traces are transients from PV^+ and mGluR1α$^+$ dendrite-contacting boutons, respectively. Inset shows the same traces after Gaussian filtering on an extended time scale. (I) Peak [Ca^{2+}] transient amplitudes are significantly larger (Kruskal–Wallis test: $p < 0.01$, MW U *post hoc* test, $p < 0.01$ between unidentified and PV; $p < 0.01$ between PV and mGluR1α) in PV^+ (orange) compared to mGluR1α dendrite-contacting (cyan) or all other boutons (gray, n = 605 boutons from 30 cells). Black symbols correspond to individual data points obtained from the cell shown in A-G. (J) Cumulative probability plot of the same peak amplitudes indicates higher probability of a larger transients in PV^+ dendrite-innervating terminals. Data are presented as median and IQR.

In most experiments, I imaged 15 - 30 boutons, of which few had apparently PV^+ or mGluR1α$^+$ dendrites as postsynaptic targets. From the total of 692 imaged boutons, we found 26 and 61 as potential presynaptic elements to PV^+ and mGluR1α$^+$ INs, respectively. My *post hoc* analysis revealed that the peak amplitude of the [Ca^{2+}] transient was 1.25 times larger in PV^+ dendrite-targeting boutons compared with their mGluR1α$^+$ dendrite-targeting counterparts (PV: median: 0.134 G/G_{max}, IQR: 0.105 - 0.168 G/G_{max}, n = 26; mGluR1α:

median: 0.107 G/G_{max}, IQR: 0.081 - 0.138 G/G_{max}, n = 61, unidentified target: median: 0.114 G/G_{max}, IQR: 0.084 - 0.145 G/G_{max}, n = 605; ***Figure 16I, Table 2***).

To minimize potential errors caused by slightly different dye concentrations in distinct PCs, I calculated peak amplitude ratios with two other methods. First, I restricted my analyses to cells that contained both PV^+ and mGluR1α^+ dendrite-targeting boutons and calculated within-cell ratios and found a 1.28 times higher value in boutons targeting PV^+ dendrites (n = 10 cells). Second, I normalized the peak amplitude of the $[Ca^{2+}]$ transients in each PV^+ and mGluR1α^+ dendrite innervating bouton to the mean of peak amplitudes recorded from all boutons of a given cell and again found a 1.21 times larger value in boutons targeting PV^+ dendrites. In a separate set of experiments, I performed $[Ca^{2+}]$ imaging with 100 μM Fluo5F and calculated the above mentioned peak amplitude ratios. The within-cell ratio of peak $[Ca^{2+}]$ in boutons innervating PV^+ or mGluR1α^+ dendrites was 1.32 (n = 11 cells), whereas the $[Ca^{2+}]$ transients in PV or mGluR1α- innervating boutons normalized to the mean $[Ca^{2+}]$ transients were 1.33 (n = 18) and 1.04 (n = 35), respectively, yielding a ratio of 1.27 (***Table 2***).

Table 2. Properties of $[Ca^{2+}]$ transients in PV^+ and mGluR1α^+ dendrite-innervating axon terminals.

* Used for the statistical comparisons.

[a] $[Ca^{2+}]$ transients were normalized to the mean of all measured $[Ca^{2+}]$ transients of the given cell.

	PV^+ dendrite-targeting boutons					mGluR1a$^+$ dendrite-targeting boutons						
	Mean	SD	Median	n	# animal	Mean	SD	Median	n	# animal	Test	p
Peak amplitude of $[Ca^{2+}]$ transient (300 mM Fluo5F) (G/G_{max})	0.14	0.05	0.13	26*	15	0.11	0.04	0.11	61*	23	MW U-test	0.012
Normalized peak amplitude of $[Ca^{2+}]$ transient (300 mM Fluo5F)[a]	1.20	0.41	1.12	26*	15	1.00	0.28	0.98	61*	23	t-test	0.024
Peak amplitude of $[Ca^{2+}]$ transient (100 mM Fluo5F) (G/G_{max})	0.21	0.10	0.22	14*	9	0.17	0.11	0.14	21*	13	MW U-test	0.100
Normalized peak amplitude of $[Ca^{2+}]$ transient (100 mM Fluo5F)[a]	1.33	0.51	1.36	18*	12	1.04	0.25	1.03	35*	18	t-test	0.037

DOI:10.14753/SE.2019.2319

Next, I assessed the contribution of the N/P/Q-type Ca^{2+} channels to the [Ca^{2+}] transients. For this, I applied ω-CTX MVIIC (a selective N- and P/Q-type Ca^{2+} channel blocker) in a concentration (1 μM) that almost completely abolished the evoked EPSCs in both INs in the stratum oriens of the CA3 area (Éltes et al., 2017, demonstrated in a different set of experiments testing the effect of 1 μM ω-CTX MVIIC on evoked EPSCs which were performed by Noémi Holderith). The toxin reduced the peak amplitudes of the presynaptic [Ca^{2+}] transients by 47% (n = 296 boutons in n = 13 cells). The extent of the block was similar in PV-innervating boutons (45 ± 10% ; n = 12) and in mGluR1α- innervating boutons (46 ±18%; n = 19; p > 0.05, MW U test, ***Figure 17***). These results demonstrate that N/P/Q-type Ca^{2+} channels contribute similarly to the [Ca^{2+}] transients in the two bouton populations.

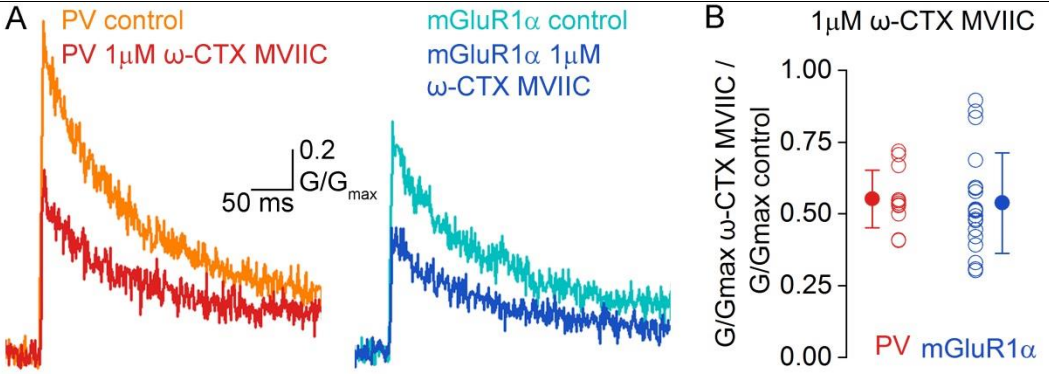

Figure 17. Contribution of N/P/Q type [Ca^{2+}] channels to the [Ca^{2+}] transients.
(A) Mean of single AP-evoked [Ca^{2+}] transients before and after application of 1 μM ω-CTX MVIIC (n = 12 PV -innervating boutons, n = 19 mGluR1α -innervating boutons). (B) [Ca^{2+}] transients are blocked to a similar extent in boutons targeting PV or mGluR1α dendrites (p > 0.05, MW U test). Data are presented as mean ± SD.

A larger [Ca^{2+}] transient might be the consequence of lower Ca^{2+} buffering, a smaller bouton volume, or a larger amount of Ca^{2+} entering the bouton. In my thesis I approached the question of potential differences in buffering, whereas the other questions were tested by my colleague Noémi Holderith (Éltes et al., 2017).

I fitted the decay of the averaged [Ca^{2+}] transients with single exponentials and found very similar time constants (PV: 352 ms, n = 25 boutons; mGluR1α: 413 ms, n = 61 boutons; other: 475 ms, n = 605 boutons, ***Figure 18A***). However, in these recordings I minimized the

DOI:10.14753/SE.2019.2319

scanning time after the AP to avoid photo damage. Therefore, the fit was restricted to 260 ms, during which the [Ca^{2+}] transients did not decay back to baseline (***Figure 18A***). Moreover, the high fluorescent dye concentration (300 µM) used in these experiments might dominate the decay, masking potential differences in the fixed buffer concentration. To circumvent this problem, I recorded [Ca^{2+}] transients with 100 µM Fluo5F and analyzed their decay times (***Figure 18B, C***). The [Ca^{2+}] transients recorded with lower dye concentrations displayed a substantially faster decay (300 µM: 463 ms, n = 691 boutons; 100 µM: 210 ms, n = 439 boutons; fitted to the first 260 ms of the averaged traces). When I compared the decay time constants of [Ca^{2+}] transients in boutons innervating PV^+ or $mGluR1\alpha^+$ dendrites, I found no significant difference (PV: median: 277 ms, IQR: 212 - 403 ms, n = 18; mGluR1α: median: 259 ms, IQR: 207 - 322 ms, n = 35; $p < 0.61$, MW U test; ***Figure 18B, C***), arguing against a robust difference in Ca^{2+} buffering.

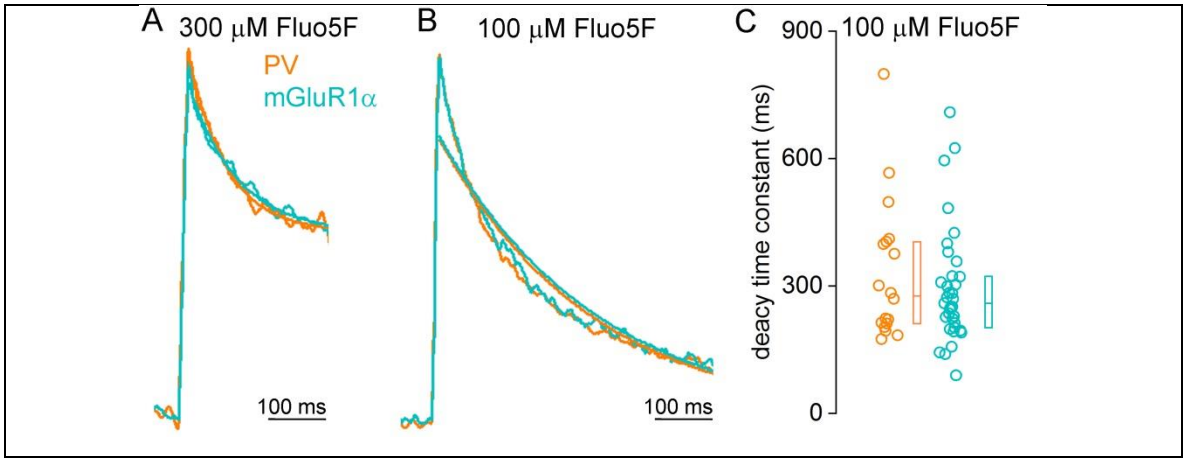

DOI:10.14753/SE.2019.2319

Figure 18. Decay time constant of [Ca^{2+}] transients in innervating PV^+ or mGluR1α^+ dendrites is similar.

(A) Normalized mean [Ca^{2+}] transients recorded with 300 μM Fluo5F. Transients are fitted with a monoexponential (orange, PV^+ dendrite targeting boutons, n = 25; cyan, mGluR1α^+ dendrite targeting boutons, n = 61). (B) Monoexponential fit on [Ca^{2+}] traces recorded with lower dye concentration, 100 μM Fluo5F (orange, PV^+ dendrite targeting boutons, n = 18; cyan, mGluR1α^+ dendrite targeting boutons, n = 35). (C) Decay time constants of [Ca^{2+}] transients are similar in the two bouton populations ($p > 0.05$, MW U test). Traces are Gauss filtered for optimal visualization of the fits. Data are presented as median and IQR.

To test for potential differences in bouton volumes, Noémi Holderith performed 3D EM reconstructions of PV^+ or mGluR1α^+ dendritic segments and their presynaptic axon terminals in the stratum oriens of perfusion fixed tissue, and of a randomly selected subset of our in vitro two-photon imaged boutons. Her experiments revealed no significant difference in the volume of the boutons innervating these IN types, demonstrating that distinct bouton volumes are not the main cause of the observed differences in peak [Ca^{2+}]. She also measured the total AZ areas in the 3D reconstructed boutons and found significantly smaller AZs in PV^+ dendrite-innervating boutons. Her bouton volume and active zone measurements, and our [Ca^{2+}] imaging experiments allowed the calculation of the total Ca^{2+} that enters upon an AP (peak [Ca^{2+}] * volume). Assuming that this Ca^{2+} enters through Ca^{2+} channels located in the AZs, we could calculate the functional Ca^{2+}channel density (i.e. total amount of Ca^{2+} that enters the boutons through a unit AZ area). These two combined functional- structural approaches indicated an 1.7 - 1.9 times larger functional Ca^{2+} channel density for boutons innervating PV^+ INs compared to the mGluR1α^+ dendrite-targeting ones.

5.2. PART II. Improved spike inference accuracy by estimating the peak amplitude of unitary [Ca2+] transients in weakly GCaMP6f expressing hippocampal CA1 pyramidal cells

5.2.1. Variability in the amplitude of GCaMP6f [Ca^{2+}] transients

I obtained sparse expression of GCaMP6f in dorsal hippocampal CA1 PCs by injecting the mixture of highly diluted Cre-recombinase-expressing AAV vectors and concentrated flexed GCaMP6f-containing AAVs. Three weeks after the virus injection, I implanted a chronic imaging window above the dorsal hippocampus to provide optical access for recording neuronal activity in a head-fixed, lightly anaesthetized mouse. The peak amplitude of [Ca^{2+}] transients (0.26 ± 0.3 ΔF/F, median = 0.16 ΔF/F, IQR: 0.07 - 0.36 ΔF/F, n = 311 transients) showed substantial variability (mean CV = 1.07 ± 0.42, n = 13 cells; ***Figure 19A-C***) in my imaged cells, similar to that published previously (Chen et al., 2013). The variability in the peak [Ca^{2+}] transients could reflect different single AP-evoked, unitary [Ca^{2+}] transient among cells, different ratios of single APs and bursts of APs, different numbers of APs within bursts and the different degrees of nonlinearity of the genetically encoded Ca^{2+} indicator.

To address the contribution of these parameters, I recorded single AP-evoked unitary [Ca^{2+}] transients in acute hippocampal slices. Whole-cell patch-clamp recording perturbs the intracellular milieu of the cells and dialyzes soluble proteins, including GCaMP6f; therefore, I decided to record extracellularly-evoked APs in cell-attached configuration and the corresponding [Ca^{2+}] transients with two-photon microscopy in a line-scan mode over the somata. Antidromic APs were evoked by extracellularly stimulating PC axons in stratum oriens/alveus. The mean peak amplitude of [Ca^{2+}] transients evoked by a single AP (0.2 ± 0.2 ΔF/F, median = 0.14, IQR: 0.06 - 0.27, n = 121 cells) was similar to that described earlier (e.g. Chen et al., 2013), with profound cell-to-cell variability (CV = 0.96; ***Figure 19D, E***). The signal to noise ratio was also highly variable (11.4 ± 7.4, median = 10.3, IQR: 5.6 - 15, n = 115), and positively correlated with the unitary [Ca^{2+}] signals ($\rho = 0.88$, $p < 0.01$; Spearman correlation; ***Figure 19D inset***).

DOI:10.14753/SE.2019.2319

The trial-to-trial variability in the amplitude of unitary [Ca^{2+}] transients was assessed by evoking 12 APs at 0.25 Hz. These experiments revealed similar peak amplitudes throughout the train without any significant run-up or run-down (normalized mean of the 12th transient = 1.06 ± 0.16, n = 45 cells) and demonstrated very little within-cell, trial-to-trial variance (CV = 0.13 ± 0.06, median = 0.12, IQR: 0.1 – 0.17, n = 45 cells; ***Figure 19E***).

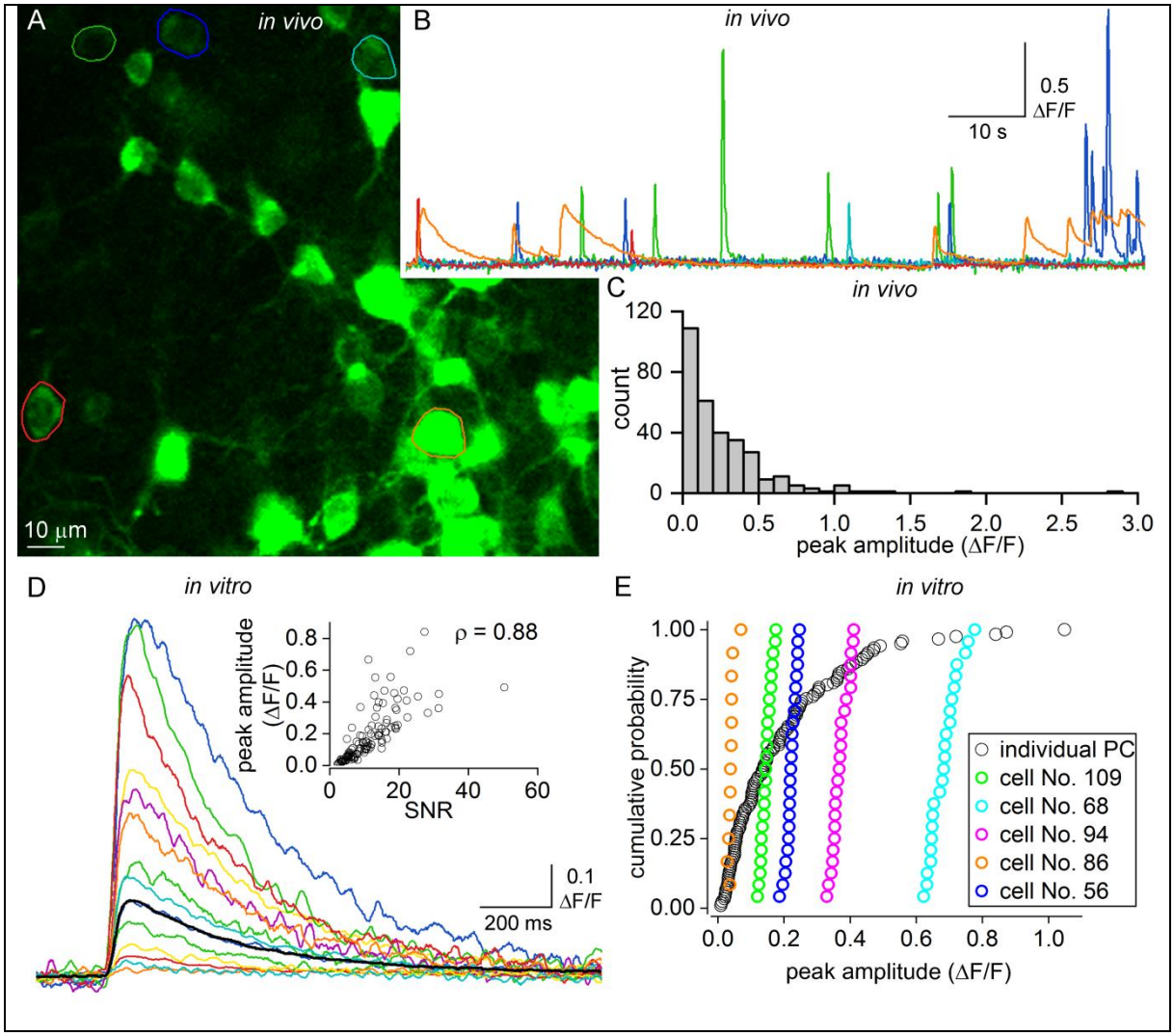

DOI:10.14753/SE.2019.2319

Figure 19. Variability in the amplitude of [Ca^{2+}] transients.

(A) A representative image z-stack (maximum intensity projection of 20 images) of the hippocampal CA1 area in vivo in an anaesthetised, head-fixed micemouse. The ROIs for some of the analysed cells are overlaid. (B) Fluorescence traces recorded from the cells shown in (A). (C) Histogram of peak amplitudes of in vivo recorded [Ca^{2+}] transients (n = 311 transients from 13 GCaMP6f-expressing PCs, 10 minutes long recording). (C) Representative single AP-evoked unitary [Ca^{2+}] transients recorded from the somata of CA1 PCs *in vitro*. Black trace corresponds to average of all recorded PCs (n = 121). Inset: peak amplitude shows significant ($p < 0.01$, Spearman correlation) positive correlation with signal to noise ratio (SNR). (E) Cumulative probability plot of mean unitary [Ca^{2+}] transients (black, n = 121 cells) demonstrates large cell-to-cell variability, with a much smaller trial-to-trial variance of individual cells (5 individual cells color coded, each with multiple trials).

This is large cell to cell variance is not only found for the extracellularly evoked unitary responses, but is also observed for the occasionally occurring (n = 6 cells) spontaneous single AP-evoked responses, which had peak amplitudes and variances very similar to the evoked responses (CV = 0.81, ***Figure 20***).

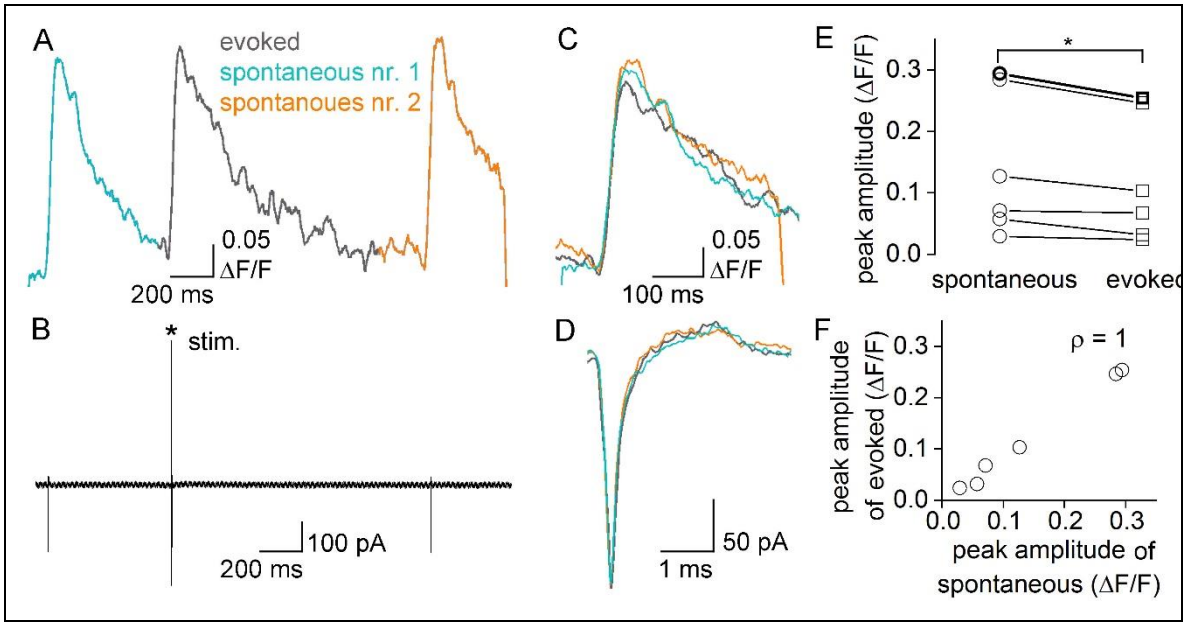

Figure 20. Spontaneous and evoked unitary [Ca2+] transients show similar amplitudes and cell-to-cell variability.
(A-B) A fluorescence trace shows two spontaneous (cyan and orange) and one stimulus-evoked (grey) [Ca2+] transients (A) and the corresponding APs recorded in the cell-attached configuration (B). (C-D) The spontaneous and evoked [Ca2+] transients (C) and APs (D) have similar shapes and amplitudes. (E-F) The amplitude of spontaneous single AP-evoked [Ca2+] transients is on average 27% larger compared to that of the stimulus-evoked [Ca2+] transients (e; n = 6 cells, p = 0.036, Paired Sample Wilcoxon Signed Rank test), but their amplitudes show perfect correlation (f, Spearman correlation).

5.2.2. Variability in the GCaMP6f expression level

Virally expressed proteins, including GCaMP6f are known to demonstrate variable expression levels (Dana et al., 2014). To quantify the variability in the expression level in acute hippocampal slices I first measured GCaMP6f intensities in slices following fixation in 4% PFA-containing fixative using confocal microscopy (***Figure 21A, B***). I argue that by chemically fixing the slices, variability in fluorescence will no longer reflect differences in intracellular [Ca^{2+}], but will purely reflect GCaMP6f expression levels. I found that CA1 PCs show widely differing GCaMP6f intensities (482 ± 542 AU, median = 262 AU, IQR: 109 – 654 AU; CV = 1.12, n = 297 cells). It is known that intensive GCaMP expressing cells with nuclear fluorescence show signs of abnormal physiology and have impaired Ca^{2+} homeostasis (Tian et al., 2009). It is thus likely that these cells do not survive acute hippocampal slicing procedures, resulting in the observed GCaMP6f intensity distribution compared to that observed *in vivo*. To reveal the full range of the GCaMP6f expression, mice -sparsely expressing GCaMP6f in the dorsal hippocampus- were perfusion fixed and the intensity of the labelled cells was quantified using confocal microscopy with identical acquisition settings. The distribution of CA1 PCs according to their GCaMP6f expression showed large variability (IQR: 131 – 979 AU, CV = 1.05, n = 639 cells) with a somewhat higher mean intensity (624 ± 653 AU, median = 345 AU), compared to that obtained from *in*

DOI:10.14753/SE.2019.2319

vitro slices after fixation ($p < 0.01$; Two-Sample Kolmogorov Smirnoff test, ***Figure 21B***), consistent with preferential death of the most intensive cells following slicing.

Another readout of the expression level of GCaMP6f might be determined by measuring the intensity at the isosbestic wavelength of GCaMP6f (~810nm). We therefore measured the fluorescent intensity in acute hippocampal slice at 810 nm excitation wavelength and found that it significantly correlates with the intensity determined *post hoc* after fixation ($\rho = 0.76$, $p < 0.001$, Spearman correlation; ***Figure 21C***). However, we failed to find a significant correlation for cells that weakly express GCaMP6f ($\rho = 0.33$, $p = 0.12$, Spearman correlation, ***Figure 21D***).

To provide unequivocal evidence that the intrinsic fluorescence of GCaMP6f in fixed tissue is indeed proportional to the amount of GCaMP6f protein, Katalin Szigeti immunolabeled the perfusion fixed tissue with an anti-GFP antibody (***Figure 21E***) and examined its relationship with the native GCaMP6f intensity. The almost perfect positive correlation ($n = 87$; $\rho = 0.97$, $p < 0.01$; Spearman correlation; ***Figure 21F***) between the anti-GFP immunoreactivity and intrinsic GCaMP6f fluorescence after fixation indicates that the latter is an excellent correlate of GCaMP6f protein level.

DOI:10.14753/SE.2019.2319

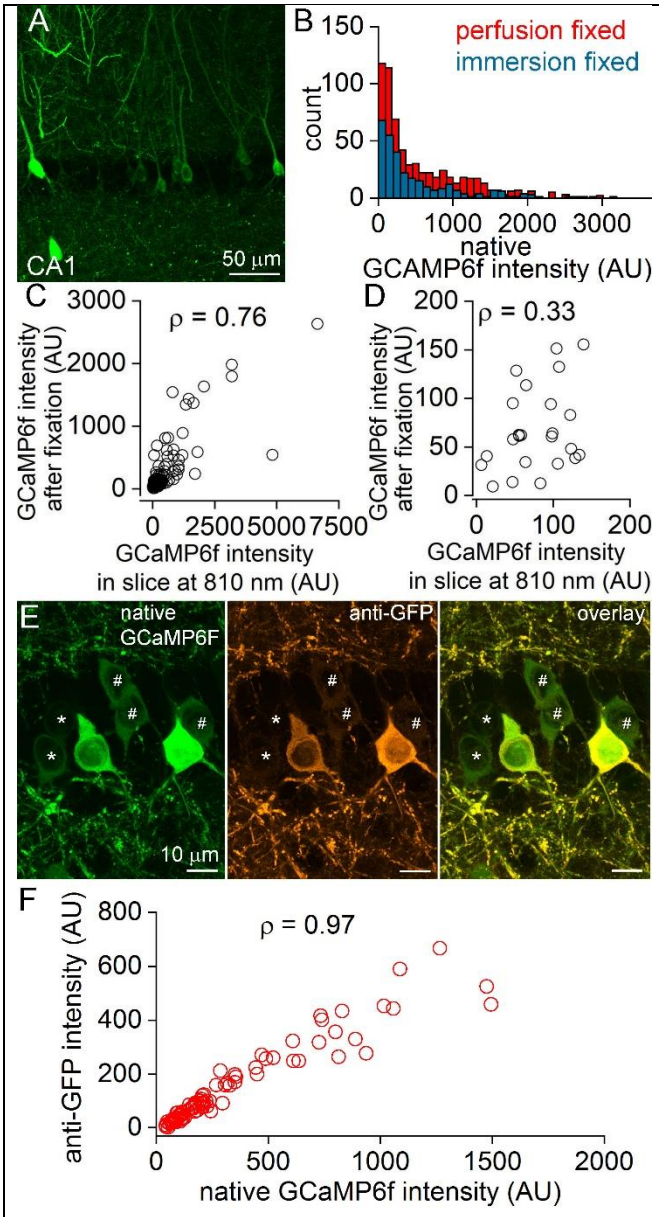

Figure 21. Large variability in the GCaMP6f expression level in CA1 PCs. (A) Maximum intensity projection image showing variability in native GCaMP6f intensity in perfusion fixed tissue. (B) Histograms of native GCaMP6f intensities. (C) GCaMP6f intensity after fixation (measured with confocal microscopy) correlates with GCaMP6f intensity as measured in acute slices using 810 nm excitation light with two-photon microscopy for the whole population ($p < 0.001$, Spearman correlation). (D) For the intensity sub-selected cells (lower 65 percentiles of all cells) no significant correlation is found between these parameters ($p = 0.12$, Spearman correlation). (E) High magnification confocal images of perfusion fixed tissue showing native GCAMP6f expression (green) and their anti-GFP immunoreactivity (orange). * and # indicate weakly and moderately expressing cells, respectively. (F) The intensity of the native GCaMP6f signal and that of the anti-GFP immunosignal shows a significantly positive correlation ($n = 87$, $p < 0.01$, Spearman correlation). AU, arbitrary unit.

5.2.3. Variability of unitary [Ca^{2+}] transients among cells with similar GCaMP6f expression level

Having demonstrated large cell-to-cell variability in the amplitude of unitary [Ca^{2+}] transients and GCaMP6f expression levels, I asked whether these parameters show any correlation. To ensure that even cell-attached recordings do not cause any alterations in the fluorescence of the cells, I measured GCaMP6f intensities before establishing the cell-

attached configuration and after the withdrawal of the pipette in 83 out of 121 PCs in acute slices. I observed that in 28 out of 83 recorded neurons, the fluorescence intensities increased more than 25% during the 10 - 30 minutes cell-attached recordings, resulting in a large increase in the mean intensity of the cells. Thus, I restricted my further analysis to cells that showed changes <25%. The peak amplitudes of unitary [Ca^{2+}] transients (0.20 ± 0.16 ΔF/F, median = 0.15 ΔF/F, IQR: 0.07 - 0.3 ΔF/F, n = 55) and the variability (CV = 0.79) of these subselected cells were very similar to those of the whole population (0.20 ± 0.20 ΔF/F, median = 0.14 ΔF/F, IQR: 0.06 - 0.27 ΔF/F, n = 121 cells, CV = 0.96, ***Table 3***), indicating that the changes in fluorescence during the recordings did not selectively occur in cells showing small or large unitary [Ca^{2+}] transients. This large variance was also apparent among cells recorded from the same slices (CV = 0.64 ± 0.4, n = 10 slices) and from the same animals (CV = 0.65 ± 0.36, n = 18 animals, 2 – 4 cells/animal). At the end of the recordings I acquired Z image stacks of the recorded cells and the surrounding areas to enable their *post hoc* identification after fixation (***Figure 22***).

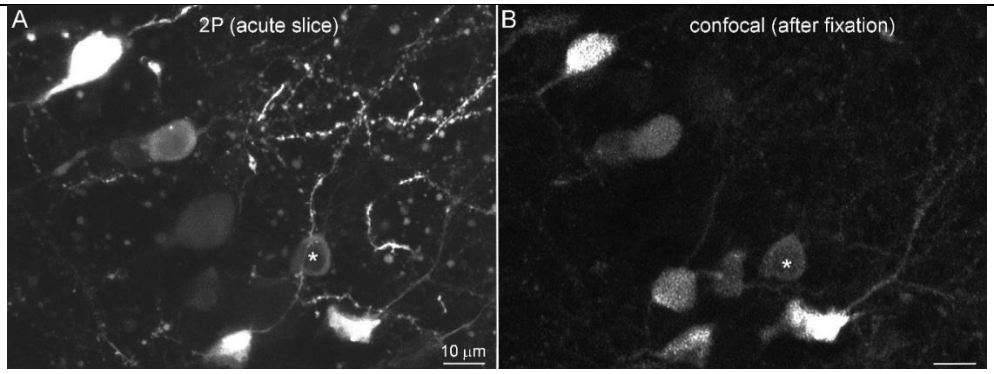

Figure 22. *Post hoc* identification of in vitro, extracellularly recorded cells.
(A, B) Maximum intensity projection images from two-photon (2P; A) and confocal (B) image Z stacks of the recorded cell (*) and surrounding area.

Despite the lack of intracellular labels (e.g. biocytin or fluorescent dyes), I could unequivocally identify 43 of the 55 recorded cells in the fixed sections. Then, I measured their native GCaMP6f intensity levels using confocal microscopy (***Figure 23C***) and observed a substantial variability in their intensity (277 ± 478 AU, median = 151 AU, IQR 66 – 252 AU, CV = 1.73, n = 43 cells; ***Figure 23E***). I found a significant negative correlation between

the peak amplitude of unitary [Ca^{2+}] transients and the GCaMP6f expression level (n = 43, ρ = -0.69, p < 0.01; Spearman correlation, ***Figure 23F***), with highly expressing cells showing very small fluorescence change upon an AP. The relationship seems to follow a power law, where the peak amplitude is proportional to the expression level^{-1}. However, there was a very pronounced variance around the fit at cells with low expression levels. In cells selected for similarly low native GCaMP6f intensities (the lowest 65% of the cells, < 180 AU) the peak amplitudes were somewhat higher (0.26 ± 0.14 ΔF/F, median = 0.22 ΔF/F, IQR: 0.14 - 0.39 ΔF/F), but were still highly variable (CV = 0.56, n = 26).

Table 3. Mean peak amplitudes according to the successive selection criteria.

selection criterias	mean ΔF/F	SD	CV	n
all data	0.199	0.192	0.96	121
intensity change during recording could be assesed (images aquired with same laser intensity)	0.209	0.191	0.91	83
intensity change during recordings < ± 25%	0.202	0.160	0.79	55
identified after fixation	0.191	0.153	0.80	43
GCaMP6f intensity < 180 AU	0.258	0.144	0.56	26
GCaMP6f intensity > 180 AU	0.089	0.102	1.15	17

When the peak amplitude of unitary [Ca^{2+}] transient was plotted against the GCaMP6f expression level for these subselected cells, no significant correlation was found (ρ = -0.22, p = 0.28; Spearman correlation, ***Figure 23G, Table 3***). The amount of GCaMP6f also correlates negatively with the signal to noise ratio (ρ = -0.58, p < 0.01; Spearman correlation, ***Figure 23H***), but it is also highly variable (IQR: 10.5 - 19.3, CV = 0.6, n = 25) for cells with low intensities.

DOI:10.14753/SE.2019.2319

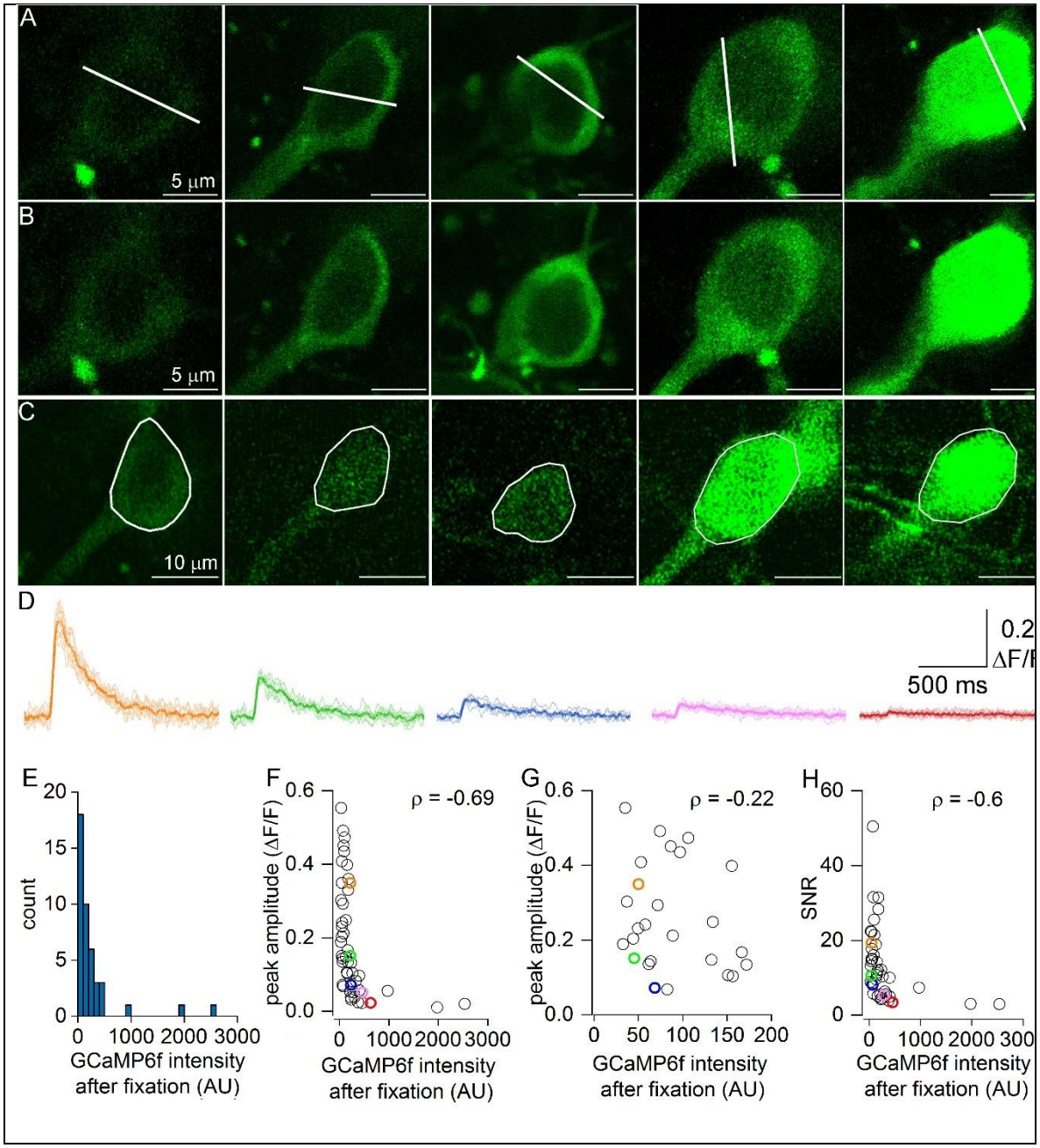

Figure 23. Single AP-evoked [Ca^{2+}] fluorescence transients show large variability among cells with similar GCaMP6f expression level.

(A) Two-photon (2P) images of CA1 PCs before cell-attached recordings (white lines: scanning lines). (B) 2P images of the same cells after recording pipette was withdrawn at the end of the recordings. Note the lack of detectable changes in the native GCaMP6f intensity in these cells. (C) Confocal images of the same cells following immersion fixation **(**outline of ROIs in white; see the *post hoc* identification of the third cell on *Figure 22*) (D) Single AP-evoked unitary [Ca^{2+}] transients in the same 6 cells as shown above (individual transients: semi-transparent, mean: bold) show large variability in amplitude. (E) Histogram of native GCaMP6f intensities of PCs for which the intensity between the start of the recording and withdrawal of the pipette did not change more than 25% (n = 43). (F) The amplitude of unitary [Ca^{2+}] transients correlate negatively with the native GCaMP6f intensity of the cells ($p < 0.01$, Spearman correlation; colored symbols represent the 6 cells shown in A-D). (G) Single AP-evoked [Ca^{2+}] fluorescence signals show large variability among cells with similar intensities (same data as in F, but sub-selected for cells with intensities <180 AU; $p = 0.28$, Spearman correlation). (H) Native GCaMP6f intensity levels correlate negatively with signal to noise ratio of unitary [Ca^{2+}] transients, but show large variability among cells with similar intensities ($p < 0.01$, Spearman correlation).

Non-biological sources of variance could contribute to the observed large variability in the peak amplitude of unitary [Ca^{2+}] transients. The background fluorescence (F_{bk}) varies within the slices and because its exact value influences our estimate of $\Delta F/F$, we estimated its contribution to the total variance of unitary [Ca^{2+}] transients. In a subset of slices, we recorded 2 cells each having its 'own' background line (i.e.: scanned quasi simultaneously with the recorded cell). We calculated the $\Delta F/F$ for each cell with its 'own' F_{bk} and also with the other cell's F_{bk} and calculated the variance in $\Delta F/F$. The mean CV was 0.17, which accounts for ~10% of the total variance (CV = 0.56). Furthermore, the positioning of our scanning line over the cell body can result in different nucleus/cytosol ratios, which could be another biologically-irrelevant source of variance. We, therefore, divided the scanned line over the cells into two halves, having different cytoplasm/nuclei ratios and intensities and calculated $\Delta F/F$. This analysis revealed a very tight, significant correlation ($\rho = 0.94$, $p <$

0.001, Spearman correlation) between the ΔF/F values of the two halves, but some variance was apparent (CV = 0.13 ± 0.1, n = 20 cells). We acknowledge that this is again a biologically irrelevant source of error, but it is responsible only for 5.3% of the total variance in the peak amplitude of unitary [Ca^{2+}] transients (CV = 0.56). Out-of-focus fluorescence light has little if any contribution to the recorded fluorescent transient in sparse labelling conditions. We tested such contribution by two methods: First, we argue that if a labelled process passed below or above our imaged cell and its activity contributed to the fluorescence signal, then the chance that it contributes equally to both the 'left' and 'right' halves is very small. Thus, we divided our line scans into two halves and analysed them separately and we found a coefficient of variation of only 0.13 ± 0.1 (n = 20 cells). In addition to this analysis, we performed the experiments requested by the reviewer. We measured unitary peak amplitudes in three different focal planes (middle of the cell and 3-4 μm above or below this plane) over cell bodies of low GCaMP6f expressing cells and we calculated the coefficient of variations in the mean fluorescent unitary response amplitudes between the three focal planes. The mean amplitudes showed very little dependencies on the focal planes, resulting in a CV of 0.10 ± 0.07 (n = 7 cells, ***Figure 24***). Finally, we also tested how the variance in the peak amplitude of unitary [Ca^{2+}] transients depended on the time between the virus injection and the recordings (i.e. expression time). For this, we calculated the variance in the peak amplitudes measured from the cells recorded in the same slice, or in the same animals (same expression time). We found similarly large variance both within cells from the same slices (mean CV = 0.64 ± 0.4, n = 10 slices) or from cells from different slices but the same animal (mean CV = 0.65 ± 0.36, n = 18 animals, 2 – 4 cells/animal). The variance in the unitary peak amplitude within cells recorded from the same animal (i.e.: same expression time) was large at any given expression time and showed no correlation with the expression time (ρ= 0.25, p = 0.32; n = 18 animals, Spearman correlation).

DOI:10.14753/SE.2019.2319

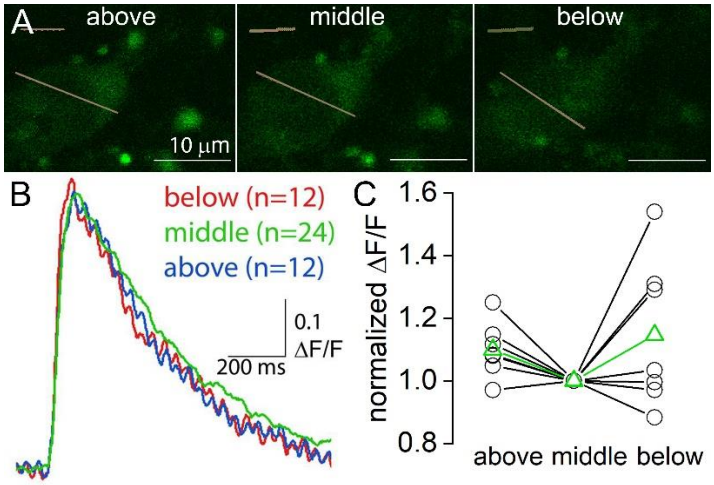

Figure 24. Negligible contribution of out of focus fluorescence to the peak amplitude of unitary responses.

(A) Images of the same weakly GCaMP6f expressing cell in three different focal planes separated by 3-4 µm. (B) Averaged unitary fluorescent transients recorded in the three focal planes shown in (A). (C) The peak amplitudes recorded in the different focal planes show little variability (CV = 0.10, n =7 cells; open circles: individual cells; green triangles: mean).

Next, I analysed the relationship between the decay time constants of the unitary [Ca^{2+}] transients and the GCaMP6f expression level and found a significant positive correlation for the whole population ($\rho = 0.6$, $p < 0.01$; n = 41, Spearman correlation, ***Figure 25A***), and also for the cells subselected based on their GCaMP6f intensity ($\rho = 0.51$, $p < 0.01$; n = 26, Spearman correlation, ***Figure 25B***). When analysing the relationship of unitary peak amplitudes and decay time constants, we found that cells with smaller unitary peak amplitudes (and higher GCaMP6f intensity) displayed mostly longer decay times, resulting in a significant correlation between them ($\rho = -0.27$, $p = 0.048$; n = 53, Spearman correlation, ***Figure 25C, D***); whereas for the GCaMP6f intensity subselected group of cells (intensity < 180 AU) there was no significant correlation between these parameters ($\rho = -0.001$, $p = 0.99$; n = 26, Spearman correlation, ***Figure 25C, E***).

DOI:10.14753/SE.2019.2319

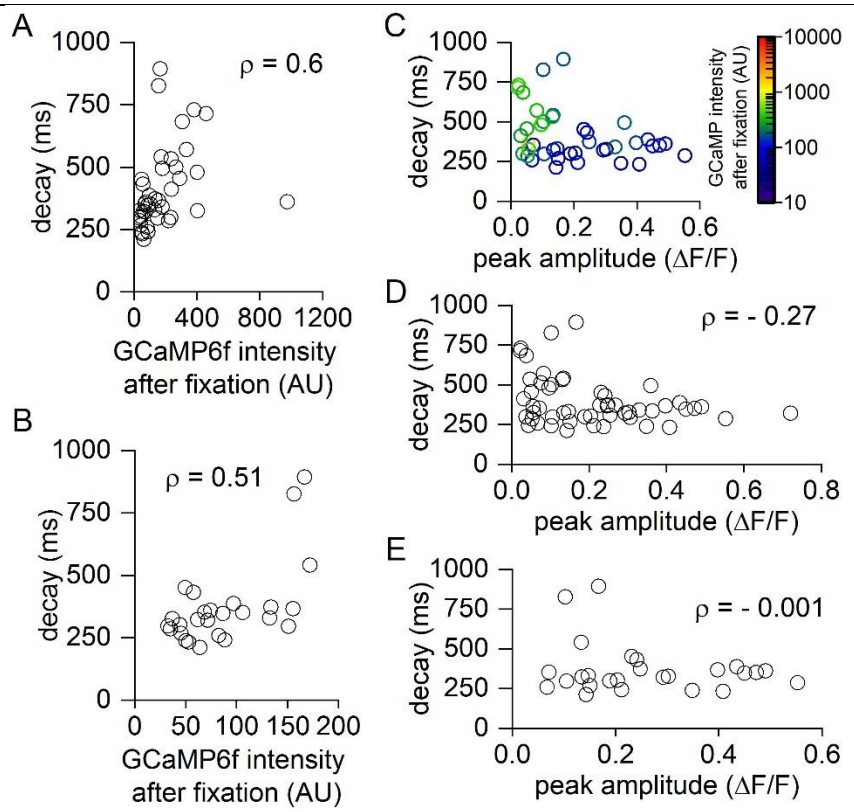

Figure 25. Correlation of the decay time constant of unitary [Ca^{2+}] transients with the GCaMP6f expression level.

(A, B) The decay time constant of single-AP evoked [Ca^{2+}] transients correlates positively with the GCaMP6f intensity of the recorded PCs (n = 41; p < 0.01, Spearman correlation) for the whole population (A) and for the sub-selected cells (B, same data as in A, but sub-selected for cells with intensities <180 AU, corresponding to the bottom 65% of the cells; n = 26; p = 0.008, Spearman correlation). (C) Heatmap plot showing the relationship between decay time constants, the peak amplitudes of unitary [Ca^{2+}] transients and GCaMP6f expression level of the recorded cells. (D) The decay time constants correlate negatively with the peak amplitudes of the unitary responses (ρ = -0.27, p = 0.048; n = 53, Spearman correlation) when all cells are examined. (E) However, when only the weakly GCaMP6f expressing cells are subselected (< 180 AU), there is no significant correlation between these parameters (ρ = -0.001, p = 0.99; n = 26, Spearman correlation).

Variability in the amplitude of unitary [Ca^{2+}] transients reported by GCaMP6f can be the consequence of different amounts of [Ca^{2+}] entering the soma, different somatic surface

to volume ratios or different [Ca^{2+}] buffering. Because the amount of [Ca^{2+}] entering through VGCC during an AP is strongly dependent on the AP waveform (Sabatini and Regehr, 1999; Geiger and Jonas, 2000), I measured AP width (full width at half-maximal amplitude) as recorded in the cell-attached configuration. The AP width does not correlate significantly with the peak amplitude of unitary [Ca^{2+}] transients ($\rho = 0.20$, $p = 0.17$; Spearman correlation, ***Figure 26A***). To assess the effect of potential differences in endogenous buffers such as calbindin, which is expressed in superficial PCs (Baimbridge et al., 1991), I grouped the recorded cells based on their somatic location in the PC layer as deep, middle and superficial cells. I found no significant difference in the peak amplitude of unitary [Ca^{2+}] transients among the three groups (superficial: 0.19 ± 0.15 $\Delta F/F$, $n = 20$; middle: 0.23 ± 0.14 $\Delta F/F$, $n = 18$; deep: 0.14 ± 0.15 $\Delta F/F$, $n = 12$; $p = 0.13$, Kruskal-Wallis ANOVA test with multiple independent samples; ***Figure 26B***). Next, I fitted the decay of averaged [Ca^{2+}] transients with single exponentials and found very similar decay time constants within these subgroups (superficial: 419 ± 154 ms, $n = 19$; middle: 376 ± 127 ms, $n = 18$; deep: 400 ± 210 ms, $n = 11$; $p = 0.35$, Kruskal-Wallis ANOVA test with multiple independent samples), arguing against considerable differences in endogenous Ca^{2+} buffering. To test for potential differences due to different surface to volume ratios, Katalin Szigeti reconstructed the soma of a subset of the recorded PCs in 3D from the two-photon Z image stacks and calculated their surface to volume ratios. The peak amplitude of the unitary [Ca^{2+}] transients of the subselected cells (0.20 ± 0.16 $\Delta F/F$, median = 0.15 $\Delta F/F$, IQR: 0.06 – 0.35 $\Delta F/F$, CV = 0.8, $n = 21$) did not correlate with the surface to volume ratio ($\rho = 0.07$, $p > 0.05$; Spearman correlation, ***Figure 26C***). Differences in resting [Ca^{2+}] could also be an important factor in determining cell-to-cell variability in the peak unitary [Ca^{2+}] transients. To obtain a measure that should reflect the resting [Ca^{2+}] I normalized the resting fluorescence (F_{rest}) of each cell to its native GCaMP6 fluorescence intensity after fixation. The lack of correlation between this measure and the amplitude of its unitary [Ca^{2+}] transients ($\rho = -0.25$, $p = 0.12$, ***Figure 26C***) indicates that the large variance in unitary [Ca^{2+}] transient amplitudes is primarily not the consequence of the variability in resting [Ca^{2+}].

Finally, I tested cell-to-cell variability in the amplitude of unitary [Ca^{2+}] transients in CA1 PCs using a synthetic Ca^{2+} dye, which is known to report physiologically relevant [Ca^{2+}]

linearly ***Figure 26E***. I filled CA1 PCs for 10 minutes with 300 μM Fluo5F and recorded single AP-evoked [Ca^{2+}] transients in the whole-cell configuration. I found substantially smaller variability in the peak amplitude (0.02 ± 0.006 G/G_{max}, median = 0.02 G/G_{max}, IQR: 0.019 - 0.023 G/G_{max}, n = 23) with a CV of only 0.27. The mean-normalized distribution of unitary [Ca^{2+}] signals reported with Fluo5F was significantly narrower than that reported by GCaMP6f (p = 0.014, Two-Sample Kolmogorov Smirnoff test, ***Figure 26F***), suggesting that the variability in the amplitude of GCaMP6f [Ca^{2+}] transients is not the consequence of a biological variability in peak [Ca^{2+}].

DOI:10.14753/SE.2019.2319

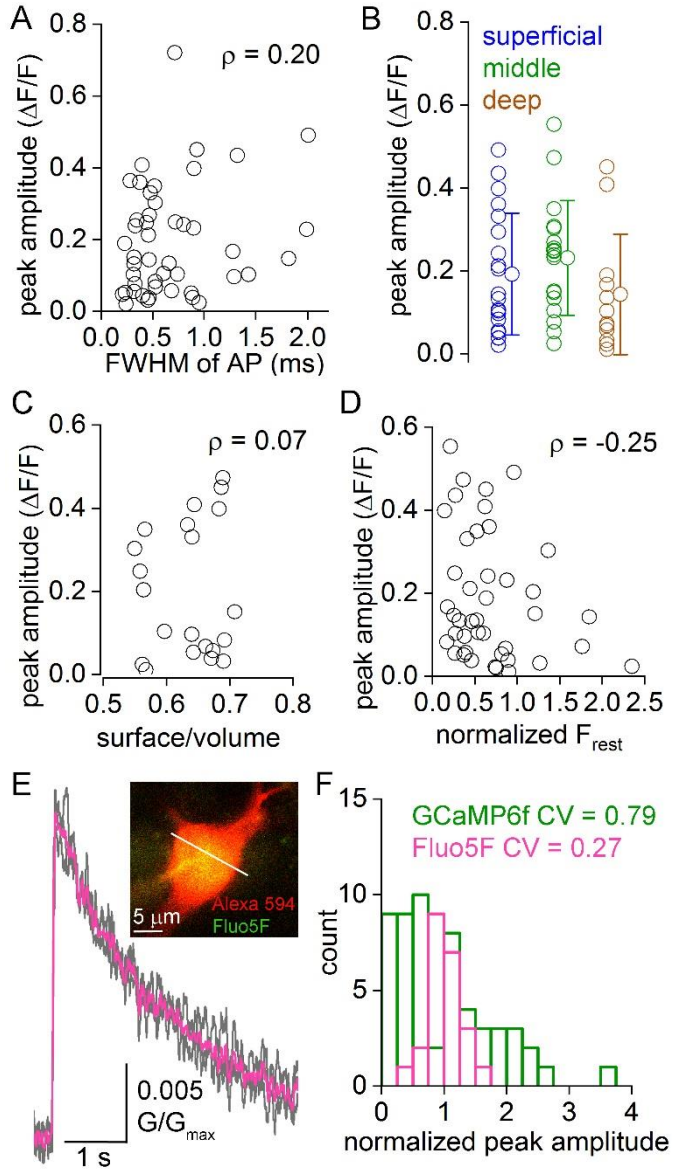

Figure 26. The amplitude of unitary GCaMP6f [Ca^{2+}] fluorescent transients does not correlate with the AP width, soma location in the PC layer or surface to volume ratio. (A) Peak amplitude of unitary [Ca^{2+}] transients do not correlate with AP width recorded in cell-attached configuration (p = 0.17, Spearman correlation; n = 46 cells). (B) Unitary [Ca^{2+}] transients are not significantly different among cells situated in superficial, middle or deep part of the stratum pyramidale (p = 0.13, Kruskal Wallis test). (C) Surface to volume ratio does not correlate with the amplitude of unitary [Ca^{2+}] transients (p = 0.78, Spearman correlation; n = 21 cells). (D) Peak amplitude of unitary [Ca^{2+}] transients does not correlate with the GCaMP6f intensity-normalized F_{rest} (p = 0.12, Spearman correlation). (E) Representative [Ca^{2+}] transients (grey: three individual traces; pink: averaged trace) recorded with 300 µM Fluo5F. Inset shows the scanning line over the PC somata. (F) The distribution of single AP-evoked GCaMP6f [Ca^{2+}] transients (normalized to mean) is wider (CV = 0.79, n = 55) and significantly different (p = 0.014, two-sample Kolmogorov-Smirnoff test), compared to that of unitary [Ca^{2+}] transients measured with Fluo5F (CV = 0.27, n = 23 cells).

5.2.4. Supralinear temporal summation of GCaMP6f [Ca^{2+}] transients

To examine the relationship between GCaMP6f expression levels and the temporal summation of fluorescent [Ca^{2+}] transients, I evoked trains of APs at different frequencies.

[Ca^{2+}] transients showed substantial temporal summation already at 10 Hz and the summation was even more pronounced at 50 Hz (***Figure 27***). I calculated a linearity index by dividing the peak of [Ca^{2+}] transients evoked by the short trains with the respective mathematical sum of their unitary events. The summation of GCaMP6f [Ca^{2+}] transients was was use-dependent (***Figure 27G***) and supralinear at every tested frequency and showed a slight frequency dependence (linearity index: 5AP at 10 Hz: 1.67 ± 0.54, median = 1.54, IQR: 1.31 – 1.94, n = 34; 3AP at 50 Hz: 1.70 ± 0.51, median = 1.57, IQR: 1.42 – 2.02, n = 26; 5AP at 50 Hz: 1.92 ± 0.63, median = 1.89, IQR: 1.48 – 2.27, n = 40; 3AP at 100 Hz: 1.83 ± 0.66, median = 1.82, IQR: 1.23 – 2.26, n = 18). In contrast, the summation of [Ca^{2+}] transients measured with Fluo5F was quasi linear (linearity index: 5AP at 10 Hz: 0.93 ± 0.07, median = 0.95, IQR: 0.9 - 0.96, n = 10), indicating that the supralinear summation of GCaMP6f fluorescent transients is not the consequence of an increased Ca^{2+} influx during the AP trains. The linearity of 5 AP evoked GCaMP6f [Ca^{2+}] transients at 10 Hz did not show significant correlation either with the unitary [Ca^{2+}] transient amplitude ($\rho = 0.14$, $p = 0.4$; Spearman correlation, ***Figure 27B***), or with GCaMP6f expression level ($\rho = -0.33$, $p = 0.09$; Spearman correlation, ***Figure 27C***). The correlation between the linearity of [Ca^{2+}] transients evoked by 5APs at 50 Hz and the peak amplitude of unitary [Ca^{2+}] transients was also not significant ($\rho = 0.3$, $p = 0.06$; Spearman correlation, ***Figure 27E***), but the correlation between the linearity at 50 Hz and the GCaMP6f expression level reached significance ($\rho = -0.46$, $p = 0.006$; Spearman correlation, ***Figure 27F***). The tight correlation between the linearity index for 3APs and 5APs at 50Hz indicates similar summation for a lower number of APs ($r^2 = 0.86$, Pearson correlation; ***Figure 27H***).

DOI:10.14753/SE.2019.2319

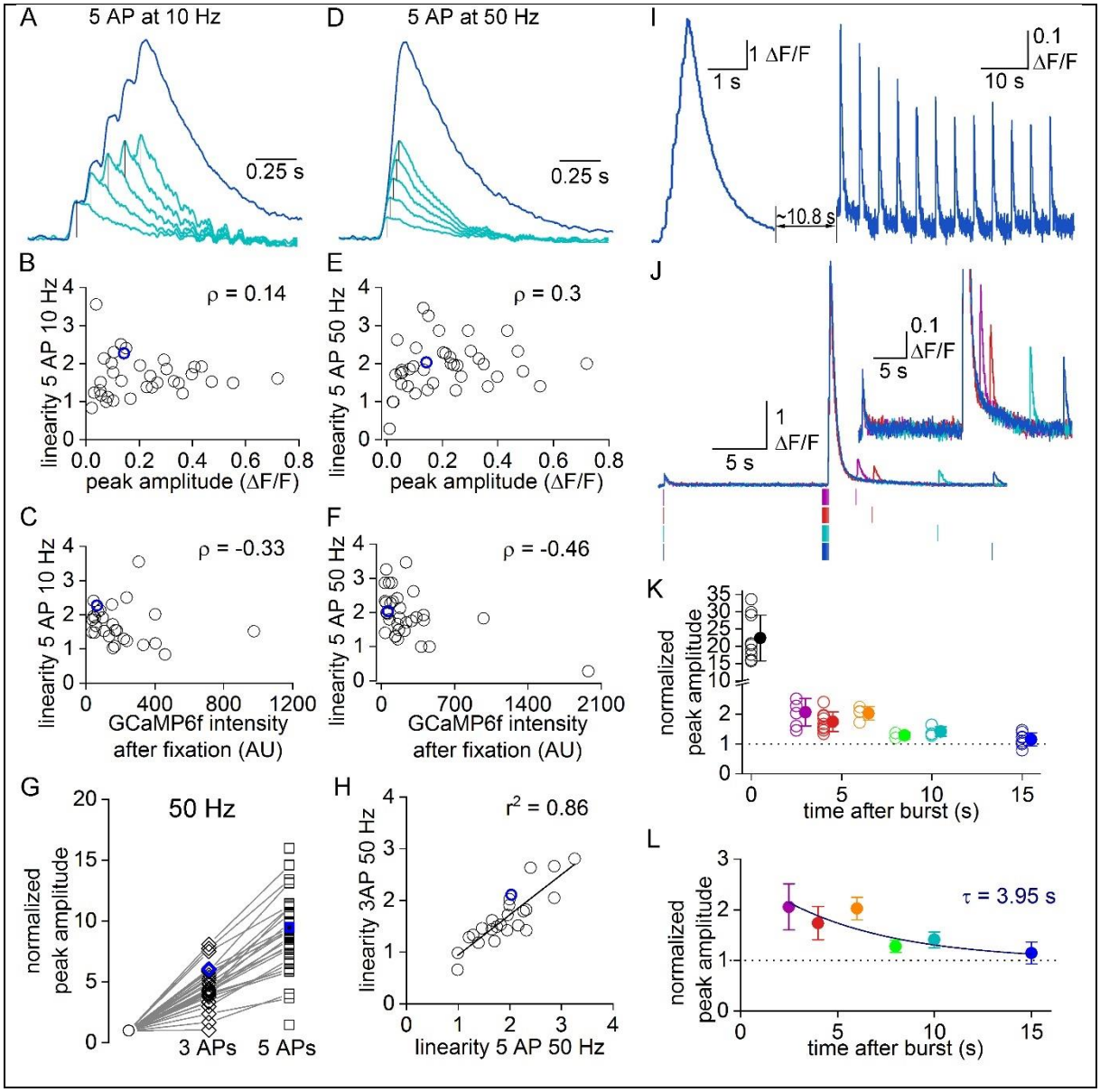

Figure 27. Nonlinearity of GCaMP6f fluorescence signals.

(A, D) Examples of [Ca^{2+}] transients normalized to their unitary peak amplitude evoked by 5 APs at 10 or 50 Hz (blue) and the mathematical sum of its corresponding five, spike time-adjusted, unitary [Ca^{2+}] transients (cyan). (B, C) Fluorescent signals evoked by 5 APs at 10 Hz are supralinear (mean linearity = 1.67 ± 0.54, n = 34). The linearity index does not correlate with either the peak amplitude of unitary [Ca^{2+}] transients ($p = 0.4$; Spearman correlation) or with their native GCaMP6f expression level ($p = 0.09$; Spearman correlation). (E, F) [Ca^{2+}] transients evoked by 5 APs at 50 Hz sum supralinearly (mean linearity = 1.92 ± 0.63, n = 40). The linearity index does not correlate with the peak amplitude of unitary [Ca^{2+}] signals (E, $p = 0.06$, Spearman correlation), but shows a negative correlation with the expression of GCaMP6f (F, $p = 0.006$, Spearman correlation). (G) Normalized peak amplitudes of 3 or 5 AP-evoked [Ca^{2+}] transients are highly variable and show different degrees of summation. (H) The linearity index for 3 and 5 APs at 50 Hz shows a significant positive correlation ($r^2 = 0.86$, $p < 0.001$, Pearson correlation). (I) A large [Ca^{2+}] transient is followed after 10.8 s by 12 APs evoked at 0.25 Hz. Note the gradual decrease of the unitary [Ca^{2+}] signal during the train. (J) Example of several [Ca^{2+}] transients evoked by burst recovery protocols (magenta, 2.5 s; red, 4 s; cyan,10 s; blue, 15 s after a 10 AP at 50 Hz burst). Bottom: lines illustrate the timing of the recovery stimuli for the different protocols. Inset: Same traces zoomed in and compressed in time for better visualization of the transients evoked by the recovery pulses. (K) The increase in peak amplitude of unitary [Ca^{2+}] transients after a burst of 10 APs at 50 Hz persists for several seconds (open circles: mean of individual cells, closed circles: average ± SD). Data are normalized to unitary [Ca^{2+}] transients measured before the burst. (L) Mono-exponential fit ($\tau = 3.95$ s) to the normalized unitary [Ca^{2+}] transients evoked by the recovery pulses (color code same as above).

Interestingly, I observed a dramatic increase in the peak amplitude of the unitary [Ca^{2+}] transients, when they followed high frequency bursts by several seconds (***Figure 27G***). To quantitatively describe this phenomenon, I applied a burst recovery protocol consisting of a 10 AP 50 Hz burst and single recovery pulses at different time points (2.5, 4, 6, 8, 10 or 15 s; ***Figure 27J***). I normalized the amplitude of [Ca^{2+}] transients to the amplitude of a unitary [Ca^{2+}] transient evoked >8 seconds before the burst. [Ca^{2+}] transients evoked by

10 AP at 50 Hz were supralinear (linearity index: 2.54 ± 0.94, median = 2.24, IQR: 1.98 – 3.14, n = 8 cells). 2.5 s after the burst the peak amplitude of the unitary [Ca^{2+}] transient was more than twice (2.06 ± 0.46, median = 2.14, IQR: 1.7 - 2.45, n = 6 cells) that of the control transient and returned to its initial value >10 second later (***Figure 27K, L***). Fitting a monoexponential to the normalized recovery of [Ca^{2+}] transients yielded a time constant of 3.95 s (***Figure 27L***). In contrast, when the same protocol was applied to cells which did not express GCaMP6f and in which [Ca^{2+}] transients were recorded using Fluo5F, the unitary peak amplitude did not increase after burst (4s after burst: 0.84 ± 0.09, median = 0.87, IQR: 0.77 - 0.92, n = 9; normalized to the unitary transient before the burst), indicating that the aforementioned phenomenon are likely due to the nonlinear nature of GCaMP6f and not the short-term facilitation of the Ca^{2+} flux.

Because the supralinear enhancement of peak amplitudes of unitary [Ca^{2+}] transients can be a potential source for the observed large cell-to-cell variance of the unitary [Ca^{2+}] transients of GCaMP6f expressing cells, I subselected cells with traces where the single AP-evoked transients were not preceded by higher frequency events by >10 s. The resulting mean unitary [Ca^{2+}] transient displayed similarly large cell-to-cell variance (CV = 0.95, n = 35). The large variance (CV = 0.73) was also present among cells with low GCaMP6f expression levels (<180 AU, n = 15).

5.2.5. Cell-to-cell variability of the peak amplitude of unitary [Ca^{2+}] transients underlies spike inference error rate

To infer APs from fluorescent [Ca^{2+}] transients, we adopted the method (MLspike) of Deneux et al. (Deneux et al., 2016) with my collaborator Miklós Szoboszlay. We set the tolerance window of spike matching to 60 ms (i.e. an inferred spike should be within a 60 ms time window of an original to be registered as ‘correctly detected’), a value almost an order of magnitude smaller than that used by Deneux et al. (500 ms). MLspike estimates the most likely spike trains underlying the fluorescent transients by using a model that includes *baseline drift* (low frequency, large amplitude baseline fluctuations, see ***Figure 9***), nonlinear feature of the Ca^{2+} sensor (p_{nonlin}; saturation γ, Hill exponent n or polynomial coefficient), the peak amplitude and the decay of the unitary [Ca^{2+}] transients. The accuracy of the fitting is

quantified in error rates (ERs) as the harmonic mean of sensitivity (% of missed spikes, i.e.: that were not detected within the 60 ms time window from the real spike) and precision (% of false detections). First, my collaborator, Miklós Szoboszlay constrained the *baseline drift* and p_{nonlin} values by fitting unitary and 5 AP-evoked [Ca^{2+}] transients recorded in individual PCs (n = 37 cells; ***Figure 28A-C***). Next, he generated synthetic data with MLspike using experimentally measured peak amplitudes, decay times, SNR of unitary [Ca^{2+}] transients, the corresponding *baseline drift* and p_{nonlin} values with spike timings obtained from Poisson distributions at 0.1 Hz, 1 Hz, and 10 Hz (***Figure 28D, F, H***). I applied 4 different fitting scenarios to investigate the parameters that critically influence the error rate (ER): 1) fitting the transients with the amplitude, decay, *baseline drift* and p_{nonlin} values used to generate the data; 2) mean decay value of the 37 cells with the cell's own amplitude, *baseline drift* and p_{nonlin} values; 3) mean amplitude value of the 37 cells, with the cell's own decay, *baseline drift* and p_{nonlin} values; 4) the mean amplitude, decay, *baseline drift* and p_{nonlin} values of the 37 cells. The first scenario resulted in virtually zero errors for all tested mean firing frequencies (red in ***Figure 28E,G,I***). Similarly, low ERs were obtained when the mean decay time constant was used at frequencies <10 Hz (orange in ***Figure 28E,G***). However, when the mean peak amplitude was used, the ER was substantially higher at all frequencies (0.1 Hz: ER = 25.3 ± 33.7%, median = 1.8%, IQR: 0 - 33.1%; 1 Hz: ER = 26.2 ± 30.8%, median = 9.3%, IQR: 0.3 - 46.2%; 10 Hz: ER = 17.4 ± 20.2%, median = 8.9%, IQR: 0.3 - 29.5%; cyan in ***Figure 28E,G,I***), similar to the scenario when all parameters used for fitting were the mean values of the 37 cells (0.1 Hz: ER = 22.9 ± 34.2%, median = 1.9%, IQR: 0 - 33.2%; 1 Hz: ER = 27.4 ± 32.9%, median = 9.5%, IQR: 0 - 51.9%; 10 Hz: ER = 26.5 ± 24.5, median = 16%, IQR: 9.6 - 47.3%; blue in ***Figure 28E,G,I***; Three-Way ANOVA: $p < 0.01$ for scenarios; $p > 0.05$ for frequency; $p > 0.05$ for scenarios*frequency interaction).

DOI:10.14753/SE.2019.2319

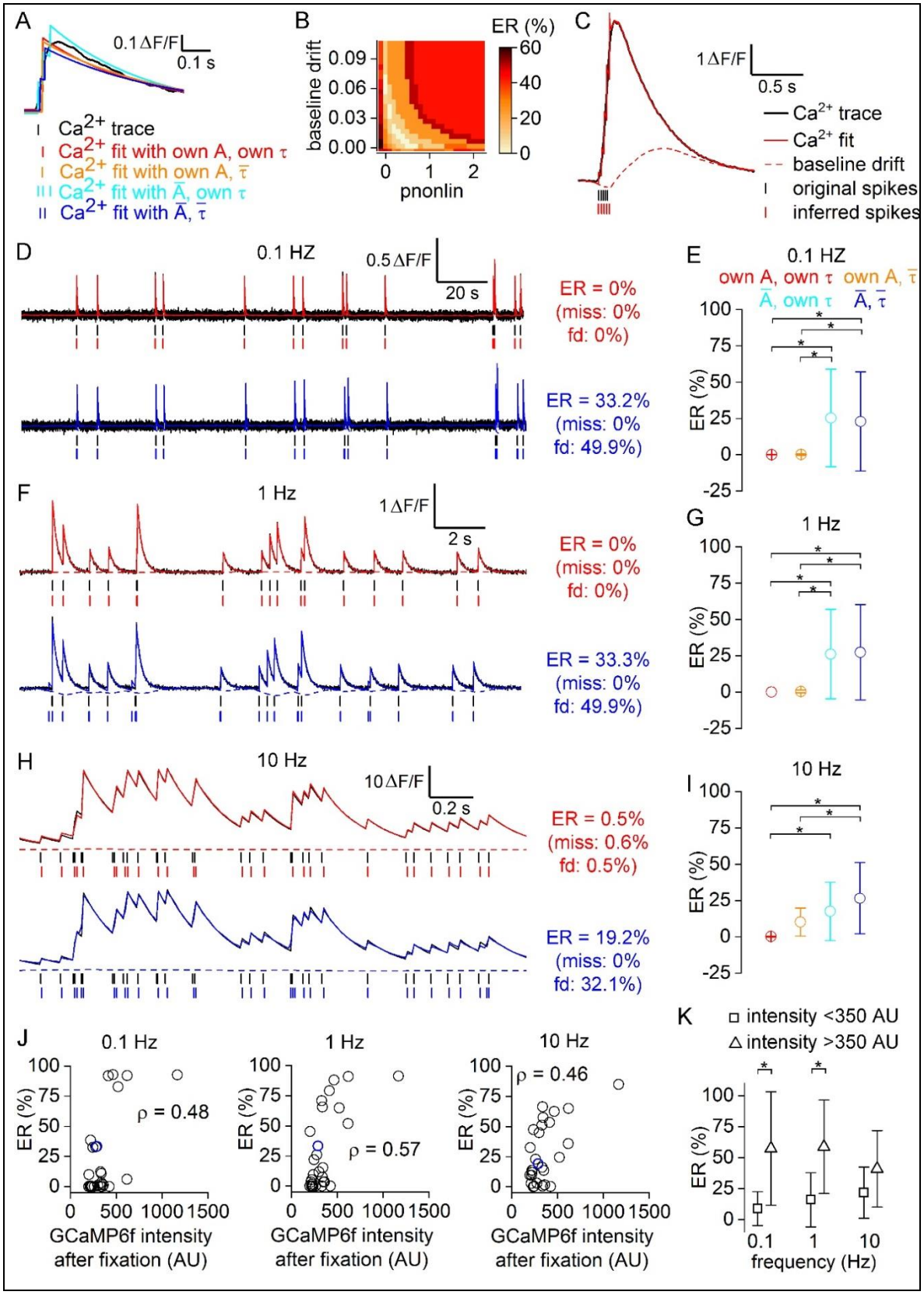

Figure 28. Cell-to-cell variability in the peak amplitude of unitary GCaMP6f [Ca^{2+}] transients leads to inaccurate spike inference.

(A) A single AP evoked [Ca^{2+}] transient (black trace) and the best fit using MLspike with the following four scenarios: 1) own amplitude and own decay time constant (red, own A and own τ); scenario 2) own amplitude and mean decay time constant (orange, own A, $\bar{\tau}$); scenario 3) mean amplitude and own decay time constant (cyan, $\bar{A}$, own τ); scenario 4) mean amplitude and mean decay time constant (blue, $\bar{A}$ and $\bar{\tau}$). (B) The inference error rate (ER) of a [Ca^{2+}] transient evoked by 5 APs at 50 Hz is plotted as a function of p_{nonlin} and *baseline drift* parameters. (C) Fitting of a [Ca^{2+}] transient evoked by 5 APs at 50 Hz using those maximal p_{nonlin} and minimal *baseline drift* values that resulted in minimal ER. (D, F, H) Representative synthetic [Ca^{2+}] traces and inference spike traces calculated with own peak amplitude and decay time constant (red) or with mean peak amplitude and mean decay time constant (blue) values. miss: missed APs; fd: false detection (60 ms tolerance window). Traces were generated with Poisson spike trains with 0.1 Hz (D), 1 Hz (F) and 10 Hz (H). (E, G, I) ERs for the different inference scenarios. (J) Correlations of ERs and GCaMP6f intensity values (0.1 Hz: $p < 0.01$; 1 Hz: $p < 0.01$; 10 Hz: $p = 0.014$; $n = 28$; Spearman correlation). (K) ERs for low intensity cells (< 180 AU, $n = 20$) are significantly smaller compared to high intensity cells (> 180 AU, $n = 8$). Statistic for panels E, G, I, K: Three-Way ANOVA: $p < 0.01$ for intensity; $p < 0.01$ for scenarios; $p > 0.05$ for frequency; $p < 0.01$ for intensity*scenarios interaction; $p > 0.05$ for intensity*frequency interaction; $p > 0.05$ for scenarios*frequency interaction; $p > 0.05$ for intensity*scenarios*frequency interaction; * < 0.05 pairwise Bonferroni *post hoc* test.

The ERs in the 4th scenario (all parameters were the mean of 37 cells) depended on the difference between the cell's unitary peak amplitudes and the mean amplitude; the ER was negligible when the difference was small (***Figure 29 A-C***). This is explained by a larger fraction of missed APs for cells with lower unitary peak amplitudes (***Figure 29 D-F***) and by a larger fraction of incorrectly detected APs for cells with higher unitary peak amplitudes (***Figure 29 G-I***). These data support the key role of the variance in the amplitude of the unitary [Ca^{2+}] transients in determining the precision of spike inference.

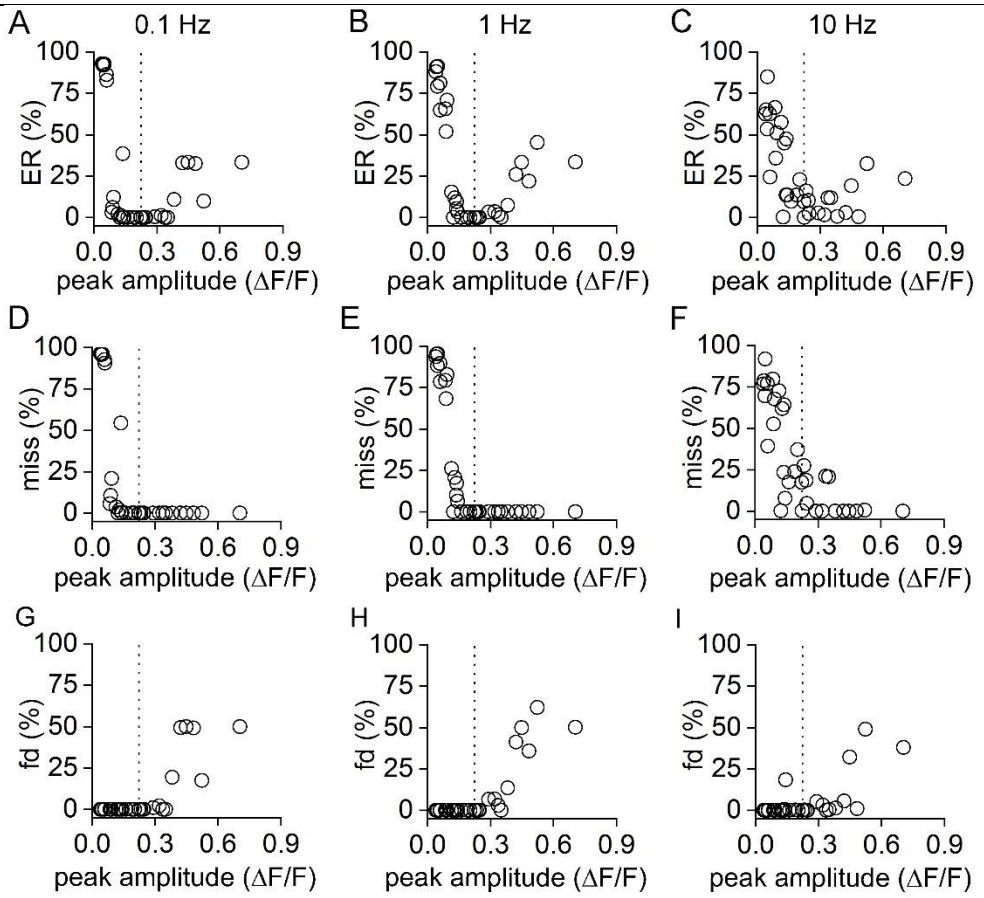

Figure 29. Correlation of spike inference error rates and peak amplitude of unitary [Ca^{2+}] transients.

(A- C) ER is low for cells with peak amplitudes similar to the mean unitary peak amplitude (indicated by the vertical dashed line) at each tested firing frequency. (D-F) The fraction of missed APs is higher for cells with small unitary peak amplitudes. (G-I) The fraction of falsely detected APs is higher for cells with large unitary peak amplitudes. (A, D, G: 0.1 Hz, B, E, H: 1 Hz, c, F, I: 10 Hz; n = 33 cells). The ER is the harmonic mean of the false detections and the fraction of missed spikes.

My analysis also revealed that the ER (4th scenario) and GCaMP6f intensity show significant positive correlations at all frequencies (0.1 Hz: $\rho = 0.5$, $p < 0.01$; 1 Hz: $\rho = 0.59$, $p < 0.01$; 10 Hz: $\rho = 0.46$, $p = 0.013$; n = 28; Spearman correlation; ***Figure 28J***). When the cells were grouped based on their native GCaMP6f intensities into low (<180 AU, n = 20) and high (>180 AU, n = 8) expressing groups, the ERs were found to be significantly smaller

for weakly expressing cells at 0.1 Hz and 1 Hz (Three-Way ANOVA: $p < 0.01$ for intensity; $p < 0.01$ for intensity*scenarios interaction; $p > 0.05$ for intensity*frequency interaction; $p > 0.05$ for intensity*scenarios*frequency interaction; pairwise Bonferroni *post hoc* test: 0.1 Hz: $p < 0.01$, 1 Hz: $p < 0.01$, 10 Hz: $p > 0.05$; ***Figure 28K***).

These results demonstrate that the key parameter that critically determines the spike inference ER is the peak amplitude of the unitary [Ca^{2+}] transients. Furthermore, my data also provides clear evidence that the ER for weakly GCaMP6f expressing cells is significantly lower than that for the strongly expressing ones.

5.2.6. Reduction of spike inference error by fitting with the estimated peak amplitudes of unitary [Ca^{2+}] transients

In the final set of simulations, I generated [Ca^{2+}] fluorescent traces using the amplitude and decay of unitary [Ca^{2+}] transients recorded in 20 PCs that weakly expressed GCaMP6f (<180 AU), their respective *baseline drift*, p_{nonlin} parameters, noise and the spike timings of randomly selected 20 CA1 PCs recorded from behaving animals using tetrodes (obtained from Grosmark, A.D., Long J. and Buzsáki, G; CRCNS.org; http://dx.doi.org/10.6080/K0862DC5, Grosmark and Buzsáki, 2016). The distribution of the mean firing rates of the PCs was positively skewed (n = 48 cells) and was very similar for the 20 subselected cells compared to the 48 cells of the dataset ($p = 0.27$, Two-Sample Kolmogorov-Smirnov test; ***Figure 30A***).

Because our previous simulations revealed that the amplitude of unitary [Ca^{2+}] transients is the key parameter in determining the ER, I aimed at determining the amplitude of unitary [Ca^{2+}] transients from the fluorescent traces with a model independent and a model dependent method. For this, first, I analysed the spike times of *in vivo* recorded CA1 PCs. Because the amplitude of a [Ca^{2+}] transient increases substantially when it is preceded by a burst, I selected APs, which were preceeded by at least a 4 second silent period. I also aimed a short (1s) silent period after the spike to be able to reliably measure the amplitude of the [Ca^{2+}] transients. In the analysed 20 *in vivo* recorded spike trains, 10.4 ± 5.5 % of the APs fulfilled these criteria. However, the slow kinetics of GCaMP6f [Ca^{2+}] transients does not allow the unequivocal distinction between single AP-evoked and isolated high-frequency

(inter spike interval (ISI) < 20 ms) burst-evoked [Ca^{2+}] transients; therefore, I also calculated the percentage of such bursts. I found that among such temporally separated events, 77.6 ± 8.4 % were single APs with a minimum of 63.6%, and the remaining ones were bursts of APs. Thus, I argued that if I detect [Ca^{2+}] transients that are separated by 4 and 1 seconds from other transients (15 ± 8 % of the total transients), the smallest two-third of them will be likely single AP-evoked '*presumed unitary'* [Ca^{2+}] transients. Then, I detected [Ca^{2+}] transients in all 20 synthetic fluorescent traces, from which I selected such temporally segregated events and calculated the mean of the amplitudes of the smallest 2/3 of them. The ratio of the '*presumed unitary*' and the real amplitude of the [Ca^{2+}] transients was 1.01 ± 0.05 (median = 1, IQR: 0.98 - 1.02), and even the largest error was only 16% (***Figure 30B***), indicating that this method provides an excellent estimate of the amplitude of unitary [Ca^{2+}] transients. Due to spike sorting issues, especially in case of bursts of APs (Buzsáki, 2004), the calculations of the fraction of single AP-s and burst of APs from the isolated events can be erroneous. However, the burst-evoked [Ca^{2+}] transients have much larger peak amplitudes compared to the single AP-evoked responses; therefore, it should be reflected by a larger, separate peak on the amplitude distributions. In such cases, the amplitude of the first peak of the distribution should be applied. In our data, the accuracy of such an estimation of '*presumed unitary*' [Ca^{2+}] transients was almost identical (1.05 ± 0.05; largest error: 23%) to that described above.

In a second method, I selected those [Ca^{2+}] transients that were inferred by MLspike as single AP-evoked ones in a scenario where mean amplitude (0.248 ΔF/F), decay time constant (388 ms), p_{nonlin} (0.56) and *baseline drift* (0.011) parameters of the 20 PCs (only weakly GCaMP6f expressing cells) were used for fitting (blue in ***Figure 30D***). I only included such detected unitary events in our analysis if they were temporally segregated from other events (>4s before and >1s after). The accuracy of this estimation method was slightly lower than that of my first method; the ratio of '*detected unitary*' and real peak amplitude was 1.08 ± 0.17 (median = 1, IQR: 0.97 - 1.16, max = 1.51). The main inaccuracies occurred for cells with small unitary peak amplitudes resulting in a significant negative correlation between the real peak amplitude and the ratio of '*detected unitary*'/real amplitudes (ρ = -0.78, $p < 0.01$; Spearman correlation, ***Figure 30C***).

Next, I hypothesised that by using the reasonably accurately estimated peak amplitude (‘*presumed unitary*’ and ‘*detected unitary*’) of each cell, the mean decay time constant (388 ms), p_{nonlin} (0.56) and *baseline drift* (0.011), inference error should be smaller compared to the scenario when all parameters were the means of the 20 PCs. Indeed, the ERs was significantly reduced ($p = 0.01$, Friedman ANOVA test; ***Figure 30G***) from 15.0 ± 15.2 % to 6.3 ± 4.9 % when the ‘*presumed unitary*’ amplitude (green in ***Figure 30G***; Paired Sample Wilcoxon Signed Rank *post hoc* test: $p < 0.01$) and to 6.4 ± 4.8 % when the ‘*detected unitary*’ amplitude was used for fitting (purple in ***Figure 30G***; Paired Sample Wilcoxon Signed Rank *post hoc* test: $p < 0.01$). The ER did not show significant correlation with the estimated unitary peak amplitudes in either of the scenarios (***Figure 30E***,***F***). These results further support the key role in the variability of peak amplitudes in spike inference accuracy, whereas the decay time constant, p_{nonlin} and *baseline drift* contribute to only a minor part of the ER (~6%). Indeed, the ER was reduced to virtually zero when in addition to the estimated amplitudes, the original decay time constant, p_{nonlin} and *baseline drift* values were used (‘*presumed unitary*’: ER = 0.05 ± 0.13 %, median = 0%, IQR: 0 - 0%; ‘*detected unitary*’: ER = 0.09 ± 2.35%, median = 0%, IQR: 0 - 0.05%).

DOI:10.14753/SE.2019.2319

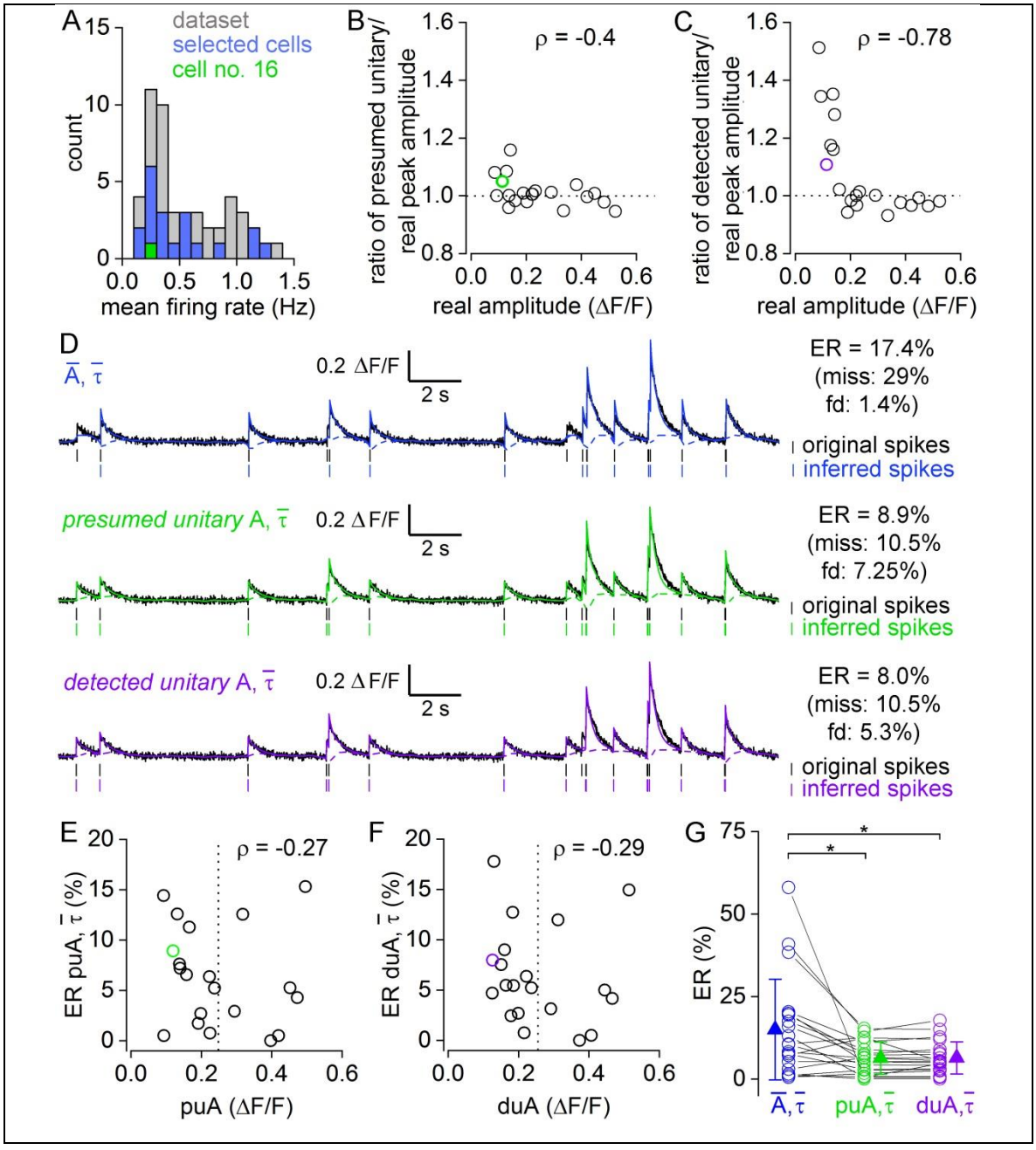

Figure 30. The error rate (ER) in spike inference can be reduced by using estimated unitary peak amplitudes.

(A) The distribution of mean firing rates of CA1 PCs obtained from Grosmark, Long and Buzsaki (CRCNS.org, http://dx.doi.org/10.6080/K0862DC5; Grosmark and Buzsáki, 2016; n = 48 cells), and that of the subselected cells (n = 20) used for generation of synthetic [Ca^{2+}] traces here (p = 0.27, Two-Sample Kolmogorov Smirnov test). (B) Original peak amplitudes, used for generation of synthetic data, are estimated correctly from the peak amplitudes of isolated '*presumed unitary*' [Ca^{2+}] transients for the whole range of amplitudes (n = 20 cells; p > 0.05, Spearman correlation). (C) Accuracy of estimating peak amplitudes from [Ca^{2+}] transients detected by MLspike as single AP-evoked ('*detected unitary*') correlates negatively with the real peak amplitudes (n = 20 cells; p < 0.01, Spearman correlation). Synthetic data generated with unitary [Ca^{2+}] amplitudes > 0.2 ΔF/F allows the accurate detection of the original unitary [Ca^{2+}] amplitude. (D) Synthetic [Ca^{2+}] traces generated with an in vivo recorded spike timing (black, [Ca^{2+}] trace; blue, green, and purple [Ca^{2+}] fits; dotted dashed blue, green, and purple, baseline drift). Inferring spikes using MLspike with the mean unitary [Ca^{2+}] transient amplitude and decay (blue) and with the '*presumed unitary*' (green) or '*detected unitary*' (purple) [Ca^{2+}] transient amplitude and mean decay (green, respectively purple). (E, F) Peak amplitude of '*presumed unitary*' (E) or '*detected unitary*' (F) [Ca^{2+}] transients does not correlate with the ER (n = 20). (F) (G) Summary plot showing significant reduction in ER (n = 20; p = 0.01, Friedman ANOVA test) when spike inference is performed using peak amplitude of '*presumed unitary*' [Ca^{2+}] transients (green; Paired Sample Wilcoxon Signed Rank post hoc test: p < 0.01) or using the amplitude of '*detected unitary*' [Ca^{2+}] transients (purple; Paired Sample Wilcoxon Signed Rank post hoc test: p < 0.01). puA: '*presumed unitary*' amplitude; duA: '*detected unitary*' amplitude.

DOI:10.14753/SE.2019.2319

6. DISCUSSION

In my dissertation I first investigated the mechanism of an intriguing form of molecular regulation of synaptic properties, the target cell-type dependent release probability. Distinct molecular compositions underlie the capability of neuronal networks to form diverse synaptic connections with distinct efficacy of information transfer. Investigating the role of this synaptic diversity in a behavioral context dependent manner is hampered by the limitations of currently available large-scale recording techniques. Therefore, in the second part of my dissertation I aimed to elucidate the sources of these limitations in case of the most widely used Ca^{2+} imaging technique using GCaMP6f; based on which, I aimed to improve the reliability of spike inference from the underlying Ca^{2+} traces.

In the first part of my thesis, the short-term synaptic plasticity measurements of CA3 PC inputs onto PV^+ or mGluR1α^+ INs that I have performed, indicate a different initial release probability at these synapses. Moreover, I show that the [Ca^{2+}] influx upon a single AP is significantly larger in case of high P_r synapses. These results, together with the parallel experiments of my colleague (Noemi Holderith: measurement of AZ area and bouton volume ratios) allowed the determination of the functional Ca^{2+} channel density. We found an almost twofold higher density in the AZs innervating PV^+ dendrites compared to those innervating mGluR1α^+ INs. This is the consequence of a larger presynaptic [Ca^{2+}] transient, a smaller AZ area, and a similar volume of boutons innervating PV^+ INs (Éltes et al., 2017). In parallel another colleague, Tekla Kirizs determined the densities of immunogold particles labeling the Cav2.1 and Cav2.2 Ca^{2+} channel subunits using sodium dodecylsulphate- digested freeze-fracture replica labeling (SDS-FRL) and she found that PV^+ dendrite-innervating terminals exhibited only a 1.15 times higher Ca^{2+} channel subunit density (Éltes et al., 2017). My further experiments aimed to test potential explanations for this discrepancy. My results excluded a difference in the contribution of VGCC to the [Ca^{2+}] transients and in buffer capacity, permitting us to draw the conclusion that a target cell-type dependent modulation of [Ca^{2+}] function or different subunit composition is the most likely underlying cause of the differing P_r at these synapses.

My Ca^{2+} imaging experiments are consistent with the results of Koester and Johnston (Koester and Johnston, 2005), who performed simultaneous paired whole-cell recordings and imaged [Ca^{2+}] transients in presynaptic boutons mediating either facilitating or depressing EPSPs in the neocortex. They also observed a larger presynaptic [Ca^{2+}] transient in depressing PC to multipolar cell synapses compared with those mediating facilitating EPSPs in bitufted cells. However, the difference in the recorded cortical boutons was more robust than that found in my present study in CA3 PCs. Koester and Johnston (2005) did not provide ultrastructural information regarding the bouton volume or AZ size, so the basis for the difference in [Ca^{2+}] between the depressing and facilitating synapses could not be determined. My data (pooled with that of Noemi Holderith's) thus extends the current knowledge by demonstrating that the larger [Ca^{2+}] in high P_r, FS PV^+ IN-innervating boutons is not the consequence of a smaller bouton volume, but rather is caused by a larger amount of Ca^{2+} entering the bouton upon an AP. Noemi Holderith, additionally, determined the size of the AZs (where Ca^{2+} channels are concentrated), therefore in our study we could predict the [Ca^{2+}] in the vicinity of the release sites. Assuming similar Ca^{2+} channel properties in different P_r boutons, our data predict a 1.7–1.9 times higher density of Ca^{2+} channels in high P_r AZs (Éltes et al., 2017). However, results of Tekla Kirizs, who performed quantitative evaluation of several hundreds of AZs with SDS-FRL for both Cav2.1 (P/Q) and Cav2.2 (N-type) Ca^{2+} channel subunits in AZs attached to $Kv3.1b^+$ (which co-localizes with PV^+) or $mGluR1\alpha^+$ somatodendritic membranes revealed only a ~15% higher [Ca^{2+}] channel density in the $Kv3.1b^+$ dendrite-innervating AZs (Éltes et al., 2017). A potential explanation for the discrepancy between our functional channel density and her SDS-FRL Cav subunit density estimates is a preferential enrichment of Cav2.3 (R-type)/Cav1 (L-type)/Cav3 (T-type) subunits in PV^+ dendrite-innervating boutons (Parajuli et al., 2012; Carbone et al., 2014). However, my experiments with 1 μM ω-CTX MVIIC revealed an almost identical block of [Ca^{2+}] transients in boutons targeting these distinct IN types, arguing against differential contribution of R-, T-, and L-type Ca^{2+} channels to the [Ca^{2+}] transients. Another possible explanation for this discrepancy is a differential fixed Ca^{2+} buffer concentration in these two bouton populations. However, the similar decay of the [Ca^{2+}] transients (recorded with either 300 or 100 μM Fluo5F) in these bouton populations argues against this possibility. My results

in concert with those of Noemi Holderith's and Tekla Kirizs' provide evidence that differential target cell type-dependent regulation of Ca^{2+} channel function is the most likely mechanism underlying the differences in release probability.

There are a number of ways to regulate Ca^{2+} channel function. Association with different β subunits promotes different voltage-dependent activation and inactivation (for review, see Buraei and Yang, 2010 (Buraei and Yang, 2010). Interactions with SNARE proteins such as syntaxin and SNAP25 at the so-called "synprint" motif reduce the channel open probability, whereas additional coexpression of synaptotagmin reverses this effect (Zhong et al., 1999). This suggests a regulatory switch by which presynaptic Ca^{2+} channels bound to Ca^{2+} sensors are functionally enabled, whereas Ca^{2+} channels decoupled from Ca^{2+} sensors are disabled (Eggermann et al., 2011). The AZ protein Munc13, which is involved in vesicle priming processes, has also been found to alter Ca^{2+} inflow by modulating the kinetic properties of Ca^{2+} channels without changing their density (Calloway et al., 2015). Probably the most widely studied modulation of Ca^{2+} channel function is its regulation by presynaptic G-protein-coupled receptors (e.g., mGluRs, A1 adenosine- α2 noradrenergic, $GABA_B$, or endocannabinoid receptors (Bean, 1989; Dittman and Regehr, 1996; Takahashi et al., 1996; Leão and Von Gersdorff, 2002; Brown et al., 2004; Szabó et al., 2014; Kupferschmidt and Lovinger, 2015). P/Q- and N-type Ca^{2+} channel function is reduced via direct binding of G-protein β/γ -subunits to Ca^{2+} channel β subunits. In a recent study, Anderson et al. (2015) demonstrated that presynaptic β neurexins can reduce tonic endocannabinoid production transsynaptically and increase the P_r of CA1 PC axons by alleviating presynaptic [Ca^{2+}] from CB1-mediated inhibition (Anderson et al., 2015). Another way of modulating Ca^{2+} channel function is phosphorylation: CDK5 (kinase)/calcineurin (phosphatase) equilibrium has been shown to set the phosphorylation state of the α1 subunit of N-type Ca^{2+} channels, which influences the voltage dependence of the open probability of the channel (Su et al., 2012; Kim and Ryan, 2013). Whatever the mechanisms are, they must be able to modulate the function of presynaptic Ca^{2+} channels in a postsynaptic target cell type-dependent manner. The amount of Ca^{2+} entering through presynaptic voltage-gated Ca^{2+} channels is very sensitive to the shape/waveform of the AP (Geiger and Jonas, 2000) so a postsynaptic target cell type-dependent difference in the AP waveform could also explain our results. It remains

to be seen whether the AP waveform in boutons (Rowan et al., 2014) that are segregated by only a few micrometers along the same axon could be sufficiently different to account for the ~30% difference in the [Ca^{2+}] transient observed in our experiments. The larger amount of Ca^{2+}, together with a higher docked vesicle density in high P_r boutons, indicates a higher [Ca^{2+}] at the Ca^{2+} sensors. Rozov et al. (Rozov et al., 2001) tested the transmission between cortical PCs and two distinct IN types (multipolar and bitufted) with fast and slow Ca^{2+} buffers. The more robust effect of EGTA (slow buffer) on neurotransmitter release from PC to bitufted compared with multipolar cells predicted a larger physical distance between the Ca^{2+} channels and Ca^{2+} sensors (larger coupling distance) in the low P_r synapse. Our functional Ca^{2+} channel density estimate is consistent with this prediction and supports the hypothesis that the mechanisms underlying the low initial P_r and the subsequent short-term facilitation is a large Ca^{2+} channel to Ca^{2+} sensor distance (Neher, 1998; Atwood and Karunanithi, 2002; Eggermann et al., 2011). Another level of complexity might arise from the potential target cell type-dependent differences in the sub-AZ distribution of Ca^{2+} channels (Holderith et al., 2012; Nakamura et al., 2015).

So far, the only known protein with a dramatic difference in its density between low- and high-P_r synapses of a single PC axon is mGluR7 (Shigemoto et al., 1996), making it an ideal candidate through which a low initial P_r and a consequent short-term facilitation could be achieved. The pharmacological blockade of group III mGluRs (including mGluR7) increases the amplitude of evoked EPSCs, but does not change the facilitating phenotype of EPSCs recorded from CA1 mGluR1α^+ INs (Losonczy et al., 2003), suggesting a tonic, mGluR-mediated reduction of transmitter release from these axon terminals. Similarly, knocking down Elfn1 from SOM^+ INs also led to an increase in the amplitude of the first EPSC of a train and a reduction in the degree of short-term facilitation, consistent with the results of pharmacological block of mGluR7. Indeed, it has been shown recently that the postsynaptically located Elfn1 has a key role in the selective recruitment of mGluR7 to the presynaptic AZs of PC axons that contact SOM/ mGluR1α^+ INs (Tomioka et al., 2014). However, the short-term plasticity of the mGluR1α^+ dendrite-targeting boutons in mGluR7 antagonist or after Elfn1 knock-down is still facilitating, very different from that observed in PV^+ IN-targeting boutons, suggesting that other mechanisms must be involved. These might

include the regulation of Ca^{2+} channel function mentioned above or the selective presence of molecules that might impose facilitation on synapses (e.g., NMDA receptors, (Buchanan et al., 2012); kainate receptors, (Sylwestrak and Ghosh, 2012); or synaptotagmin-7, (Jackman et al., 2016). Additional factors could contribute to differences in initial P_r by changing the sensitivity of the release machinery to $[Ca^{2+}]$. Proteins such as Rab3A-D and Munc13-3 increase P_r (Schlüter et al., 2004, 2006; Ishiyama et al., 2014), whereas others such as mover decrease *Pr* (Körber et al., 2015) without affecting the readily releasable pool. Unc13 isoforms have been implicated in the preferential targeting of vesicles to docking sites that are formed at varying distances from the Ca^{2+} channels (Böhme et al., 2016). Any of these mechanisms may also contribute to the differences in initial *Pr* in addition to the above described differences in $[Ca^{2+}]$.

The hypothesis that distinct molecular mechanism can underlie the different efficacy of the information transfer of short-term depressing and facilitating synapses, at low and high frequency activity respectively, is at present generally accepted. The molecular and functional heterogeneity in concert with the complex organization of efferents and afferents could support the emergence of biased excitatory-inhibitory microcircuits in the hippocampus that could dynamically regulate routing of information (Soltesz and Losonczy, 2018).

Current methods for the in-depth investigation of the extent to which these diverse synaptic properties shape the transformation of the activities of individual neurons into complex behaviors are limited (Broussard et al., 2014; Jercog et al., 2016; Lin and Schnitzer, 2016). Currently, *in vivo* two-photon Ca^{2+} imaging using GCaMP6f, genetically encoded Ca^{2+} indicator, is one of the most widespread tecniques applied to answer this question. However, the current models/ algorithms/ software used to decipher the neuronal activity underlying the GCaMP6f fluorescence traces are inaccurate. Understanding the sources of these limitations and devising new, more accurate procedures are necessary. In the second part of my thesis I demonstrated that the variability of peak amplitudes of GCaMP6f $[Ca^{2+}]$ transients recorded *in vivo* in a population of cells is not only the consequence of the mixture of single APs and high-frequency bursts, but also due to a substantial cell-to-cell variability in the peak amplitude of unitary $[Ca^{2+}]$ transients and the variable degree of supralinearity of

GCaMP6f. I also show that the expression level of GCaMP6f is highly variable among CA1 PCs, partially underlying the variability in the amplitude, decay and summation of unitary [Ca^{2+}] transients. However, to my surprise, substantial variability is still observed in the peak amplitude and supralinearity when PCs with similarly low GCaMP6f expression were subselected. Our modelling with MLspike revealed that the main source of spike inference error is the variability in the peak amplitude, and not in the decay or supralinearity (Éltes et al., 2019, modelling performed together with Miklos Szoboszlay). I developed two procedures to estimate the peak amplitudes of unitary [Ca^{2+}] transients in CA1 PCs and show that spike inference performed with MLspike using these unitary amplitude estimates in weakly GCaMP6f expressing cells results in error rates of ~6%.

I determined for the first time the expression level of GCaMP6f in functionally characterized nerve cells, allowing me to correlate the amplitude, kinetics and supralinearity of unitary fluorescent [Ca^{2+}] transients with the amount of genetically encoded Ca^{2+} indicators. I estimated the expression level of GCaMP6f 1) by measuring its native fluorescence in aldehyde fixed tissue, arguing that this measure should not reflect differences in [Ca^{2+}]; and 2) with anti-GFP immunohistochemistry. My collaborator's, Katalin Szigeti's experiments revealed a very tight correlation between the intrinsic GCaMP6f fluorescence and anti-GFP immunoreactivity providing a strong support for the notion that the intrinsic fluorescence of GCaMP6f in fixed tissue is an excellent measure of the protein level (Éltes et al., 2019). Determining the expression level of GCaMP6f in every imaged cell after dense population recordings is laborious, therefore I also analysed the relationship between the intrinsic GCaMP6f fluorescent intensities as measured in acute slices with two-photon microscopy and those measured after fixation. The weak correlation, with very low predictive power at low intensities, indicates that the resting fluorescence of GCaMP6f in living tissue is not a reliable indicator of the amount of GCaMP6f protein irrespective whether 810 nm or 925 nm excitation laser was used. Therefore, I conclude that reliable measurement of the expression level of GCaMP6f requires analysis of fluorescent intensities after chemical fixation. I also suggest that applying a cut off value of ~5% intensity of the most intensely labelled cells or ~30% intensity value of the mean intensity of the population should be applied to subselect cells in which the unitary [Ca^{2+}] transients should have large amplitudes

with favourable SNR. Such intensity-subselection resulted in the exclusion of approximately one third of the cells.

I simultaneously measured electrically the APs and optically GCaMP6f [Ca^{2+}] transients in acute hippocampal slices and not *in situ* in the brain, but I argue that my approach of using cell-attached recordings with antidromic stimulation, has the advantage of permitting the *post hoc* identification of the unlabeled cells and of performing such experiments in hundreds of PCs. The size of my data is substantially larger than that of *in vivo* recordings and my data is not confined to monitoring naturally occurring spike trains, but I was able to perform the same, standardized protocols (e.g. single AP, bursts with different frequencies and spike number, recovery protocol) for all recorded cells. My results demonstrate large variance in the peak amplitude of single AP-evoked unitary GCaMP6f [Ca^{2+}] transients in hippocampal CA1 PCs (CV= 0.96 for all recorded cells; CV = 0.95 for temporally isolated unitary events in 35 cells; CV = 0.73 for temporally isolated unitary events in cells with low GCaMP6f expression, n = 15). The cell-to-cell variability in [Ca^{2+}] transients in visual cortical *in vivo* recorded cells using GCaMP6f or GCaMP6s (Greenberg et al., 2018) was somewhat smaller (CV = 0.5 and 0.6, respectively), which might be the consequence of differences between hippocampal and visual cortical PCs or differences between *in vitro* and *in vivo* conditions, including the temperature (room vs. body temperature). Indeed, the peak amplitude of single AP-evoked [Ca^{2+}] transients and its variance is known to depend on the preparations (hippocampal slice cultures, acute cortical slices, *in vivo*) and recording conditions (Mao et al., 2008; Tian et al., 2009; Akerboom et al., 2012; Ohkura et al., 2012; Chen et al., 2013). Biological variation in the behavior of GCaMP6f among distinct nerve cell types is also plausible, because the ionic strength and the composition of the intracellular milieu has been shown to affect the affinity, cooperativity, and dynamic range of GCaMPs (Hires et al., 2008). However, the parameters responsible for the variability among cell types and among individual cells of the same types are unknown.

Biophysical and biochemical mechanisms can potentially account for such complexities. Greenberg and colleagues developed a kinetic model and proposed that the

cooperativity across the four Ca^{2+} binding sites of GCaMP, the slow and multiphasic kinetics of the indicator, and the total GCaMP concentration can account for variability and nonlinearity of GCaMP-reported fluorescent transients (Greenberg et al., 2018). Moreover, GCaMP molecules display two states with different fluorescent properties. The dimeric form, though less prevalent, contributes to background fluorescence of the GCaMP expressing cells, however it is [Ca^{2+}] insensitive (Akerboom et al., 2009) and can complicate the interpretation of fluorescent transients. Some mutations have been shown to result in photoisomerization (Akerboom et al., 2009), or in the accumulation of non-responsive proteins in lysosomes (jRGECO1a, Dana et al., 2016). It has also been shown that GCaMP-associated calmodulin disrupt Ca^{2+} influx and dynamics, and gene expression by affecting the gating of L-type Ca^{2+} channels in an expression-dependent manner (Yang et al., 2018).

I also demonstrated that peak amplitude of unitary [Ca^{2+}] transients is not only different among cell types and among cells of the same type, but also varies according to the cell's firing history. The use-dependent nonlinearity of ΔF/F has been reported previously (Mao et al., 2008; Tian et al., 2009; Akerboom et al., 2012; Ohkura et al., 2012; Chen et al., 2013) and is probably a result of the cooperativity of calcium binding by calmodulin. We provide a first evidence for a >2 fold increase of the unitary peak amplitude after a high frequency burst (10 AP at 50 Hz), and for the extremely slow recovery time course (~4 s) from this process. The mechanism underlying this long time-constant of the burst-evoked potentiation of unitary responses is probably different from that which underlies the supralinearity of the GCaMP6f responses within bursts (e.g. [Ca^{2+}]-dependent association constants (Nakai et al., 2001) or different Ca^{2+} binding sites with different on and off rates). I also provide first evidence for variable degrees of supralinearity of GCaMP6f among CA1 PCs and its weak dependcy on the expression level of the sensor.

The expression level of the [Ca^{2+}] indicator is thought to play a key role in defining [Ca^{2+}] transients. Lower concentration of Ca^{2+} indicators should report the same [Ca^{2+}] with higher peak amplitude, faster kinetics and lower SNR (Hires et al., 2008; Broussard et al., 2014; Dana et al., 2014). Unexpectedly, my results show, that even though there is a significant negative correlation between the peak amplitude and GCaMP6f expression, in case of cells with similarly low intensities the variance remains substantial (CV = 0.56 -

0.75); therefore, homogenisation of the expression level by using transgenic mice (e.g. Dana et al., 2014) might not provide a sufficient solution for the problem. One explanation of these results is a cell-to-cell variability in Ca^{2+} influx upon single APs, resulting in a different intracellular [Ca^{2+}] that will be reported as a highly differing fluorescence change upon the same stimulation. However, the lack of correlation of the unitary [Ca^{2+}] transients with the AP width or with the surface to volume ratio, and the lack of differences between peak amplitudes and decay time constants in cells with potentially different endogenous buffers, provide evidence that the substantial variability in unitary GCaMP6f [Ca^{2+}] transients and its summation are likely due to differences in the aforementioned intrinsic properties of GCaMP6f instead of a different [Ca^{2+}]. This hypothesis is supported by the results of recordings with a synthetic dye (Fluo5F) in CA1 PCs not expressing GCaMP6f, showing much more uniform unitary [Ca^{2+}] transients among CA1 PCs. However, a plausible explanation is that the nonlinear reporting characteristic of GCaMP6f enhances the smaller variation in the Ca^{2+} influx.

I demonstrate that cell-to-cell variability of the peak amplitude of unitary [Ca^{2+}] transients is a key source of spike inference ER on simulated data (with experimentally derived parameters, performed together with my colleague Miklos Szoboszlay, Éltes et al., 2019) using the MLspike algorithm (Deneux et al., 2016). Fitting with mean peak amplitude, but own decay time constants, p_{nonlin} and *baseline drift* parameters results in a similarly high ER compared to fitting with the mean of all parameters. Our ER with the mean parameters is similar to that obtained by (Deneux et al., 2016) and also by a recent study using simple non-negative deconvolution (Pachitariu et al., 2018). During *in vivo* optical recordings, the unitary peak amplitude of the several hundreds of recorded cells is not available; nonetheless, our results indicate that a decrease in spike inference ER may already be achieved by subselecting cells based on their GCaMP6f expression level. In the weakly expressing cell population, I was able to accurately estimate the unitary peak amplitude with a model-independent ('*presumed unitary*') and a model-dependent ('*detected unitary*') procedure. Providing either of these estimated peak amplitudes to MLspike resulted in a significant reduction of the spike inference ER. Even though I do not provide a direct comparison of the performance of several softwares on the same dataset, based on the literature (Deneux et al., 2016; Theis et al., 2016;

Pachitariu et al., 2018) there is no other spike inference algorithm or model that can estimate spiking activity with such low ERs (~5%). Importantly, this low ER is achieved in our simulations with a detection window (60 ms) that is an order of magnitude briefer than that used by others. The use of spiking statistics for the estimation of unitary [Ca^{2+}] transient amplitudes should be a generalizable method provided the firing properties of the cells of interest are known from *in vivo* silicon probe or tetrode recordings, based on which one can calculate the ratio of temporally isolated single APs and bursts of APs. The key issue with both of our methods is to achieve a SNR in the *in vivo* recordings, which permits detection of single AP-evoked fluorescence transients. One solution might be to reduce the number simultaneously recorded nerve cells, resulting in a better SNR. My results support the necessity to obtain *in vivo* the full range of the critical parameters and to consider the variability of these when developing spike inferring algorithms.

DOI:10.14753/SE.2019.2319

7. CONCLUSION

In my dissertation I investigated the mechanism underlying distinct target cell-type dependent P_r and short-term plasticity. First, I determined the short-term plasticity of CA3 PC synapses contacting PV^+ and $mGluR1\alpha^+$ INs. My measurements of EPSCs, evoked by extracellular stimulation of CA3 PC axon collaterals demonstrated different (CA3 PC-to PV IN: depressing, CA3 PC-to mGlur1α IN: facilitating) short-term synaptic properties at these synapses, indicating a different initial release probability. I also found that the coexpression of Elfn1 in $mGlur1\alpha^+$ INs will likely impose facilitating short-term plasticity of CA3 PC-to-$mGlur1\alpha^+$ IN synapses. My results provided me the use of these molecules (PV and mGlur1α) in this brain region to label postsynaptic compartments of high, respectively low P_r synapses.

Next, my [Ca^{2+}] imaging experiments of CA3 PC local axon terminals showed that the [Ca^{2+}] influx upon a single AP is significantly larger in case of high P_r synapses. With the use of ω-CTX MVIIC, a selective N- and P/Q- type Ca^{2+} channel blocker I also provide evidence for a similar contribution of P/Q, N type Ca^{2+} channels to the [Ca^{2+}] influx in these two populations of synapses. Finally by repeating my [Ca^{2+}] imaging experiments with a lower concentration of the Ca^{2+} sensitive dye, I managed to demonstrate the lack of difference between decay time constants in the high, respectively low P_r bouton populations, indicating similar [Ca^{2+}] buffering in these two bouton populations.

These results, in concert with the parallel experiments of my colleagues showing a ~ twofold higher functional Ca^{2+} channel density in the AZs innervating PV^+ INs compared with those innervating $mGluR1\alpha^+$ ones, but only ~15% difference in the Ca^{2+} channel subunit density; provided evidence that a target cell-type different modulation of [Ca^{2+}] function or different subunit composition are the underlying causes of the different P_r at these synapses.

Distinct physiological properties and molecular compositions underlie the capability of the neuronal network to form diverse synaptic connections with distinct efficacy of information transfer. Investigating the role of the synaptic diversity in a behavioral context-dependent manner is hampered by the limitations of currently available large-scale recording techniques. Therefore, in the second part of my dissertation, I searched for the potential causes of these limitations in case of the most widespread, large-scale optical recording technique, Ca^{2+} imaging using GCaMP6f.

DOI:10.14753/SE.2019.2319

I demonstrate that the variability of peak amplitudes of GCaMP6f [Ca^{2+}] transients recorded *in vivo* is not only the consequence of variable activity, but is also due to a substantial cell-to-cell variability in the peak amplitude of unitary [Ca^{2+}] transients. Next, I offer evidence that the expression level of GCaMP6f is highly variable among CA1 PCs, and only partially underlies the variability in the amplitude of single AP-evoked Ca^{2+} transients recorded *in vitro*. Furthermore, I describe the phenomena of unitary Ca^{2+} transients amplitudes' dependence on the preceding firing history of the cell. I also show that GCaMP6f Ca^{2+} transients sum supralinearly and the supralinearity is frequency dependent and varies substantially form cell-to-cell. My parallel control experiments with a synthetic Ca^{2+} dye, that is known to report physiologically relevant [Ca^{2+}] linearly indicate that the observed variability and supralinearity are due to the intrinsic characteristics of GCaMP6f.

Our modelling study, performed with the help of my colleague, Miklós Szoboszlay, revealed that the main source of spike inference error is the variability in the peak amplitude, and not in the decay or supralinearity. Finally, I developed a model dependent and an independent procedure to estimate the peak amplitudes of unitary [Ca^{2+}] transients and I demonstrate reliable (mean ER ~5%) spike inference with MLspike using these unitary amplitude estimates in weakly GCaMP6f expressing.

DOI:10.14753/SE.2019.2319

8. SUMMARY

Target cell type-dependent differences in presynaptic release probability (P_r) are intriguing features of cortical microcircuits that increase the computational power of neuronal networks. The experiments of Rozov et al. (2001) indicated that differences in Ca^{2+} channel densities might be the underlying mechanism. My experiments indicate that the initial P_r of CA3 pyramidal cell synapses onto PV^+ or mGluR1α^+ INs is different; moreover the facilitating short-term properties of mGluR1α-dendrite targeting synapses is likely imposed by the co-expression of Elfn1 protein. My [Ca^{2+}] imaging experiments of CA3 PC local axon terminals revealed that the [Ca^{2+}] influx upon a single AP is significantly larger in case of high P_r synapses. This difference is not due to a differing contribution of P/Q, N type Ca^{2+} channels to the [Ca^{2+}] influx or to differnces in [Ca^{2+}] buffering. These results, in concert with those of Noémi Holderith, revealed a ~2 times higher functional Ca^{2+} channel density in high P_r synapses. However, the results of Tekla Kirizs demonstrated only 1.15 times larger Cav2.1 and Cav2.2 subunit densities using an independent anatomical method. This discrepancy indicates a target cell type-specific modulation of voltage-gated Ca^{2+} channel function or different subunit composition being the mechanisms underlying the functional differences (Éltes et al., 2017).

Investigating the role of such diversity of synaptic properties on network activity and behavior is hampered by inaccuracies of spike inference from fluorescent traces. Here I explored how the expression level of the most widely used genetically encoded Ca^{2+} indicator, GCaMP6f affects the amplitude, kinetics and temporal summation of [Ca^{2+}] transients in mouse hippocampal CA1 PCs. The amplitude of unitary [Ca^{2+}] transients negatively correlates with GCaMP6f expression, but displays large variability among PCs with similarly low expression levels. The summation of fluorescent signals is frequency dependent, supralinear and also shows remarkable cell-to-cell variability. Additionally, simulations performed with my colleague Miklós Szoboszlay, demonstrate that spike inference error rates (using MLspike; Deneux et al., 2016) strongly depend on unitary peak amplitudes and GCaMP6f expression levels. Finally, I provide an effective spike inference strategy that relies on the analysis of only weakly GCaMP6f expressing cells and on the estimation of the unitary [Ca^{2+}] transients in individual PCs (Éltes et al., 2019).

DOI:10.14753/SE.2019.2319

9. ÖSSZEFOLGALÓ

A transzmitter felszabadulási valószínűség (*Fv*) célsejt-specifikus különbségei az agykérgi hálózatok érdekes jellemzői. Rozov és mtsai. kísérletei arra utalnak, hogy ennek hátterében a Ca^{2+} csatornák sűrűségében lévő különbség állhat (Rozov et al., 2001). Tézisemben bizonyítékot szolgáltatok arra, hogy a kezdeti *Fv* a CA3 piramissejtek (PS) és PV^{+} vagy mGluR1α^{+} interneuronok közötti szinapszisokban eltérő. A CA3 PS axonvégződéseiben végzett [Ca^{2+}] méréseimből kiderült, hogy nagyobb mennyiségű [Ca^{2+}] áramlik be egyetlen akciós potenciál során a nagyobb *Fv* terminálisokba. Ez a különbség nem a P/Q, illetve N típusú Ca^{2+} csatornák, a [Ca^{2+}] beáramlásához való eltérő hozzájárulásából, illetve nem a különböző [Ca^{2+}] pufferelésből származik. Ezen eredményeim és Holderith Noémi axonterminális térfogat és aktív zóna terület mérései alapján kiszámoltuk a funkcionális Ca^{2+} csatorna sűrűséget, mely ~2x nagyobb a magas *Fv* szinapszisokban. Kirizs Tekla anatómiai kísérletei viszont jelentősen kisebb különbséget mutattak ki (~1,15). Az anatómiai és funkcionális denzitás közötti eltérés alapján a Ca^{2+} csatornák célsejt-specifikus funkcionális modulációja vagy különböző alegység-összetétele állhat a célsejt-specifikus *Fv* hátterében (Éltes et al., 2017).

A szinaptikus tulajdonságok sokféleségének a különböző viselkedési mintázatok kialakulására kifejtett hatásának feltárását az *in vivo* mért fluoreszcens jelek tüzelési mintázattá való visszafejtésének pontatlansága gátolja. Tézisem második felében ezen limitációk okát vizsgáltam a széleskörben használt genetikailag kódolt Ca^{2+} indikátor, a GCaMP6f esetén. Kísérleteim kimutatták, hogy az egységnyi [Ca^{2+}] tranziensek amplitúdója negatívan korrelál a GCaMP6f expresszió szintjével, de hasonlóan alacsony expressziós szintű PS-ek esetén nagy eltérést mutat. A fluoreszcens jelek összegzése frekvenciafüggő, szupralineáris, és jelentős sejtenkénti változékonyságot mutat. Szoboszlay Miklós kolegámmal végzett szimulációk alapján megállapítottuk, hogy a tüzelési mintázat visszafejtési hibarátája nagymértékben függ az egységnyi tranziens amplitudójában lévő változékonyságtól és a GCaMP6f expressziós szintjétől. Végezetül, egy olyan, eddigieknél hatékonyabb visszafejtési stratégiát mutattam be, amely a gyenge GCaMP6f expressziós szintű sejtek analízisén és az egységnyi [Ca^{2+}] tranziensek amplitudójának becslésén alapszik (Éltes et al., 2019).

10. BIBLIOGRAPHY

Akerboom J et al. (2012) Optimization of a GCaMP calcium indicator for neural activity imaging. J Neurosci 32:13819–13840.

Akerboom J, Rivera JDV, Guilbe MMR, Malavé ECA, Hernandez HH, Tian L, Hires SA, Marvin JS, Looger LL, Schreiter ER (2009) Crystal structures of the GCaMP calcium sensor reveal the mechanism of fluorescence signal change and aid rational design. J Biol Chem 284:6455–6464.

Akert K, Pfenninger K, Sandri C, Moor H (1972) Freeze-etching and cytochemistry of vesicles and membrane complexes in synapses of the C.N.S. In: In Structure and Function of Synapses (Purpura GDP and DP, ed), pp 67–86. New York: Raven Press.

Ali AB, Deuchars J, Pawelzik H, Thomson AM (1998) CA1 pyramidal to basket and bistratified cell EPSPs: dual intracellular recordings in rat hippocampal slices. J Physiol 507:201–217.

Ali AB, Thomson AM (1998) Facilitating pyramid to horizontal oriens-alveus interneurone inputs: dual intracellular recordings in slices of rat hippocampus. J Physiol 507:185–199.

Althof D, Baehrens D, Watanabe M, Suzuki N, Fakler B, Kulik Á (2015) Inhibitory and excitatory axon terminals share a common nano-architecture of their Cav2.1 (P/Q-type) Ca(2+) channels. Front Cell Neurosci 9:315.

Ambrose RE, Pfeiffer BE, Foster DJ (2016) Reverse Replay of Hippocampal Place Cells Is Uniquely Modulated by Changing Reward. Neuron 91:1124–1136.

Andersen P, Morris R, Amaral D, Bliss T, O'Keefe J (2007) The Hippocampus Book. Oxford University Press. 3-128.

Anderson GR, Aoto J, Tabuchi K, Földy C, Covy J, Yee AX, Wu D, Lee S-J, Chen L, Malenka RC, Südhof TC (2015) β-Neurexins Control Neural Circuits by Regulating Synaptic Endocannabinoid Signaling. Cell 162:593–606.

Aronov D, Nevers R, Tank DW (2017) Mapping of a non-spatial dimension by the hippocampal-entorhinal circuit. Nature 543:719–722.

Arriaga M, Han EB (2017) Dedicated Hippocampal Inhibitory Networks for Locomotion and Immobility. J Neurosci 37:9222–9238.

Atwood HL, Karunanithi S (2002) Diversification of synaptic strength: presynaptic elements. Nat Rev Neurosci 3:497–516.

Badura A, Sun XR, Giovannucci A, Lynch LA, Wang SS-H (2014) Fast calcium sensor proteins for monitoring neural activity. Neurophotonics 1:025008.

Baimbridge KG, Peet MJ, McLennan H, Church J (1991) Bursting response to current-evoked depolarization in rat CA1 pyramidal neurons is correlated with lucifer yellow dye coupling but not with the presence of calbindin-D28k. Synapse 7:269–277.

Bannister NJ, Larkman AU (1995) Dendritic morphology of CA1 pyramidal neurones from the rat hippocampus: I. Branching patterns. J Comp Neurol 360:150–160.

Basu J, Siegelbaum SA (2015) The Corticohippocampal Circuit, Synaptic Plasticity, and Memory. Cold Spring Harb Perspect Biol 7:1506–1510.

Bean BP (1989) Neurotransmitter inhibition of neuronal calcium currents by changes in channel voltage dependence. Nature 340:153–156.

Bennett MK, Calakos N, Scheller RH (1992) Syntaxin: a synaptic protein implicated in docking of synaptic vesicles at presynaptic active zones. Science 257:255–259.

Berridge MJ, Lipp P, Bootman MD (2000) The versatility and universality of calcium signalling. Nat Rev Mol Cell Biol 1:11–21.

Biró AA, Holderith NB, Nusser Z (2005) Quantal size is independent of the release probability at hippocampal excitatory synapses. J Neurosci 25:223–232.

Blackman A V., Abrahamsson T, Costa RP, Lalanne T, Sjöström PJ (2013) Target-cell-specific short-term plasticity in local circuits. Front Synaptic Neurosci 5:1–13.

Böhme MA, Beis C, Reddy-Alla S, Reynolds E, Mampell MM, Grasskamp AT, Lützkendorf J, Bergeron DD, Driller JH, Babikir H, Göttfert F, Robinson IM, O'Kane CJ, Hell SW, Wahl MC, Stelzl U, Loll B, Walter AM, Sigrist SJ (2016) Active zone scaffolds differentially accumulate Unc13 isoforms to tune Ca(2+) channel-vesicle coupling. Nat Neurosci 19:1311–1320.

Borst JG, Sakmann B (1996) Calcium influx and transmitter release in a fast CNS synapse. Nature 383:431–434.

Branco T, Staras K (2009) The probability of neurotransmitter release: variability and feedback control at single synapses. Nat Rev Neurosci 10:373–383.

Broussard GJ, Liang R, Tian L (2014) Monitoring activity in neural circuits with genetically encoded indicators. Front Mol Neurosci 7:97.

Brown SP, Safo PK, Regehr WG (2004) Endocannabinoids inhibit transmission at granule cell to Purkinje cell synapses by modulating three types of presynaptic calcium channels. J Neurosci 24:5623–5631.

Buchanan KA, Blackman A V., Moreau AW, Elgar D, Costa RP, Lalanne T, Tudor Jones AA, Oyrer J, Sjöström PJ (2012) Target-specific expression of presynaptic NMDA receptors in neocortical microcircuits. Neuron 75:451–466.

Buraei Z, Yang J (2010) The ß subunit of voltage-gated Ca2+ channels. Physiol Rev 90:1461–1506.

Buzsáki G (2004) Large-scale recording of neuronal ensembles. Nat Neurosci 7:446–451.

Buzsáki G, Chrobak JJ (1995) Temporal structure in spatially organized neuronal ensembles: a role for interneuronal networks. Curr Opin Neurobiol 5:504–510.

Calloway N, Gouzer G, Xue M, Ryan TA (2015) The active-zone protein Munc13 controls the use-dependence of presynaptic voltage-gated calcium channels. Elife 4:e07728.

Carbone E, Calorio C, Vandael DHF (2014) T-type channel-mediated neurotransmitter release. Pflugers Arch 466:677–687.

Cembrowski MS, Bachman JL, Wang L, Sugino K, Shields BC, Spruston N (2016) Spatial Gene-Expression Gradients Underlie Prominent Heterogeneity of CA1 Pyramidal Neurons. Neuron 89:351–368.

Chen T-W, Wardill TJ, Sun Y, Pulver SR, Renninger SL, Baohan A, Schreiter ER, Kerr RA, Orger MB, Jayaraman V, Looger LL, Svoboda K, Kim DS (2013) Ultrasensitive fluorescent proteins for imaging neuronal activity. Nature 499:295–300.

Chevaleyre V, Siegelbaum SA (2010) Strong CA2 pyramidal neuron synapses define a powerful disynaptic cortico-hippocampal loop. Neuron 66:560–572.

Cui Z, Gerfen CR, Young WS (2013) Hypothalamic and other connections with dorsal CA2 area of the mouse hippocampus. J Comp Neurol 521:1844–1866.

Dana H, Chen T-W, Hu A, Shields BC, Guo C, Looger LL, Kim DS, Svoboda K (2014) Thy1-GCaMP6 transgenic mice for neuronal population imaging in vivo. PLoS One 9:e108697.

Dana H, Mohar B, Sun Y, Narayan S, Gordus A, Hasseman JP, Tsegaye G, Holt GT, Hu A, Walpita D, Patel R, Macklin JJ, Bargmann CI, Ahrens MB, Schreiter ER, Jayaraman V, Looger LL, Svoboda K, Kim DS (2016) Sensitive red protein calcium indicators for imaging neural activity. Elife 5:1–24.

Danielson NB, Zaremba JD, Kaifosh P, Bowler J, Ladow M, Losonczy A (2016) Sublayer-Specific Coding Dynamics during Spatial Navigation and Learning in Hippocampal Area CA1. Neuron 91:652–665.

De Chaumont F, Dallongeville S, Chenouard N, Hervé N, Pop S, Provoost T, Meas-Yedid V, Pankajakshan P, Lecomte T, Le Montagner Y, Lagache T, Dufour A, Olivo-Marin JC (2012) Icy: An open bioimage informatics platform for extended reproducible research. Nat Methods 9:690–696.

Del Castillo J, Katz B (1954) Quantal components of the end-plate potential. J Physiol 124:560–573.

Deneux T, Kaszas A, Szalay G, Katona G, Lakner T, Grinvald A, Rózsa B, Vanzetta I (2016) Accurate spike estimation from noisy calcium signals for ultrafast three-dimensional imaging of large neuronal populations in vivo. Nat Commun 7:12190.

Denk W, Strickler JH, Webb WW (1990) Two-photon laser scanning fluorescence microscopy. Science 248:73–76.

Dittman JS, Regehr WG (1996) Contributions of calcium-dependent and calcium-independent mechanisms to presynaptic inhibition at a cerebellar synapse. J Neurosci 16:1623–1633.

Dodge FA, Rahamimoff R (1967) Co-operative action a calcium ions in transmitter release at the neuromuscular junction. J Physiol 193:419–432.

Dombeck DA, Harvey CD, Tian L, Looger LL, Tank DW (2010) Functional imaging of hippocampal place cells at cellular resolution during virtual navigation. Nat Neurosci 13:1433–1440.

Du J, Zhang L, Weiser M, Rudy B, McBain CJ (1996) Developmental expression and functional characterization of the potassium-channel subunit Kv3.1b in parvalbumin-containing interneurons of the rat hippocampus. J Neurosci 16:506–518.

Dulubova I, Sugita S, Hill S, Hosaka M, Fernandez I, Südhof TC, Rizo J (1999) A

conformational switch in syntaxin during exocytosis: role of munc18. EMBO J 18:4372–4382.

Eggermann E, Bucurenciu I, Goswami SP, Jonas P (2011) Nanodomain coupling between Ca^{2+} channels and sensors of exocytosis at fast mammalian synapses. Nat Rev Neurosci 13:7–21.

Éltes T, Kirizs T, Nusser Z, Holderith N (2017) Target Cell Type-Dependent Differences in Ca2+ Channel Function Underlie Distinct Release Probabilities at Hippocampal Glutamatergic Terminals. J Neurosci 37:1910–1924.

Éltes T, Szoboszlay M, Kerti-Szigeti K, Nusser Z (2019) Improved spike inference accuracy by estimating the peak amplitude of unitary [Ca 2+] transients in weakly GCaMP6f expressing hippocampal pyramidal cells. J Physiol:JP277681.

Fuentealba P, Begum R, Capogna M, Jinno S, Márton LF, Csicsvari J, Thomson A, Somogyi P, Klausberger T (2008) Ivy cells: a population of nitric-oxide-producing, slow-spiking GABAergic neurons and their involvement in hippocampal network activity. Neuron 57:917–929.

Geiger JR, Jonas P (2000) Dynamic control of presynaptic Ca(2+) inflow by fast-inactivating K(+) channels in hippocampal mossy fiber boutons. Neuron 28:927–939.

Geiller T, Fattahi M, Choi J-S, Royer S (2017) Place cells are more strongly tied to landmarks in deep than in superficial CA1. Nat Commun 8:14531.

Goda Y, Südhof TC (1997) Calcium regulation of neurotransmitter release: reliably unreliable? Curr Opin Cell Biol 9:513–518.

Gray EG (1963) Electron microscopy of presynaptic organelles of the spinal cord. J Anat 97:101–106.

Green JD (1964) The Hippocampus. Physiol Rev 44:561–608.

Greenberg DS, Houweling AR, Kerr JND (2008) Population imaging of ongoing neuronal activity in the visual cortex of awake rats. Nat Neurosci 11:749–751.

Greenberg DS, Wallace DJ, Voit K-M, Wuertenberger S, Czubayko U, Monsees A, Handa T, Vogelstein JT, Seifert R, Groemping Y, Kerr JN (2018) Accurate action potential inference from a calcium sensor protein through biophysical modeling. bioRxiv:479055.

Grewe BF, Langer D, Kasper H, Kampa BM, Helmchen F (2010) High-speed in vivo calcium imaging reveals neuronal network activity with near-millisecond precision. Nat Methods 7:399–405.

Grienberger C, Konnerth A (2012) Imaging calcium in neurons. Neuron 73:862–885.

Grosmark AD, Buzsáki G (2016) Diversity in neural firing dynamics supports both rigid and learned hippocampal sequences. Science 351:1440–1443.

Hargreaves EL, Rao G, Lee I, Knierim JJ (2005) Major dissociation between medial and lateral entorhinal input to dorsal hippocampus. Science 308:1792–1794.

Hata Y, Slaughter CA, Südhof TC (1993) Synaptic vesicle fusion complex contains unc-18 homologue bound to syntaxin. Nature 366:347–351.

Helmchen F, Denk W (2005) Deep tissue two-photon microscopy. Nat Methods 2:932–940.

Hires SA, Tian L, Looger LL (2008) Reporting neural activity with genetically encoded calcium indicators. Brain Cell Biol 36:69–86.

Hitti FL, Siegelbaum SA (2014) The hippocampal CA2 region is essential for social memory. Nature 508:88–92.

Holderith N, Lorincz A, Katona G, Rózsa B, Kulik A, Watanabe M, Nusser Z (2012) Release probability of hippocampal glutamatergic terminals scales with the size of the active zone. Nat Neurosci 15:988–997.

Holtmaat A, Caroni P (2016) Functional and structural underpinnings of neuronal assembly formation in learning. Nat Neurosci 19:1553–1562.

Igarashi KM, Ito HT, Moser EI, Moser M-B (2014) Functional diversity along the transverse axis of hippocampal area CA1. FEBS Lett 588:2470–2476.

Isaacson JS, Scanziani M (2011) How inhibition shapes cortical activity. Neuron 72:231–243.

Ishiyama S, Schmidt H, Cooper BH, Brose N, Eilers J (2014) Munc13-3 superprimes synaptic vesicles at granule cell-to-basket cell synapses in the mouse cerebellum. J Neurosci 34:14687–14696.

Jackman SL, Turecek J, Belinsky JE, Regehr WG (2016) The calcium sensor synaptotagmin 7 is required for synaptic facilitation. Nature 529:88–91.

Jercog P, Rogerson T, Schnitzer MJ (2016) Large-Scale Fluorescence Calcium-Imaging

Methods for Studies of Long-Term Memory in Behaving Mammals. Cold Spring Harb Perspect Biol 8:a021824.

Jinno S, Klausberger T, Marton LF, Dalezios Y, Roberts JDB, Fuentealba P, Bushong EA, Henze D, Buzsáki G, Somogyi P (2007) Neuronal diversity in GABAergic long-range projections from the hippocampus. J Neurosci 27:8790–8804.

Jung MW, Wiener SI, McNaughton BL (1994) Comparison of spatial firing characteristics of units in dorsal and ventral hippocampus of the rat. J Neurosci 14:7347–7356.

Kaeser PS, Deng L, Wang Y, Dulubova I, Liu X, Rizo J, Südhof TC (2011) RIM proteins tether Ca2+ channels to presynaptic active zones via a direct PDZ-domain interaction. Cell 144:282–295.

Kandel ER, Schwartz JH, Jessell TM, Siegelbaum SA, Hudspeth AJ (2013) Principles of Neural Science. :71–307.

Katz B, Miledi R (1967) A study of synaptic transmission in the absence of nerve impulses. J Physiol 192:407–436.

Katz PS, Kirk MD, Govind CK (1993) Facilitation and depression at different branches of the same motor axon: evidence for presynaptic differences in release. J Neurosci 13:3075–3089.

Kepecs A, Fishell G (2014) Interneuron cell types are fit to function. Nature 505:318–326.

Khvotchev M, Dulubova I, Sun J, Dai H, Rizo J, Südhof TC (2007) Dual modes of Munc18-1/SNARE interactions are coupled by functionally critical binding to syntaxin-1 N terminus. J Neurosci 27:12147–12155.

Kim SH, Ryan TA (2013) Balance of calcineurin Aα and CDK5 activities sets release probability at nerve terminals. J Neurosci 33:8937–8950.

Kitamura T, Pignatelli M, Suh J, Kohara K, Yoshiki A, Abe K, Tonegawa S (2014) Island cells control temporal association memory. Science 343:896–901.

Klausberger T, Somogyi P (2008) Neuronal diversity and temporal dynamics: The unity of hippocampal circuit operations. Science (80-) 321:53–57.

Knierim JJ, Neunuebel JP, Deshmukh SS (2014) Functional correlates of the lateral and medial entorhinal cortex: objects, path integration and local-global reference frames. Philos Trans R Soc Lond B Biol Sci 369:20130369.

Knöpfel T, Gallero-Salas Y, Song C (2015) Genetically encoded voltage indicators for large scale cortical imaging come of age. Curr Opin Chem Biol 27:75–83.

Koester HJ, Johnston D (2005) Target cell-dependent normalization of transmitter release at neocortical synapses. Science 308:863–866.

Kohara K, Pignatelli M, Rivest AJ, Jung H-Y, Kitamura T, Suh J, Frank D, Kajikawa K, Mise N, Obata Y, Wickersham IR, Tonegawa S (2014) Cell type-specific genetic and optogenetic tools reveal hippocampal CA2 circuits. Nat Neurosci 17:269–279.

Körber C, Horstmann H, Venkataramani V, Herrmannsdörfer F, Kremer T, Kaiser M, Schwenger DB, Ahmed S, Dean C, Dresbach T, Kuner T (2015) Modulation of Presynaptic Release Probability by the Vertebrate-Specific Protein Mover. Neuron 87:521–533.

Kraus BJ, Robinson RJ, White JA, Eichenbaum H, Hasselmo ME (2013) Hippocampal "time cells": time versus path integration. Neuron 78:1090–1101.

Kulik A, Nakadate K, Hagiwara A, Fukazawa Y, Luján R, Saito H, Suzuki N, Futatsugi A, Mikoshiba K, Frotscher M, Shigemoto R (2004) Immunocytochemical localization of the alpha 1A subunit of the P/Q-type calcium channel in the rat cerebellum. Eur J Neurosci 19:2169–2178.

Kupferschmidt DA, Lovinger DM (2015) Inhibition of presynaptic calcium transients in cortical inputs to the dorsolateral striatum by metabotropic GABA(B) and mGlu2/3 receptors. J Physiol 593:2295–2310.

Kusch V, Bornschein G, Loreth D, Bank J, Jordan J, Baur D, Watanabe M, Kulik A, Heckmann M, Eilers J, Schmidt H (2018) Munc13-3 Is Required for the Developmental Localization of Ca2+Channels to Active Zones and the Nanopositioning of Cav2.1 Near Release Sensors. Cell Rep 22:2094–2106.

Leão RM, Von Gersdorff H (2002) Noradrenaline increases high-frequency firing at the calyx of Held synapse during development by inhibiting glutamate release. J Neurophysiol 87:2297–2306.

Lee S-H, Marchionni I, Bezaire M, Varga C, Danielson N, Lovett-Barron M, Losonczy A, Soltesz I (2014) Parvalbumin-positive basket cells differentiate among hippocampal pyramidal cells. Neuron 82:1129–1144.

Lenkey N, Kirizs T, Holderith N, Máté Z, Szabó G, Vizi ES, Hájos N, Nusser Z (2015) Tonic endocannabinoid-mediated modulation of GABA release is independent of the CB1 content of axon terminals. Nat Commun 6:6557.

Li C, Ullrich B, Zhang JZ, Anderson RGW, Brose N, Südhof TC (1995) Ca(2+)-dependent and -independent activities of neural and non-neural synaptotagmins. Nature 375:594–599.

Lin MZ, Schnitzer MJ (2016) Genetically encoded indicators of neuronal activity. Nat Neurosci 19:1142–1153.

Losonczy A, Somogyi P, Nusser Z (2003) Reduction of excitatory postsynaptic responses by persistently active metabotropic glutamate receptors in the hippocampus. J Neurophysiol 89:1910–1919.

Losonczy A, Zhang L, Shigemoto R, Somogyi P, Nusser Z (2002) Cell type dependence and variability in the short-term plasticity of EPSCs in identified mouse hippocampal interneurones. J Physiol 542:193–210.

Lütcke H, Gerhard F, Zenke F, Gerstner W, Helmchen F (2013) Inference of neuronal network spike dynamics and topology from calcium imaging data. Front Neural Circuits 7:201.

MacDonald CJ, Carrow S, Place R, Eichenbaum H (2013) Distinct hippocampal time cell sequences represent odor memories in immobilized rats. J Neurosci 33:14607–14616.

Mao T, O'Connor DH, Scheuss V, Nakai J, Svoboda K (2008) Characterization and subcellular targeting of GCaMP-type genetically-encoded calcium indicators. PLoS One 3:e1796.

Markram H, Gupta A, Uziel A, Wang Y, Tsodyks M (1998a) Information processing with frequency-dependent synaptic connections. Neurobiol Learn Mem 70:101–112.

Markram H, Wang Y, Tsodyks M (1998b) Differential signaling via the same axon of neocortical pyramidal neurons. Proc Natl Acad Sci U S A 95:5323–5328.

Maximov A, Tang J, Yang X, Pang ZP, Südhof TC (2009) Complexin controls the force transfer from SNARE complexes to membranes in fusion. Science 323:516–521.

McMahon HT, Missler M, Li C, Südhof TC (1995) Complexins: cytosolic proteins that regulate SNAP receptor function. Cell 83:111–119.

Melzer S, Michael M, Caputi A, Eliava M, Fuchs EC, Whittington MA, Monyer H (2012) Long-range-projecting GABAergic neurons modulate inhibition in hippocampus and entorhinal cortex. Science 335:1506–1510.

Mercer A, Eastlake K, Trigg HL, Thomson AM (2012) Local circuitry involving parvalbumin-positive basket cells in the CA2 region of the hippocampus. Hippocampus 22:43–56.

Mizuseki K, Diba K, Pastalkova E, Buzsáki G (2011) Hippocampal CA1 pyramidal cells form functionally distinct sublayers. Nat Neurosci 14:1174–1181.

Nakai J, Ohkura M, Imoto K (2001) A high signal-to-noise Ca(2+) probe composed of a single green fluorescent protein. Nat Biotechnol 19:137–141.

Nakamura Y, Harada H, Kamasawa N, Matsui K, Rothman JS, Shigemoto R, Silver RA, DiGregorio DA, Takahashi T (2015) Nanoscale distribution of presynaptic Ca(2+) channels and its impact on vesicular release during development. Neuron 85:145–158.

Neher E (1998) Vesicle pools and Ca2+ microdomains: new tools for understanding their roles in neurotransmitter release. Neuron 20:389–399.

Nusser Z (2018) Creating diverse synapses from the same molecules. Curr Opin Neurobiol 51:8–15.

O'Keefe J, Dostrovsky J (1971) The hippocampus as a spatial map. Preliminary evidence from unit activity in the freely-moving rat. Brain Res 34:171–175.

Ohkura M, Sasaki T, Sadakari J, Gengyo-Ando K, Kagawa-Nagamura Y, Kobayashi C, Ikegaya Y, Nakai J (2012) Genetically encoded green fluorescent Ca2+ indicators with improved detectability for neuronal Ca2+ signals. PLoS One 7:e51286.

Omer DB, Maimon SR, Las L, Ulanovsky N (2018) Social place-cells in the bat hippocampus. Science 359:218–224.

Oñativia J, Schultz SR, Dragotti PL (2013) A finite rate of innovation algorithm for fast and accurate spike detection from two-photon calcium imaging. J Neural Eng 10:046017.

Pachitariu M, Stringer C, Harris KD (2018) Robustness of Spike Deconvolution for Neuronal Calcium Imaging. J Neurosci 38:7976–7985.

Palay SL, Palade GE (1955) The fine structure of neurons. J Biophys Biochem Cytol 1:69–88.

Parajuli LK, Nakajima C, Kulik A, Matsui K, Schneider T, Shigemoto R, Fukazawa Y (2012) Quantitative regional and ultrastructural localization of the Ca(v)2.3 subunit of R-type calcium channel in mouse brain. J Neurosci 32:13555–13567.

Park IJ, Bobkov Y V., Ache BW, Principe JC (2013) Quantifying bursting neuron activity from calcium signals using blind deconvolution. J Neurosci Methods 218:196–205.

Parnas I (1972) Differential block at high frequency of branches of a single axon innervating two muscles. J Neurophysiol 35:903–914.

Pastalkova E, Itskov V, Amarasingham A, Buzsáki G (2008) Internally generated cell assembly sequences in the rat hippocampus. Science 321:1322–1327.

Pfenninger K, Akert K, Moor H, Sandri C (1972) The fine structure of freeze-fractured presynaptic membranes. J Neurocytol 1:129–149.

Pnevmatikakis EA, Soudry D, Gao Y, Machado TA, Merel J, Pfau D, Reardon T, Mu Y, Lacefield C, Yang W, Ahrens M, Bruno R, Jessell TM, Peterka DS, Yuste R, Paninski L (2016) Simultaneous Denoising, Deconvolution, and Demixing of Calcium Imaging Data. Neuron 89:285–299.

Podor B, Hu Y, Ohkura M, Nakai J, Croll R, Fine A (2015) Comparison of genetically encoded calcium indicators for monitoring action potentials in mammalian brain by two-photon excitation fluorescence microscopy. Neurophotonics 2:021014.

Pouille F, Scanziani M (2004) Routing of spike series by dynamic circuits in the hippocampus. Nature 429:717–723.

Reyes A, Lujan R, Rozov A, Burnashev N, Somogyi P, Sakmann B (1998) Target-cell-specific facilitation and depression in neocortical circuits. Nat Neurosci 1:279–285.

Robitaille R, Tremblay JP (1987) Non-uniform release at the frog neuromuscular junction: evidence of morphological and physiological plasticity. Brain Res 434:95–116.

Rose T, Goltstein PM, Portugues R, Griesbeck O (2014) Putting a finishing touch on GECIs. Front Mol Neurosci 7:88.

Rowan MJM, Tranquil E, Christie JM (2014) Distinct Kv channel subtypes contribute to differences in spike signaling properties in the axon initial segment and presynaptic boutons of cerebellar interneurons. J Neurosci 34:6611–6623.

Rozov A, Burnashev N, Sakmann B, Neher E (2001) Transmitter release modulation by

intracellular Ca2+ buffers in facilitating and depressing nerve terminals of pyramidal cells in layer 2/3 of the rat neocortex indicates a target cell-specific difference in presynaptic calcium dynamics. J Physiol 531:807–826.

Sabatini BL, Regehr WG (1999) Timing of synaptic transmission. Annu Rev Physiol 61:521–542.

Sasaki T, Takahashi N, Matsuki N, Ikegaya Y (2008) Fast and accurate detection of action potentials from somatic calcium fluctuations. J Neurophysiol 100:1668–1676.

Scanziani M, Gähwiler BH, Charpak S (1998) Target cell-specific modulation of transmitter release at terminals from a single axon. Proc Natl Acad Sci U S A 95:12004–12009.

Schlüter OM, Basu J, Südhof TC, Rosenmund C (2006) Rab3 superprimes synaptic vesicles for release: implications for short-term synaptic plasticity. J Neurosci 26:1239–1246.

Schlüter OM, Schmitz F, Jahn R, Rosenmund C, Südhof TC (2004) A complete genetic analysis of neuronal Rab3 function. J Neurosci 24:6629–6637.

Schneggenburger R, Han Y, Kochubey O (2012) Ca(2+) channels and transmitter release at the active zone. Cell Calcium 52:199–207.

Schwaller B (2010) Cytosolic Ca2+ buffers. Cold Spring Harb Perspect Biol 2:a004051.

Scoville WB, Milner B (1957) Loss of recent memory after bilateral hippocampal lesions. J Neurol Neurosurg Psychiatry 20:11–21.

Shigemoto R, Kulik A, Roberts JD, Ohishi H, Nusser Z, Kaneko T, Somogyi P (1996) Target-cell-specific concentration of a metabotropic glutamate receptor in the presynaptic active zone. Nature 381:523–525.

Söllner T, Bennett MK, Whiteheart SW, Scheller RH, Rothman JE (1993a) A protein assembly-disassembly pathway in vitro that may correspond to sequential steps of synaptic vesicle docking, activation, and fusion. Cell 75:409–418.

Söllner T, Whiteheart SW, Brunner M, Erdjument-Bromage H, Geromanos S, Tempst P, Rothman JE (1993b) SNAP receptors implicated in vesicle targeting and fusion. Nature 362:318–324.

Soltesz I, Losonczy A (2018) CA1 pyramidal cell diversity enabling parallel information processing in the hippocampus. Nat Neurosci 21:484–493.

Somogyi P (2010) Hippocampus – intrinsic organisation. In: Handbook of Brain

Microcircuits (Gordon M. Shepherd SG, ed), pp 148–164. Oxford: Oxford University Press.

Somogyi P, Katona L, Klausberger T, Lasztóczi B, Viney TJ (2014) Temporal redistribution of inhibition over neuronal subcellular domains underlies state-dependent rhythmic change of excitability in the hippocampus. Philos Trans R Soc Lond B Biol Sci 369:20120518.

Strange BA, Witter MP, Lein ES, Moser EI (2014) Functional organization of the hippocampal longitudinal axis. Nat Rev Neurosci 15:655–669.

Su SC, Seo J, Pan JQ, Samuels BA, Rudenko A, Ericsson M, Neve RL, Yue DT, Tsai L-H (2012) Regulation of N-type voltage-gated calcium channels and presynaptic function by cyclin-dependent kinase 5. Neuron 75:675–687.

Sudhof TC (2004) The synaptic vesicle cycle. Annu Rev Neurosci 27:509–547.

Südhof TC (2012a) The presynaptic active zone. Neuron 75:11–25.

Südhof TC (2012b) Calcium control of neurotransmitter release. Cold Spring Harb Perspect Biol 4:a011353.

Südhof TC (2013a) Neurotransmitter release: the last millisecond in the life of a synaptic vesicle. Neuron 80:675–690.

Südhof TC (2013b) A molecular machine for neurotransmitter release: synaptotagmin and beyond. Nat Med 19:1227–1231.

Svoboda K, Yasuda R (2006) Principles of two-photon excitation microscopy and its applications to neuroscience. Neuron 50:823–839.

Sylwestrak EL, Ghosh A (2012) Elfn1 regulates target-specific release probability at CA1-interneuron synapses. Science 338:536–540.

Szabó GG, Lenkey N, Holderith N, Andrási T, Nusser Z, Hájos N (2014) Presynaptic calcium channel inhibition underlies CB1 cannabinoid receptor-mediated suppression of GABA release. J Neurosci 34:7958–7963.

Takahashi T, Forsythe ID, Tsujimoto T, Barnes-Davies M, Onodera K (1996) Presynaptic calcium current modulation by a metabotropic glutamate receptor. Science 274:594–597.

Theis L, Berens P, Froudarakis E, Reimer J, Román Rosón M, Baden T, Euler T, Tolias AS,

Bethge M (2016) Benchmarking Spike Rate Inference in Population Calcium Imaging. Neuron 90:471–482.

Thestrup T et al. (2014) Optimized ratiometric calcium sensors for functional in vivo imaging of neurons and T lymphocytes. Nat Methods 11:175–182.

Thomson AM (1997) Activity-dependent properties of synaptic transmission at two classes of connections made by rat neocortical pyramidal axons in vitro. J Physiol 502 (Pt 1:131–147.

Tian L, Hires SA, Mao T, Huber D, Chiappe ME, Chalasani SH, Petreanu L, Akerboom J, McKinney SA, Schreiter ER, Bargmann CI, Jayaraman V, Svoboda K, Looger LL (2009) Imaging neural activity in worms, flies and mice with improved GCaMP calcium indicators. Nat Methods 6:875–881.

Tomioka NH, Yasuda H, Miyamoto H, Hatayama M, Morimura N, Matsumoto Y, Suzuki T, Odagawa M, Odaka YS, Iwayama Y, Won Um J, Ko J, Inoue Y, Kaneko S, Hirose S, Yamada K, Yoshikawa T, Yamakawa K, Aruga J (2014) Elfn1 recruits presynaptic mGluR7 in trans and its loss results in seizures. Nat Commun 5:4501.

Unal G, Crump MG, Viney TJ, Éltes T, Katona L, Klausberger T, Somogyi P (2018) Spatio-temporal specialization of GABAergic septo-hippocampal neurons for rhythmic network activity. Brain Struct Funct 223:2409–2432.

Valero M, Cid E, Averkin RG, Aguilar J, Sanchez-Aguilera A, Viney TJ, Gomez-Dominguez D, Bellistri E, de la Prida LM (2015) Determinants of different deep and superficial CA1 pyramidal cell dynamics during sharp-wave ripples. Nat Neurosci 18:1281–1290.

Vogelstein JT, Watson BO, Packer AM, Yuste R, Jedynak B, Paninski L (2009) Spike inference from calcium imaging using sequential Monte Carlo methods. Biophys J 97:636–655.

Wallace DJ, Meyer zum Alten Borgloh S, Astori S, Yang Y, Bausen M, Kügler S, Palmer AE, Tsien RY, Sprengel R, Kerr JND, Denk W, Hasan MT (2008) Single-spike detection in vitro and in vivo with a genetic Ca2+ sensor. Nat Methods 5:797–804.

Wang Y, Okamoto M, Schmitz F, Hofmann K, Südhof TC (1997) Rim is a putative rab3 effector in regulating synaptic-vesicle fusion. Nature 388:593–598.

Wilt BA, Fitzgerald JE, Schnitzer MJ (2013) Photon shot noise limits on optical detection of

neuronal spikes and estimation of spike timing. Biophys J 104:51–62.

Yaksi E, Friedrich RW (2006) Reconstruction of firing rate changes across neuronal populations by temporally deconvolved Ca2+ imaging. Nat Methods 3:377–383.

Yang Y, Liu N, He Y, Liu Y, Ge L, Zou L, Song S, Xiong W, Liu X (2018) Improved calcium sensor GCaMP-X overcomes the calcium channel perturbations induced by the calmodulin in GCaMP. Nat Commun 9.

Zhang S-J, Ye J, Miao C, Tsao A, Cerniauskas I, Ledergerber D, Moser M-B, Moser EI (2013) Optogenetic dissection of entorhinal-hippocampal functional connectivity. Science 340:1232627.

Zhao Y, Araki S, Wu J, Teramoto T, Chang Y-F, Nakano M, Abdelfattah AS, Fujiwara M, Ishihara T, Nagai T, Campbell RE (2011) An expanded palette of genetically encoded Ca^{2+} indicators. Science 333:1888–1891.

Zheng K, Bard L, Reynolds JP, King C, Jensen TP, Gourine A V, Rusakov DA (2015) Time-Resolved Imaging Reveals Heterogeneous Landscapes of Nanomolar Ca(2+) in Neurons and Astroglia. Neuron 88:277–288.

Zhong H, Yokoyama CT, Scheuer T, Catterall WA (1999) Reciprocal regulation of P/Q-type Ca2+ channels by SNAP-25, syntaxin and synaptotagmin. Nat Neurosci 2:939–941.

Zhou P, Pang ZP, Yang X, Zhang Y, Rosenmund C, Bacaj T, Südhof TC (2013) Syntaxin-1 N-peptide and Habc-domain perform distinct essential functions in synaptic vesicle fusion. EMBO J 32:159–171.

DOI:10.14753/SE.2019.2319

11. LIST OF OWN PUBLICATIONS

11.1. Publications that formed the basis of the dissertation:

1. **Éltes T***, Kirizs T*, Nusser Z, Holderith N. (2017) Target cell type-dependent differences in Ca^{2+} channel function underlie distinct release probabilities at hippocampal glutamatergic terminals. Journal of Neuroscience, 37: 1910–19242. IF: 5.971.

2. **Éltes T,** Szoboszlay M, Kerti-Szigeti K, Nusser Z. (2019): Improved spike inference accuracy by estimating the peak amplitude of unitary [Ca^{2+}] transients in weakly GCaMP6f expressing hippocampal CA1 pyramidal cells. The Journal of Physiology, J Physiol. 2019 Jun;597(11):2925-2947, IF:4.540.

11.2. Other publications:

1. Unal G, Crump MG, Viney TJ, **Éltes T**, Katona L, Klausberger T, Somogyi P. (2018) Spatio-temporal specialization of GABAergic septo-hippocampal neurons for rhythmic network activity, Brain Structure and Function, doi: 10.1007/s00429-018-1626-0; IF: 4.231.

2. Orbán-Kis K, **Szabadi T**, Szilágyi T. (2015) The loss of Ivy cells and the hippocampal input modulatory O-LM cells contribute to the emergence of hyperexcitability in the hippocampus, Rom J Morphol Embryol, 56(1):155–161; IF: 0.811.

*: co-first authors

DOI:10.14753/SE.2019.2319

12. ACKNOWLEDGMENTS

I would like to thank my supervisor, Prof. Zoltán Nusser for the opportunity to study and work in such a stimulating, persevering environment. I would like to thank him for his patient guidance, motivation and encouragement over the years. I am indebted to dr. Noémi Holderith who not only introduced me to electrophysiological and optical recording techniques, but also gave advice and support. I express my gratitude to dr. Mark Eyre, dr. Nóra Lenkey and dr. Miklós Szoboszlay for their invaluable help with electrophysiological recordings; to dr. Nóra Lenkey for teaching me the viral injection procedures; and to Klaudia Spitzer for teaching me the surgical and imaging techniques for *in vivo* experiments. I am grateful for all former and current members of the Laboratory of Cellular Neurophysiology for their constant support, inspiring discussions and for the pleasant working atmosphere. I would also like to all members of our journal club, including Makara and Szabadics labs, because these journal clubs were fundamental for the development of my critical thinking. I am thankful to Dóra Rónaszéki, Bence Kókay and Éva Dóbai for their excellent technical assistance and patience.

I would also like to thank to my previous supervisors during my undergraduate years: Prof. Péter Somogyi from University of Oxford and Prof. Tibor Szilágyi from University of Medicine and Pharmacy Tirgu Mures, for introducing me to this beautiful scientific field, neuroscience.

Last but not least I am grateful to my friends, family and my husband, Péter for their patience, understanding and support throughout the years.